TESIS DOCTORAL

Estimation of cardiac electrical activity by invasive and non-invasive mapping techniques

Autor:

Ismael Hernández Romero

Director/es:

Andreu Martínez Climent
Carlos Miguel Figuera Pozuelo

Programa de Doctorado Interuniversitario en Multimedia y Comunicaciones

Escuela Internacional de Doctorado

2019

Genius begins great works;
labor alone finishes them.
~Joseph Joubert

Agradecimientos

En primer lugar, quiero acordarme de toda la gente que me ha acompañado y sufrido en Madrid, Valencia, Cáceres, Michigan, Utah y Tobarra. Lugares que me han sido mis escenarios y hogares durante la elaboración de esta tesis.

A mis mentores, sherpas y compañeros de viaje que me ayudaron a llegar hasta aquí con la mayor dedicación, criterio y paciencia posible.

A mis compañeros del Hospital Gregorio Marañón, equipazo investigador, sin los que este trabajo hubiera sido mucho más complicado y menos entretenido. Tres ángeles hay allí que velan por mí, tres que de sobra saben quiénes son. Solo puedo agradeceros enormemente vuestro tiempo y pedir perdón a vuestros allegados por no dejar que ellos lo disfrutaran más.

A mis compañeros y alumnos de la Universidad Rey Juan Carlos y Universidad Carlos III, que tan buenos momentos me han dado.

A mis compañeros de la Universidad Politécnica de Valencia, amigos de la terreta y el caloret faller. Vuestro temperamento se debería recetar.

Todas las personas que han sido claves, de una u otra manera, en mi vida.

Y por supuesto, los que siempre han estado ahí, apoyándome y haciéndome crecer como persona, mi familia y amigos, mis padres, mi hermana… abuelos…

A todos, gracias.

A todos, quiero agradeceros por ayudarme en gran medida a desarrollar esta tesis, pero sobre todo por el tiempo que pasamos juntos durante el proceso.

Gracias, gracias y gracias y se queda en poco.

Ojala algún día os haga sentir el orgullo que realmente merecéis a todos vosotros.

Resumen

Antecedentes

Las enfermedades cardiovasculares (ECV) son la principal causa de muerte a nivel mundial (Fuster et al. 2006). Casi un tercio de la mortalidad está asociada a ECVs y el gasto sanitario que suponen en los países industrializados supera al asociado a cualquier otra enfermedad. Las patologías más comunes dentro de las ECV son las arritmias cardiacas, trastornos del ritmo cardiaco provocadas por alteraciones de la actividad eléctrica que rige el funcionamiento del corazón. En la actualidad, los tratamientos más efectivos de arritmias complejas se basan en procedimientos invasivos de ablación por radiofrecuencia (Calkins et al. 2017). Estos procedimientos permiten eliminar zonas del tejido cardiaco de mantenimiento arrítmico. Para la correcta realización de estos procedimientos de ablación, es necesario el uso de técnicas de mapeo cardiaco a partir de señales eléctricas intracavitarias para la caracterización in-situ de la actividad eléctrica.

El inicio y mantenimiento sostenido en el tiempo de las arritmias están profundamente condicionados por las propiedades del sustrato cardíaco. Aunque los mecanismos arrítmicos aún no se entienden completamente, en general se acepta que la actividad eléctrica caótica presente en estos eventos es causada por características como la velocidad de conducción lenta (CV) y los bloqueos de conducción (Jalife et al. 2011; Kléber y Rudy 2004). En particular, la existencia de fibrilación auricular (FA), una de las arritmias más comunes en la práctica clínica (John Camm et al. 2013), se ha relacionado con la naturaleza de su sustrato basado en la estructura (Burstein y Nattel 2008; Marrouche et al. 2014). Un consenso reciente ha señalado que el éxito de los procedimientos de ablación con catéter durante la FA implica una modificación del sustrato y requiere investigaciones adicionales (Calkins et al. 2017). Por lo tanto, la

identificación de regiones que son propensas a mantener arritmias es un factor clave para la caracterización de las propiedades del sustrato.

La imagen electrocardiográfica (ECGI) es una técnica de mapeo eléctrico no invasivo que tiene como objetivo reconstruir la actividad electrofisiológica en la superficie del corazón a partir de los potenciales de la superficie corporal (Brooks y MacLeod 1997; Gulrajani 1998). Requiere resolver un problema inverso mal condicionado y regularizar la solución (Oster y Rudy 1997; Willoughby 1979). Esta metodología ha obtenido resultados prometedores para caracterizar sustratos arritmogénicos como isquemia (Álvarez et al. 2012; Wang et al. 2013) y regiones dominantes de alta frecuencia (Pedrón-Torrecilla et al. 2016). Por lo tanto, el ECGI puede ser una herramienta prometedora con la resolución espacial suficiente para describir otras propiedades del sustrato auricular. En la práctica clínica, las mediciones de CV pueden proporcionar un biomarcador para identificar zonas de conducción lenta, donde existe fibrosis o acoplamiento alterado de célula a célula, siendo propensas a formar circuitos reentrantes y regiones de anclaje para rotores (Honarbakhsh et al. 2019). Sin embargo, la generación actual de sistemas de mapeo electroanatómico clínico no admite la construcción en tiempo real de mapas de velocidad de conducción, lo que requiere un análisis manual a posteriori (Cantwell et al. 2015) y dificulta el uso de esta métrica en la práctica clínica.

La medida de CV describe la velocidad a través de la dirección de propagación de un frente de onda eléctrico a través del tejido cardíaco excitable. Puede proporcionar información cuantitativa importante sobre la estructura, la orientación de las fibras del miocardio y las propiedades del sustrato intrínseco; factores que pueden ayudar a dilucidar los posibles mecanismos arritmogénicos (Cantwell et al. 2015; Roney et al. 2019). A primera vista, el enfoque para medir el CV sobre la superficie cardiaca puede parecer obvio; detectar la activación de un frente de onda en diferentes momentos y dividir la distancia recorrida por el intervalo de tiempo. Sin embargo, la complejidad de la actividad durante los ritmos fibrilatorios, donde las trayectorias pueden ser caóticas, hace que la medida de este parámetro sea un desafío. Por otro lado, la complicada geometría de la morfología auricular dificulta la viabilidad de otros métodos propuestos (Bayly et al. 1998; Kay y Gray 2005), adecuados para analizar la actividad reentrante en planos regulares 2-D como sobre registros de mapeo óptico.

Objetivos

El objetivo principal de la presente tesis es estudiar, desarrollar y validar herramientas de procesamiento de señales para caracterizar la actividad cardíaca y así aumentar nuestro conocimiento sobre los mecanismos arrítmicos y mejorar la eficacia de los tratamientos. Específicamente, el primer objetivo era desarrollar una metodología matemática para medir la velocidad de conducción de la actividad eléctrica a partir de diferentes técnicas de mapeo (por ejemplo, mapeo intracardíaco y ECGI no invasivo). El segundo objetivo fue validar las mediciones obtenidas de esta técnica novedosa bajo diferentes escenarios simulados y reales y aplicados a diferentes patologías cardíacas.

Para lograr estos objetivos, se diseñaron los siguientes objetivos específicos:

1. Desarrollar una metodología robusta para medir la velocidad de conducción tanto durante la actividad regular como durante la actividad fibrilatoria a partir de diferentes técnicas invasivas y no invasivas.

2. Validar la medición de la velocidad de conducción propuesta durante los patrones de fibrilación auricular y estudiar su uso potencial como predictor clínico de las regiones de ablación que causan la arritmia por ECGI.

3. Aplicar la medición de la velocidad de conducción propuesta durante las configuraciones experimentales que permiten aclarar los mecanismos de las alternativas en el inicio de la fibrilación ventricular.

4. Aclarar los mecanismos arrítmicos de la manifestación del patrón de Brugada en un entorno hipercalémico empleando la metodología propuesta.

Metodología

En primer lugar, la medida de la CV fue diseñada para que pudiera ser aplicada sobre patrones de fibrilación funcional reentrante, como es el caso de la fibrilación auricular.

Para determinar la CV durante ritmos simples y complejos, se remuestrearon geometrías 3D usando parametrizaciones para obtener un dominio de muestreo uniforme, que pueda representar los nuevos nodos añadidos al modelo original como un nuevo dominio, equivalente a una matriz cuadrada. Utilizando el gradiente de la información de fase para obtener la dirección normal de los frentes de onda y almacenándolos en nuestra matriz equivalente, podemos interpretar esta matriz de vectores con un enfoque aerodinámico y usar el campo vectorial generado para estimar la CV sobre cada "streamline" generada sobre este campo. La CV estimada, la orientación de los campos vectoriales y las velocidades del frente de onda puede volver a proyectarse a toda la superficie local del miocardio.

La metodología propuesta se validó mediante el uso de modelos matemáticos sintéticos 3D simples y modelos matemáticos realistas. Además se mostró su utilidad para caracterizar regiones de tejido remodelado mediante el uso de datos clínicos de pacientes reales.

A continuación, se caracterizó usando esta nueva metodología la secuencia de eventos previos al inicio de rentradas funcionales, que pueden producirse en caso de muerte súbita por fibrilación ventricular. En este caso, se usó un modelo animal experimental de inicio de fibrilación ventricular para obtener las tendencias electrofisiológicas previas al desencadenamiento de la arritmia. Además, un fármaco antiarrítmico es aplicado para poder estudiar su efecto en este escenario.

El siguiente objetivo consiste en la identificación de los mecanismos arrítmicos de sustratos cardiacos quiescentes, sustratos susceptibles de iniciar arritmias ante estímulos externos de diferente índole. En este caso, se estudió la manifestación del patrón de Brugada bajo condiciones de hipercalemia usando datos clínicos y modelos matemáticos realistas para testar las diferentes hipótesis propuestas en este ámbito. Además, se comprobó si la metodología desarrollada para estimar la CV puede servir para desenmascarar a los pacientes propensos a padecer esta afección antes de manifestarla.

Resultados

Se desarrolló una nueva metodología para estimar la velocidad de conducción aplicable a patrones de activación irregulares y su aplicabilidad se probó sobre tres escenarios diferentes: datos simulados, simulaciones por computadora de fibrilación auricular y registros de ECGI.

La mayor ventaja de esta metodología es su versatilidad, capaz de aplicarse sobre geometrías simples o complejas. El método permitió la estimación de CV durante patrones simples y fibrilatorios en geometrías auriculares realistas. El análisis de ECGI ha sido probado con registros intracardiacos. Además, se relacionó las estimaciones de velocidad obtenidas con parámetros clásicos del campo de estudio como los mapas de frecuencias dominantes, haciendo patente que esta novedosa tecnología tiene el potencial para ayudar a la estratificación de pacientes con FA en función de las áreas existentes de baja CV y beneficiarse del mejor tratamiento.

En relación a los datos experimentales de inicios fibrilatorios, se comprobó que el inicio de la fibrilación ventricular estaba relacionado con la aparición conjunta de alternancias espaciales de calcio y regiones CV lentas. Además, la modificación de la corriente de calcio por medio de un fármaco bloqueante de esta corriente, el verapamilo, provocó una disociación de la evolución en el comportamiento del calcio y del voltaje de las alternancias espaciales retrasando los inicios arrítmicos. Estos resultados destacan la relevancia de las propiedades electrofisiológicas espaciales como CV y alternancias de calcio cuando se aplica un medicamento.

Por último, los principales hallazgos en el estudio sobre pacientes susceptibles de padecer el Síndrome de Brugada demostraron que durante un episodio de hipercalemia severa, la presencia de un fenotipo de Brugada sobre la señal electrocardiografica en los modelos se asocia con una alta prevalencia de arritmias malignas y mortalidad. La manifestación de los signos de Brugada en el ECG debido a hipercalemia, se debe al aumento del potencial de reposo celular y a la reducida disponibilidad de canales de sodio que esto provoca para que haya activación cardiaca, lo que resulta en una conducción lenta y bloqueos, particularmente si existe fibrosis en el tracto de salida de ventrículo derecho. Ademas, se comprobó con nuestra herramientas que la estimación de CV puede ser útil para discriminar entre las posibles causas que pueden provocar la aparición del signo de Brugada.

Conclusiones

Los resultados obtenidos con esta variedad de datos revelan la utilidad de la metodología desarrollada para entender mejor los mecanismos arrítmicos, potenciar la utilidad de la técnica ECGI y están ayudando al desarrollo de nuevas terapias y estrategias de tratamiento. Esta Tesis contribuye a mejorar el conocimiento y la toma de decisiones en patologías reales de muy diversa naturaleza pero con factores comunes.

Abstract

Cardiovascular Diseases (CD) constitute a serious health problem worldwide. Almost one third of the mortality is associated to cardiovascular diseases and their sanitary cost in industrialized countries overcomes that dedicated to any other disease. Most common pathologies among the CD are cardiac arrhythmias, which are cardiac rhythm alterations provoked by modifications in the electrical activity governing heart functioning. Nowadays, the most effective treatment for complex arrhythmias is based on invasive processes by radiofrequency ablation. This procedure allows eliminating the areas of the cardiac tissue responsible for the maintenance of the arrhythmia. Before initiating these ablation procedures, it is necessary to use cardiac mapping techniques from intracavitary electrical signals for the characterization of the electrical activity in-situ.

Characterization of the regions prone to keep arrhythmias remains today as a major challenge for improving diagnosis, and is key for the effective treatment of cardiac arrhythmias. With the goal of providing a more detailed picture of the spatio-temporal characteristics of arrhythmias, electrocardiography imaging (ECGI) has been developed in recent years. ECGI allows obtaining cardiac electrical activity non-invasively, building tridimensional maps that represent arrhythmic characteristics. With these data, the exact mechanism of a certain arrhythmia could be reconstructed. This could provide key information for deciding the future treatment and for the planning of the surgical intervention if needed, therefore reducing its duration and costs.

Due to the emerging nature of this non-invasive system for diagnosis, this technology still lacks of technical resources for the obtaining of parameters that allow the stratification of cardiac substrate and the characterization of the initiation and maintenance of arrhythmias. Therefore, the goal of this thesis is to generate a new methodology applicable to ECGI which is capable of obtaining stratification parameters that provide the spatio-temporal cardiac characteristics and owns the

versatility to work under a variety of arrhythmic scenarios. To achieve that, a novel methodology to measure conduction velocity in simple and fibrillatory patterns of cardiac activity, together with complex 3D geometries, has been developed. This methodology was later applied to characterize and describe different arrhythmic mechanisms of varying nature using mathematical models, animal experimental models and clinical data.

In the first place, the methodology was designed to measure conduction velocity in fibrillatory functional and re-entrant patterns, as in atrial fibrillation, which is the arrhythmia with most prevalence worldwide and with current treatments of limited efficacy. The proposed methodology was validated with the use of synthetic, simple and realistic 3D models. Moreover, its utility to characterize regions of remodelled tissue was illustrated in realistic 3D models and clinical data.

Later on, it was studied the sequence of events prior to the initiation of functional re-entries that can be produced in cases of sudden cardiac death due to ventricular fibrillation. In this case, an animal experimental model of initiation of ventricular fibrillation was used to obtain the electrophysiological tendencies previous to the unleashing of the arrhythmia. In addition to that, an antiarrhythmic drug was applied to investigate its effect in this scenario.

The next goal was the identification of the arrhythmic mechanisms of quiescent cardiac substrates, studying possible hypothesis related to the appearance of cardiac diseases under specific environmental conditions. In this case, the manifestation of Brugada pattern under hyperkalemic environment was studied employing clinical data and mathematical realistic models to test the different hypothesis proposed.

The results obtained from these data illustrate the utility of this developed methodology to further investigate arrhythmic mechanisms, potentiate the utility of ECGI technique and help to develop new therapies and treatment strategies. This Thesis contributes to the improvement in knowledge for decision making in real pathologies of diverse nature but with common factors.

Contents

Agradecimientos ..... **iii**

Resumen ..... **v**

Antecedentes ..... **v**

Objetivos ..... **vii**

Metodología ..... **viii**

Resultados ..... **ix**

Conclusiones ..... **x**

Abstract ..... **xii**

Contents ..... **xiv**

List of figures ..... **xix**

Acronyms ..... **xxii**

Chapter 1 ..... **1**

1.1. Motivations **2**

1.2. Objectives **3**

1.3. Structure of the thesis **4**

Chapter 2 ..... **7**

2.1. Cardiac physiology **7**

2.1.1 The heart 7

2.1.2 Action potential 9

2.1.3 Intracellular calcium homeostasis 11

2.1.4 Nonlinear dynamics in the excitation-contraction coupling 13

2.2. Arrhythmogenesis **15**

2.2.1 Mechanisms of cardiac arrhythmias 15

2.2.2 Mechanisms of cellular alternans 16

2.2.3 Spatial alternans 20

2.2.4 Atrial fibrillation 21

2.2.5 Clinical treatment of atrial fibrillation 23

2.3. Modalities for investigating cardiac activity **26**

2.3.1 The surface electrocardiogram 26

2.3.2 Body Surface Potential Mapping 29

2.3.2 Electrocardiographic imaging 31

2.3.2 Optical mapping 33

2.4. Human cardiac modeling **35**

2.4.1 Action potential modeling 35

2.4.2 Tissue level modeling 38

2.4.3 Geometrical models 38

Chapter 3 ..... **41**

3.1. Introduction **41**

3.2. Methods **43**

3.2.1 Remeshing Data in Uniform sampling domain 43

3.2.2 Conduction Velocity Estimation 45

3.2.3 Synthetic data model 47

3.2.4 Effects of spatiotemporal resolution 47

3.2.5 Mathematical model 47

3.2.6 Patient data 48
3.2.7 Inverse solution and CV estimation 49
3.2.8 Dominant frequency analysis 49
3.2.9 Statistical analysis 51

3.3. Results 51
3.3.1 Performance of conduction velocity estimation on synthetic data 51
3.3.2 Results on realistic computer model 54
3.3.3 Results on clinical data 56

3.4. Discussion 59
3.4.1 Main findings 59
3.4.2 Performance of Conduction Velocity Estimation 60
3.4.3 Noninvasive diagnosis from the surface ECG 60
3.4.4 Limitations and future work 61
3.4.5 Conclusion 61

Chapter 4 63

4.1. Introduction 63

4.2. Methods 64
4.2.1 Isolated Heart Preparation 64
4.2.2 Optical mapping system 65
4.2.3 Experimental Protocol 66
4.2.4 Voltage and Calcium imaging processing 67
4.2.5 Identification of Voltage and Calcium Spatial Alternans 68
4.2.6 Identification of Conduction Velocities 69
4.2.7 Statistical Analysis 69

4.3. Results 69
4.3.1 Evolution of electrophysiological properties prior to VF 69
4.3.2 Mechanism of onset of VF 71
4.3.3 Effect of verapamil 72
4.3.4 Spatiotemporal mechanisms of VF inducibility 74

4.4. Discussion **77**
4.4.1 Major findings 77
4.4.2 Mechanisms of initiation of VF and Safety Pharmacology 77
4.4.3 Role of calcium alternans and CV on VF initiation 78
4.4.4 Limitations 79
4.4.5 Conclusions 80

Chapter 5 ..... **81**

5.1. Introduction **81**

5.2. Methods **82**
5.2.1 Computer Simulations 82
5.2.2 Conduction Velocity Estimation 86

5.3. Results **86**
5.3.1 Hyperkalemia, fibrosis and the mechanism of BrP 86
5.3.2 Role of Ito 90
5.3.3 Pro-arrhythmic Risk of BrP pattern 95

5.4. Discussion **97**
5.4.1 Major findings 97
5.4.2 Mechanism of pro-arrhythmic risk of BrP pattern 97
5.4.3 Limitations 98
5.4.4 Conclusions 99

Chapter 6 ..... **101**

6.1. Conclusions **101**

6.2. Guidelines for future works **103**

Chapter 7 ..... **105**

7.1. Main contributions of this thesis **105**
7.1.1 Journal papers 105
7.1.2 International conferences 106

7.1.3 Co-founder of the start-up Corify Care SL 107

7.2. Contributions related to this thesis 107

7.2.1 Journal papers 107

7.2.2 Book chapter 108

7.2.3 International conferences 108

7.3. Research stages 111

List of figures

Figure 2.1 – Electrical conduction system and morphology of AP in various locations of cardiac tissue. 8
Figure 2.2 – Action Potential. 9
Figure 2.3 – Calcium cycle in a ventricular myocyte. From (Bers 2002). 11
Figure 2.4 – AP development, the transient $[Ca^{2+}]_i$ and cell contraction. From (Bers 2002). 13
Figure 2.5 – Coupling components voltage-calcium. From (Bers 2002). 14
Figure 2.6 – Alternans in the action potential and intracellular calcium 17
Figure 2.7 – Restitution curve and its relationship with APD alternans 18
Figure 2.8 – Curve load/release of SR calcium and its relation to the alternans of CaT 19
Figure 2.9 – Example V → Ca coupling and coupling Ca → V positive and negative 20
Figure 2.10 – Types of spatial alternans. 21
Figure 2.11– Maintenance mechanisms of AF. Modified from (Swissa et al. 2002). 23
Figure 2.12 – Dominant frequency maps in three AF patients. From (Atienza et al. 2009). 26
Figure 2.13 – Precordial leads in the torso. 28
Figure 2.14 –Formation of the standard ECG signal. From (Rodrigo et al. 2015). 29
Figure 2.15 – Body surface potential maps. From Taccardi el al. (Taccardi 1963). 30
Figure 2.16 – Workflow of electrocardiographic imaging technique. 32
Figure 2.17 – Scheme of an Dual Optical Mapping System. 33
Figure 2.18 – Transmission and emission spectrum of the dyes of V_m and $[Ca^{+}]_{i..}$ 34
Figure 2.19 – Equivalent electric model of a cardiac cell. From (Jalife et al. 2011). 35

Figure 2.20 – Action potentials and APD restitution curves of the different models of human atrial electrophysiology. From (Dössel et al. 2012). 37
Figure 2.21 – 3D atria model. By (Tobón et al. 2013)..... 39
Figure 2.22 – 3D atrial model and ablation strategies. By (Reumann et al. 2008)..... 40
Figure 3.1 – Remeshing process using spherical parametrizations. 44
Figure 3.2 – Equivalence between the 3D surface and 2D plane domains. 44
Figure 3.3 – Workflow of the CV method on a reentry simulation. 45
Figure 3.4 – Activation maps obtained during sinus rhythm from icEGM in a patient..... 50
Figure 3.5 – Cross-correlation between activation maps. 50
Figure 3.6 – Estimation of conduction velocity in a sphere with synthetic data. 52
Figure 3.7 – Performance metrics of CV estimation in a spherical model. 52
Figure 3.8 – Estimation of conduction velocity in a left atrium model with synthetic data. 53
Figure 3.9 – Performance metrics of CV estimation in a left atrium model. 54
Figure 3.10 – Relationship between the estimated CV in sinus and fibrillatory rhythms from the raw signals..... 55
Figure 3.11 – Relationship between the estimated CV in sinus and fibrillatory rhythms from the ECGi signals..... 56
Figure 3.12 – Relationship between estimated CV in sinus and fibrillatory rhythms in patient data of different sources. 57
Figure 3.13 – Comparison between CV during sinus rhythm and recurrence of DF during fibrillatory rhythms in patient data. 58
Figure 3.14 – Estimated CV according to the rate of recurrence of episodes with DF. 59
Figure 4.1 – Optical mapping system setup. 66
Figure 4.2 – Description of the experimental protocol. 67
Figure 4.3 – Example of rate-dependent development of electrophysiological features obtained at different pacing cycle length in basal conditions. 70
Figure 4.4 – Sequence of VF induction. 72
Figure 4.5 – Effect of verapamil administration on alternans and CV. 73
Figure 4.6 – Example of rate-dependent development of electrophysiological features obtained at different pacing cycle length after verapamil administration. 74

Figure 4.7 – Rate-dependent changes of APD, voltage and calcium alternans for the entire dataset both during basal conditions and after verapamil administration. 75
Figure 4.8 – Maximal and minimal CV measurements. 76
Figure 5.1 – Tetrahedral finite-element wedge of ventricular mesh. 83
Figure 5.2 – Ventricular activation sequence and derivation lead positions. 85
Figure 5.3 – CV estimation using activation time of the models. 86
Figure 5.4 – Activation time of computer simulations testing the role of fibrosis of the RVOT at different levels of hyperkalemia. 88
Figure 5.5 – APD of computer simulations testing the role of fibrosis of the RVOT at different levels of hyperkalemia. 89
Figure 5.6 – Activation time of computer simulations testing the increment of I_{to} conductance. 90
Figure 5.7 – APD of computer simulations testing the role of incremental Ito conductance. 91
Figure 5.8 – Computer simulations testing the role of incremental fibrosis, I_{to} conductance and $[K^+]_o$ conditions. 92
Figure 5.9 – Computer simulations testing the role of gradient of Ito conductance over the entire epicardial surface at different levels of [K+]. 93
Figure 5.10 – Computer simulations testing the role of fibrosis over the entire epicardial surface at different levels of $[K^+]_o$. 94
Figure 5.11 – Monomorphic ventricular tachycardia. 95
Figure 5.12 – CV estimation of computer simulations with hyperkalemia. 96

Acronyms

AA	Atrial appendage (LAA and RAA are left and right respectively).
AF	Atrial fibrillation.
AP	Action potential.
APD	Action potential duration (APD_{90}).
ATP	Adenosine triphosphate.
AV	Atrioventricular (node).
AVF	Augmented lead at the left foot.
AVL	Augmented lead at the left arm.
AVR	Augmented lead at the right arm.
BCL	Basic cycle length.
BSPM	Body Surface Potential Mapping.
Ca^{2+}	Calcium ion.
cAF	Chronic atrial fibrillation.
CaT	Calcium Transient
CD	Cardiovascular Diseases
CFAE	Complex fractionated atrial electrogram.
C_m	Membrane capacitor.
CPU	Central processing unit.
CRU	Sarcoplasmic reticulum calcium release units, or ryanodine receptor.
CV	Conduction velocity.
d	Distance between cells.
D	Diffusion.
DI	Einthoven Lead I.
DII	Einthoven Lead II.

DIII	Einthoven Lead III.
ECG	Electrocardiogram.
ECGI	Electrocardiogram imaging.
EGM	Electrogram.
g_{XX}	Conductance associated to an ionic current
HT	Hilbert transform.
I_{Cab}	Background calcium current.
I_{CaL} / g_{CaL}	Inward L–type Ca2+ corrent / conductance.
I_f	Hyperpolarization–activated inward current.
I_{ion}	Resulting current through cell membrane.
I_{K1} / g_{K1}	Inward–rectifier current/conductance.
I_{Kr} / g_{Kr}	Rapid repolarizing potassium corrents / conductance.
I_{Ks} / g_{Ks}	Slow repolarizing potassium corrents / conductance.
I_{Kur} / g_{Kur}	Ultra–rapid delayed K+ current / conductance.
I_{Na} / g_{Na}	Fast sodium corrent / conductance.
I_{Nab}	Background sodium current.
I_{NaK}	Sodium–potassium pump current.
$I_{NaK,max}$	Sodium–potassium màximum pump current.
I_{NCX} / k_{NCX}	Sodium calcium exchanger current.
I_{PMCA}	Calcium pump current.
I_{to} / g_{to}	Transient outward corrent / conductance.
$J_{rel,RyR}$	Constant modulating CRUs.
K^+	Potassium ion.
k_{NCX}	Constant modulating I_{NCX}.
GP–GPU	General Purpose – Graphic Processing Unit.
LA	Left atrium.
Na^+	Sodium ion.
ODE	Ordinary differential equation.
PLB	Phospholamban.
PM	Pectinate muscles.
PN	Patient number N.
PV	Pulmonary veins.
R&D	Research and development.

RA	Right atrium.
RL	Rush–Larsen.
RMP	Resting membrane potential.
RP	Refractory period.
SA	Sinoatrial (node).
SD	Standard deviation.
SERCA	Sarcoplasmic reticulum Ca^{2+} ATPase pump.
SLN	Sarcopilin.
SP	Singularity point.
SR	Sarcoplasmic reticulum.
VN	Precordial lead (N = [1,6]).
VC	Vena cava.
V_m	Membrane potential.
WL	Wavelength.
WCT	Wilson central terminal.

Chapter 1

Introduction

Over recent decades, the development of biomedical engineering as a discipline has had a significant impact on improving the quality of life of people. And because this connection between technologists and clinicians has allowed high-tech instruments to be integrated into diagnostic and therapeutic procedures that doctors and patients face every day. Given the progress that has already been made, the room for improvement is still very high, so it is interesting in culture, business and institutions along with the great impact of this discipline. Notice the implementation of degrees and Masters in Biomedical Engineering at several Spanish universities in recent years, as well as the support from Spanish and European public and governmental entities that is reflected in the program for R&D financing "Horizon 2020" and in the Spanish Strategy for Science and Technology and Innovation 2013–2020:

- To build new and cutting–edge therapeutic methods as part of a continuous process of discovery and testing chasing clinical performance.
- To facilitate the association between Spanish health and technological development investors through collaboration with medical organizations, basic and technical science and globally relevant companies.

One of the major areas of biomedical engineering is cardiac electrophysiology. Since the first manifestations of the myocardium's electrical activity and its contribution to the heart's pumping capacity due to the excitation–contraction binomial by bringing the electrocardiogram (ECG) into clinical practice, significant progress has been made in the understanding of the electrical processes which cause stable and abnormal heart episodes. Nevertheless, the mechanisms of initiation and maintenance are not fully understood in the field of atrial tachyarrhythmias, though new approaches

to diagnosis and treatment are needed. For this reason, atrial and cardiac tachyarrhythmias research attracts a strong scientific interest in congresses devoted to this topic or the publishing of books and articles on high-impact factors.

Historically, many of these authors have included the use of animals or patients to test various diagnostic and therapeutic improvement hypotheses. Thanks to the continuous development of software and simulation systems, the arrival of in-silico research in recent years mitigates technological and ethical issues associated with experimental animal studies. Cardiac electrical activity simulations enable theories to be tested with high control of the variables involved and serve to test their feasibility avoiding huge economic and ethical costs.

1.1. Motivations

Cardiovascular diseases (CVD) are a serious health problem worldwide. Almost a third of the mortality is associated with cardiovascular diseases and the health expenditure they represent in the industrialized countries exceeds that associated with any other disease. The main causes of CVD are cardiac arrhythmias, heart rhythm disorders caused by alterations in the electrical activity that governs the functioning of the heart. Currently, the diagnosis of complex arrhythmias is based on invasive procedures that provide maps of cardiac activity from electrical signals obtained from inside the heart. In the last decade, different cardiac mapping techniques have been proposed, both invasive and non-invasive. Non-invasive techniques, based on the analysis of electrical signals recorded on the patient's torso, are called the electrocardiography imaging (ECGI) and combine signal processing with computational models of the bioelectrical characteristics of the patient's torso. The ECGI is a great technological challenge, because in its general formulation it is an ill-conditioned and indeterminate problem. A large number of different approaches have been proposed in the scientific literature to ensure the most accurate estimates possible. Despite its potential, the scope of these techniques has limitations, since i) it is necessary that the parameters obtained contain the spatiotemporal nature of cardiac activity to be useful in the clinic and ii) the validation methods are little developed.

The main hypothesis of this thesis was that a robust technique to measurement of the conduction velocity from invasive and no-invasive cardiac mapping techniques

could be developed and provide independent information to increase our knowledge regarding arrhythmias and to improve treatments efficacy.

During the development of the present doctoral thesis, a methodology applicable to different registration techniques, both invasive and non-invasive, incorporating information on cardiac activity is proposed. The developed algorithms are validated through the use of realistic, experimental mathematical models, as well as clinical records of patients in different scenarios of interest: Brugada syndrome, atrial and ventricular fibrillation. Cell, organ and human torso level mathematical models supported with experimental data have been used in this thesis to validate our hypotheses.

1.2. Objectives

The driven goal of the present technological thesis was to study, develop and validate signal processing tools to characterize cardiac activity to increase our knowledge regarding arrhythmias and to improve treatments efficacy. Specifically, the fist aim was to develop a mathematical methodology to measure conduction velocity of electrical activity from different mapping techniques (e.g. intracardiac mapping and non-invasive ECGI). The second aim was to validate the measurements obtained from this novel technique under different simulated and real scenarios and applied to different cardiac pathologies.

To achieve these objectives, the following specific objectives were designed:

1. To develop a robust methodology to measure conduction velocity both during regular and during fibrillatory activity from different invasive and non-invasive techniques.

2. To validate the proposed conduction velocity measurement during atrial fibrillation patterns and to study its potential use as clinical predictor of ablation regions causing of the arrhythmia from ECGI.

3. To apply the proposed conduction velocity measurement during under experimental set-ups that allow the clarification of the mechanisms of alternans on the initiation of ventricular fibrillation

4. To clarify the arrhythmic mechanisms of the manifestation of Brugada pattern under hyperkalemic environment by employing the proposed methodology.

1.3. Structure of the thesis

This thesis is structured in the following chapters:

Chapter 2: State of the art. In this chapter, the main concepts implied in this thesis are introduced and reviewed. Cardiac electrophysiology and electrocardiography are introduced including the body surface potential mapping (BSPM) technique. The different mechanisms discussed as responsible of the maintenance of tachyarrhythmias, as the features of the arrhythmias analyzed in this thesis are described.

Chapter 3: Complete-Chamber Conduction Velocity Estimation During Arrhythmias. A new methodology was designed to measure conduction velocity in fibrillatory functional and re-entrant patterns, as in atrial fibrillation, which is the arrhythmia with most prevalence worldwide and with current treatments of limited efficacy. The proposed methodology was validated with the use of simple and realistic 3D models.

Chapter 4: Characterization of events prior to the initiation of fibrillation. The sequence of events prior to the initiation of ventricular fibrillation was studied. An animal experimental model of initiation of ventricular fibrillation was used to obtain the electrophysiological tendencies previous to the unleashing of the arrhythmia. In addition to that, an antiarrhythmic drug was applied to investigate its effect in this scenario.

Chapter 5: Arrhythmic mechanisms of quiescent cardiac substrates. The goal was the identification of the arrhythmic mechanisms of the manifestation of Brugada pattern under hyperkalemic environment, employing clinical data and mathematical realistic models to test the different hypothesis proposed.

Chapter 6: Discussion and conclusion. The results and main findings introduced in this thesis are discussed and compared with previous works and summarizing the main findings. The conclusions are listed and a guideline for future works is proposed.

Chapter 7: Contributions. The scientific contributions associated to this thesis and derived from the present dissertation are listed in this chapter. The scientific framework in which this thesis has been involved is also described including the research stays and collaborations.

Chapter 2

State of the art

In this chapter, the state of the art and key concepts are given as an introduction to Chapters 3, 4 and 5. This is an interdisciplinary work that covers different fields and branches related to cardiology, computer simulation and electrophysiological mechanisms. For this reason, with the aim of facilitating the understanding of the thesis, this chapter will cover: (i) the explanation of cardiac physiology (ii) an overview of cardiac arrhythmias and their interventional treatments (iii) the different methods and techniques that allow obtaining cardiac electrical activity information and (iv) how human cardiac computer models can be implemented and used to obtain relevant information.

2.1. Cardiac physiology

2.1.1 The heart

The heart is the organ responsible for pumping blood through the circulatory system, allowing blood flow between the lungs and other organs. It is divided into four chambers; the two upper chambers are called atria and the two lower chambers, the ventricles. Each atrium and ventricle communicates through valves, and the right side is separated from the left through the interatrial and interventricular septum respectively.

The heart is able to pump blood through the body through rhythmic and coordinated contractions that allow continuous blood flow. The specialized conduction

tissue or cardiac electrical system is responsible for the generation and propagation of electrical stimuli or action potentials (AP) that promote the cardiac contraction. In Figure 2.1 we can see both the different chambers of the heart and the distribution and driving characteristics of the cardiac electrical system.

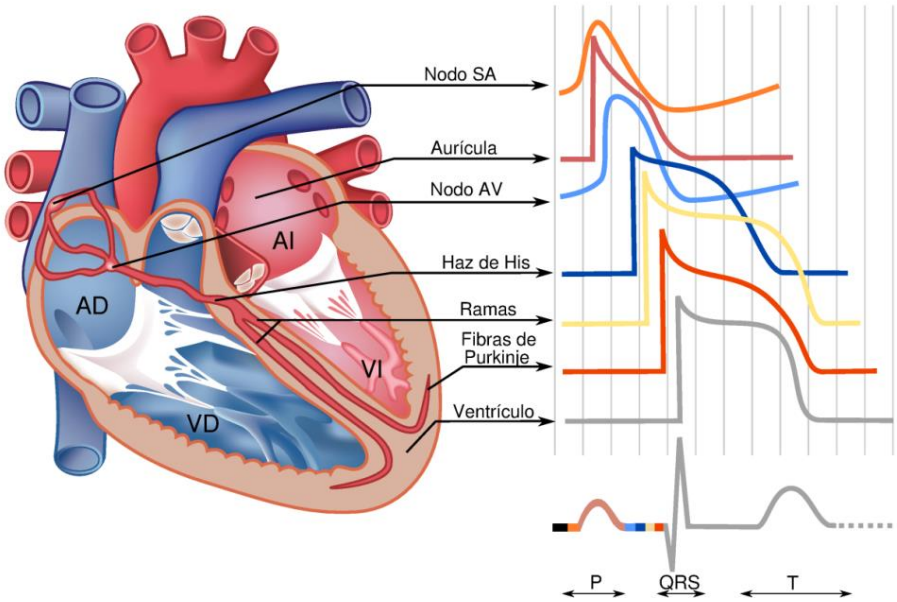

Figure 2.1 – Electrical conduction system and morphology of AP in various locations of cardiac tissue.

Frontal heart section. The main elements of heart anatomy are shown.

The origin of activation of this system occurs in the sinoatrial node, or SA node, which is self-excitable. The stimulus generated by the SA node spreads to the atria through the cardiac fibers causing their contraction. Next, the impulse reaches the atrioventricular node, or AV node, in which a delay is introduced until the atria have emptied, essential to achieve an effective ventricular systole. The AV node is connected in its output to a continuation of the conduction system, known as the Bundle of His, which is formed by a set of specialized fibers in electrical conduction. Bundle of His is divided in two branches that descend through the septum, one on the right side and another on the left side. Both branches have multitude of fibers extending throughout the ventricles in branches. These fibers are known as Purkinje fibers.

The purpose of the conduction system formed by the bundle of His and Purkinje fibers is that the excitation arrives almost simultaneously to all the ventricular muscle, responsible for carrying out the mechanical action that causes the blood pumping. As a

result of this simultaneous activation, an organized, synchronized and therefore efficiently contraction of heart muscle is obtained.

2.1.2 Action potential

As already mentioned in section 2.1.1, the mechanical efficiency of the heart is closely related to its electrical behavior. The electrical activity of the heart is the result of the overall electrical potential generated by each individual myocardial cell. This is due to differences between the concentrations of ions between intra- and extracellular media and the semipermeable nature of the cell membrane. The ions present in the intra- and extracellular media that cause electrical activity are sodium (Na^+), calcium (Ca^{2+}) and potassium (K^+). These ions are key for the action potential or electrical activity of the cardiac cell, as their concentration and charge balance is essential for the triggering of such activity (Jalife et al. 2011; Malmivuo and Plonsey 1996).

The action potential comprises several phases (phase 0, 1, 2, 3 and 4), in which not only the ions but also different ionic currents are involved, as shown in Figure 2.2.

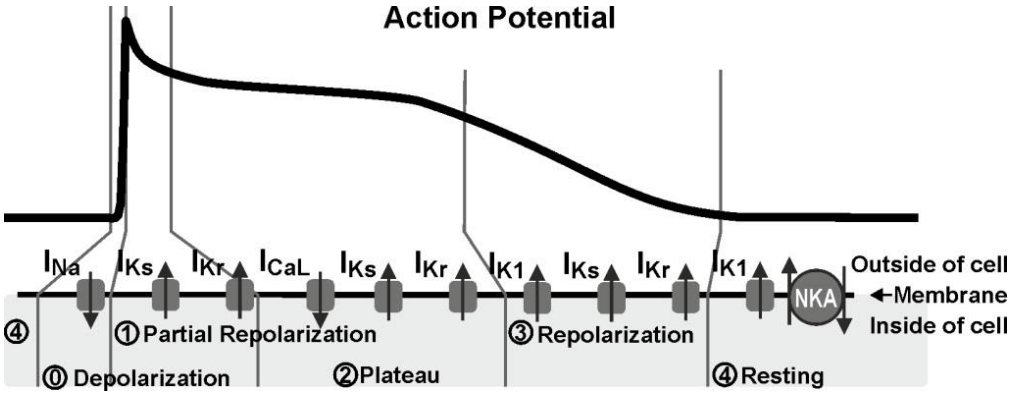

Figure 2.2 – Action Potential.

Action Potential signal and the main ionic channels and pumps involved in each AP phase are depicted above. Arrows show the direction of transportation of the ions.

The different phases of action potentials' rapid response are as follows:

- Initially the membrane potential (V_m) of the cell is stable, this being similar to the equilibrium potential of potassium ions, of about -85 mV, as during this phase the potassium ion permeability is much higher than the permeability of the other ions.

- **Phase 0** of the action potential starts with membrane depolarization. The approximate length of this phase is 1 ms. At this stage and once the threshold potential is reached, the fast sodium channels (voltage-controlled) open, allowing the influx of Na^+ ions (fast sodium current I_{Na}) as a consequence of diffusion and electric field balance, causing the upstroke of the action potential. This current remains inactive in the other phases of the action potential.
- Then in **phase 1**, the potassium ion channels open and a flow of potassium ions ranging from inside the cell to the outside is created, causing a short repolarization represented by the peak of the AP. The currents present in this phase are independent potassium current time (I_{K1}), the potassium current plateau in (I_{Kp}) and the transient outward (I_{to}).
- The later **phase 2 or plateau phase**, that lasts approximately 200 ms, is characterized by a positive voltage that remains almost constant until phase 3. This is produced by the output of potassium ions that is compensated by calcium entry. On the one hand, calcium ions enter through L-type channels (I_{Ca}), and potassium ions leave through rapid (I_{Kr}) and slow potassium currents (I_{Ks}).
- In **phase 3**, inactivation of calcium channels occurs while the potassium channels remain open so that the membrane potential returns quickly to the equilibrium potential. This repolarization process is accelerated by the opening of voltage-dependent K^+ (I_{K1}) channels.
- Finally in **phase 4**, the repolarization is completed reaching the resting membrane potential, being the potential between the interior and the exterior of the cell negative again. For this phase, the most contributing ion currents are sodium-potassium (I_{NaK}) and sodium-calcium exchanger pump (I_{NaCa}). To achieve the resting membrane concentration, the sodium calcium exchanger has the function to restore the intracellular calcium concentration by expelling it from the interior of the cell by entering sodium ions into the cell. Moreover, there is an excess of sodium into the cell and of potassium in the extracellular medium, so that the sodium-potassium pump is activated to restore the concentrations of these two ions, extracting and introducing sodium potassium respectively.

2.1.3 Intracellular calcium homeostasis

Among the ions involved in the complex workings of the heart, calcium is considered one of the most important. Calcium is crucial in the process that allows the heart chambers to contract and relax, a process called excitation-contraction coupling (Bers 2002; Jalife et al. 2011). To understand the basic physiology of cardiac function, it is important to understand in detail the flow of calcium through different organelles in the myocytes and its function in each of them for the excitation-contraction coupling to occur. In Figure 2.3 the cell and the different compartments involved in the calcium cycling process are shown.

Calcium is released into the cytosol by two different processes: influx from the extracellular medium into the cell or from its release from the sarcoplasmic reticulum.

As explained in the previous section, channels of L-type calcium open when a cardiac myocyte is depolarized during an action potential. This opening allows calcium to flow from the extracellular space including T tubules into the intracellular space or cytosol (current I_{CaL}).

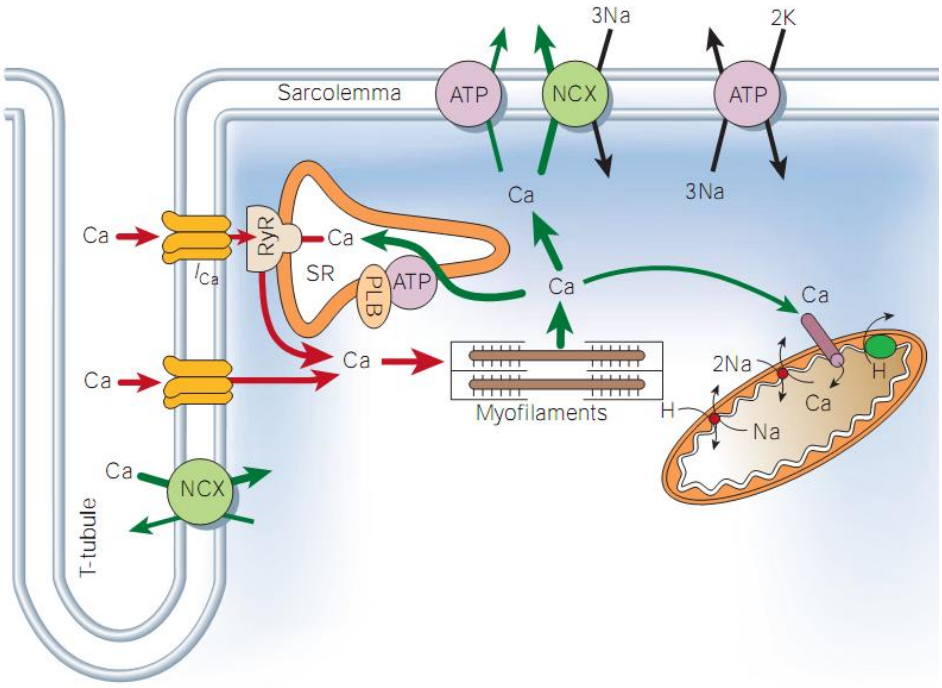

Figure 2.3 – Calcium cycle in a ventricular myocyte. From (Bers 2002).

The release of calcium from the sarcoplasmic reticulum comprises several steps. First of all, it is important to note that the sarcoplasmic reticulum is in charge of storing it. Whenever the cytosol presents low levels of calcium ions, calcium sensitive

channels present in the vicinity of the L-type ryanodine receptors (RyR), detect an increase in local concentration of Ca^{2+}, releasing the calcium contained in the compartments binding sarcoplasmic reticulum (JSR). This process is commonly referred to as the release of calcium induced calcium (CIRC).

The combination of Ca^{2+} influx from the extracellular medium and release from the sarcoplasmic reticulum raises the free concentration of intracellular Ca^{2+} ($[Ca^{2+}]_i$), allowing the ions to bind proteins such as troponin C, calmodulin or calsequestrin. By interacting with these proteins, calcium is responsible for regulating cellular effects as well as for starting the contractile machinery. Troponin C protein is present in actin filaments; when calcium binds to this protein, the free binding points of actin are exposed, so actin is able to interact with myosin and therefore produce cell contraction.

For relaxation to occur, the $[Ca^{2+}]_i$ must decrease, dissociating troponin C. This requires that the Ca^{2+} out of the cytosol is transported by four different processes:

- The Ca^{2+}-ATPase of sarcoplasmic reticulum (SERCA) reintroduces calcium therein, through the tubular network sarcoplasmic reticulum pump (NSR).
- Sodium calcium exchanger balances the concentrations of calcium, taking a Ca^{2+} ion to the extracellular medium by three Na^{+} ions feeding.
- The Ca^{2+}-ATPase pumps in the cell membrane or sarcolemmal Ca^{2+} expel it directly to the extracellular medium.
- The mitochondrial Ca^{2+} uniporter makes Ca^{2+} to reenters it.

Once the $[Ca^{2+}]_i$ decreases, cell contraction relaxes, and part of the Ca^{2+} content in the tubular network NSR sarcoplasmic reticulum flows by diffusion to the JSR compartments, completing the cycle. Figure 2.4 shows the result of this cycle from the onset of action potential, which causes an increase in intracellular calcium and cell stimulating muscle contraction.

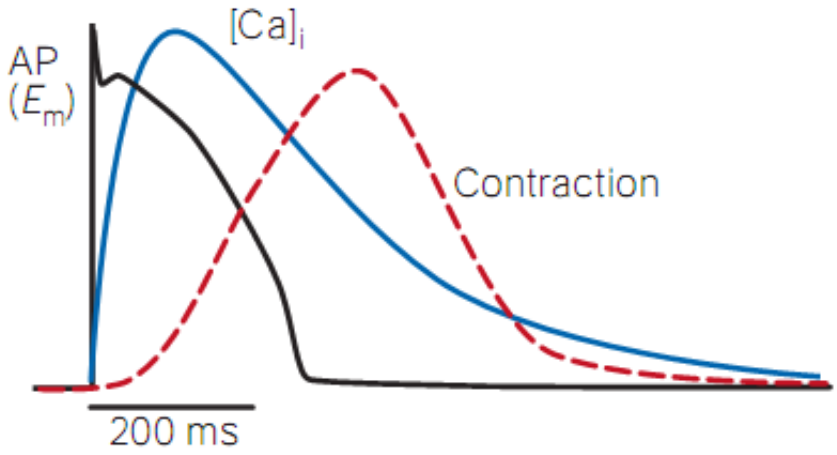

Figure 2.4 – AP development, the transient $[Ca^{2+}]_i$ and cell contraction. From (Bers 2002).

2.1.4 Nonlinear dynamics in the excitation-contraction coupling

Described above are the mechanisms that result in the electrical activity of cardiac myocytes and the effect that it provokes on muscle at the cell level. Among the different mechanisms that are part of this system, it is important to highlight the high overall complexity of the process. This is in part due the nonlinear dependence of some channels and ion transporters on one or more variables such as the transmembrane potential or a particular ion concentration. Furthermore, to add more complexity to this scenario, the existing variables have different interconnected dependencies from and onto each other, through loops that feed positively or negatively (Bers 2002; Krogh-Madsen and Christini 2012).

Because of the complexity of this system, it is often unpredictable how altering a factor may affect the behavior of the different mechanisms and what effects it may cause. This nonlinear dynamics have been observed at heart subcellular, cellular and whole organ level (Karma and Gilmour Jr 2007). Another example of non-linear dynamics is also present in the excitation-contraction coupling.

The excitation-contraction coupling has two main players of other dependent mechanisms that are involved in it: transmembrane potential and intracellular calcium. In Figure 2.5 a schematic of this scenario is shown.

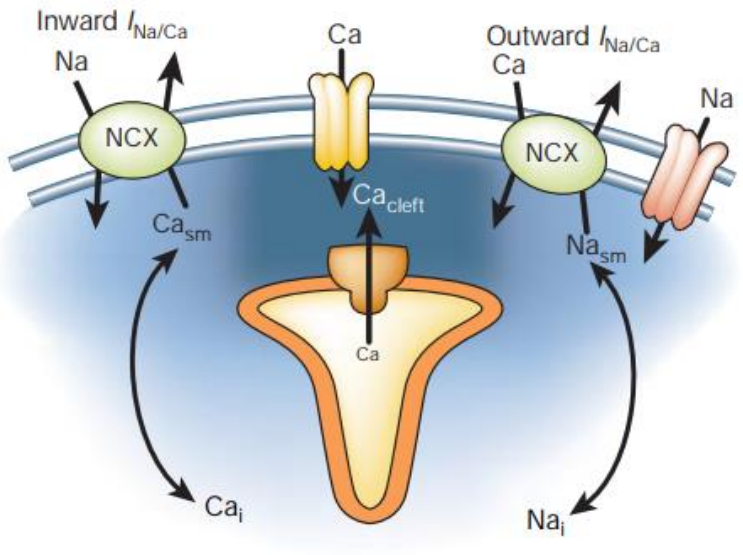

Figure 2.5 – Coupling components voltage-calcium. From (Bers 2002).

The main contributors of the various mechanisms to the coupling system are:

- **Calcium channel (I_{Ca}):** Activation of these channels is voltage-dependent, since their opening increases with depolarization. When the membrane potential is depolarized, the current L-type calcium activity increases due to the progressive opening of the channels to its maximum value. Inactivation of calcium channel has two components: voltage dependence and calcium concentration-dependence. This dual mechanism causes an accelerated inactivation of calcium currents when large intracellular calcium intakes occur. Thus, L-type channels can be inhibited by calcium own negative feedback mechanism dependent on the local concentration of calcium in the vicinity of the channel.

- **Sodium calcium exchanger (I_{NXC}):** The NCX exchanger has two operating modes: direct and reverse. In the direct mode, during repolarization, the NCX expels calcium into the extracellular space in exchange for sodium, giving rise to an input current. However, during the rising phase of the action potential, this exchanger is typically operated in reverse mode, as it introduces calcium into the cell and removes sodium. This is due to the large membrane depolarization and elevated intracellular sodium concentration that has entered by sodium channels.

- **SR ryanodine receptor (RyR):** Its opening for the release of calcium from the sarcoplasmic reticulum to the cytosol is based on the recognition of calcium ions in the cytosolic side of the membrane SR through a positive feedback system: activation is

greatest when intracellular calcium concentration increases rapidly. In addition, the SR calcium release is higher as more calcium is loaded in the SR. Next, a negative feedback mechanism occurs when cytosol calcium inactivates the RyR.

- **SR calcium pump (SERCA):** The function of the SERCA pump adjusts the dynamic changes in calcium concentration in both the cytosol and the SR. The natural tendency is to introduce SR calcium from the cytosol, although it has been shown that this can be reversed (Makinose and Hasselbach 1971). However, under physiological conditions it is believed that the reverse speed is negligible.

As shown, there is a strong correlation between the membrane potential and the intracellular calcium concentration, so that disturbance on one of these variables will considerably change the behavior of the others. During a normal contraction cycle, the process would correspond to that described in the previous section. However, under pathological or arrhythmic conditions, this association is destabilized.

2.2. Arrhythmogenesis

The mechanical function of the heart is controlled by its electrical activity. When the synchrony of the heart's electrical activation suffers an alteration of its regular pace (around 60 to 100 beats per minute, sinus rhythm), the heart has an episode of cardiac arrhythmia. Cardiac arrhythmias may be categorized as ventricular arrhythmias or supraventricular arrhythmias. While some ventricular arrhythmias may be fatal, supraventricular arrhythmias reduce standard of lives and are a significant epidemiologic problem in modern societies.

2.2.1 Mechanisms of cardiac arrhythmias

Cardiac arrhythmia mechanisms can be classified as: (i) a result of an abnormal impulse development (i.e. automaticity or trigger) or (ii) a fail of impulse propagation (i.e. reentry). Also, combinations of these mechanisms are likely to happen frequently (Issa, Miller, Zipes 2009). However, the underlying factors of arrhythmogenesis can be of different nature, such as genetic abnormalities or ischemia. Diagnosis of fundamental causes of arrhythmia is of vital importance to choose an adequate therapy for the patient.

- **Abnormal automaticity.** A characteristic of cardiomyocytes from the sinus node is the spontaneous impulse generation (automaticity). These cells generate a periodic depolarization that is transmitted to passive cardiomyocytes, enabling the spread of the wavefront to the neighboring tissue. When the sinus node does not work properly, the conductive system's automaticity induces other rhythms as response. Moreover, cardiomyocytes may display improved ordinary automaticity or unusual automaticity under particular circumstances that is absent under normal circumstances. Drugs, diseases, ionic misbalances, or nervous activity can induce this automaticity.
- **Triggered activity.** An electric trigger is an involuntary afterdepolarization development. Afterdepolarizations are new excitations in transmembrane potentials that happen during an AP (early afterdepolarizations) or after the end of the AP cycle (delayed afterdepolarization). If the depolarization threshold is reached by an afterdepolarization, a different unintentional AP is produced.
- **Abnormal conduction and reentry.** Reentry takes place when a propagating electrical wavefront depolarizes cardiac tissue in a pathway with abnormal conduction. Activation wavefronts normally disappear spontaneously after activation of the whole heart due to the long duration of the refractoriness (period not sensitive to new depolarization) compared to the duration of the cardiac activation (Issa, Miller, Zipes 2009). In pathological conditions, the shortening of the refractory period or slowing of the conduction velocity can sustain a continuous self-maintained activation wavefront, leading to a reentry. Reentries can be initiated by a conduction block and circulate back on themselves (functional reentries), or around anatomic obstacles (structural reentries).

2.2.2 Mechanisms of cellular alternans

Many cardiac arrhythmias, such as ventricular fibrillation (VF), are characterized by electric front breaking waves that cause a reentry that stimulates new propagation wavefronts (Weiss et al. 2005). However, the underlying mechanism of this process is not fully understood. Traditionally, this break has been attributed to the presence of anatomical obstacles or heterogeneities in the heart, such as the presence of an ischemic

area. However, the dynamic properties of heart cells have taken center stage as they can play an important role in promoting these arrhythmias.

This view holds that the beginning and maintenance of fibrillation are due to intrinsic dynamic factors of the own heart, such as the kinetics of the ion channels or the frequency of ion homeostasis. This approach has been taken into account since the phenomenon of alternans was observed experimentally.

Alternans are defined as variations of action potential duration (APD) or the amplitude of the intracellular calcium transient (CaT) between successive heartbeats. This behavior can be seen in Figure 2.6.

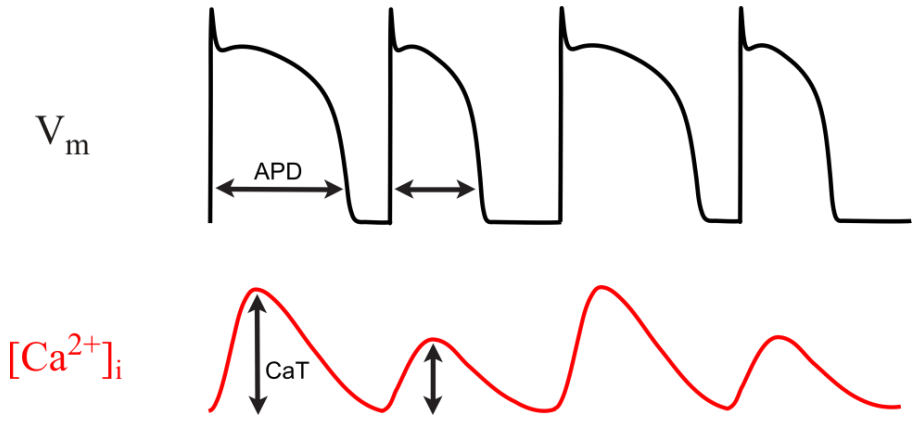

Figure 2.6 – Alternans in the action potential and intracellular calcium

The mechanism behind this phenomenon can be attributed to various factors such as the APD restitution, calcium dynamics or calcium-voltage coupling.

- **APD restitution**

APD restitution is the ratio between the APD and diastolic interval former (DI). When the length of the stimulation cycle (CL) decreases, accompanied with progressive shortening of DI, some of the ionic currents in depolarization cannot fully recover from inactivation and be reenabled; or conversely, some currents may not be inactivated in repolarization, causing APDs progressively shorter. Restitution may be related to the alternans of APD by graphic media (Nolasco and Dahlen 1968). Plotting the restitution curve, when the slope is steep (≥1), a small perturbation in the pacing cycle progressively causes rising fluctuations in APD until reaching stationary alternans. On the other hand, when the slope is flat (<1), a change in the pacing cycle would not lead to alternans; as illustrated in Figure 2.7.

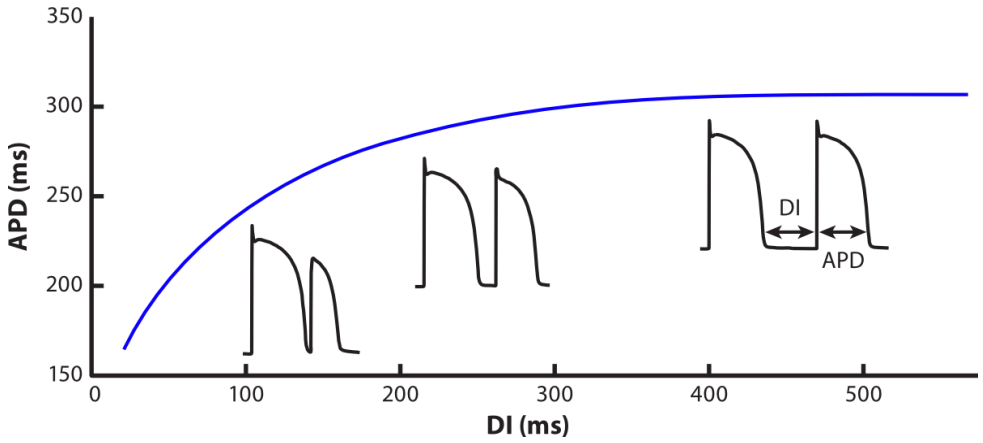

Figure 2.7 – Restitution curve and its relationship with APD alternans

The limitation of this mechanism is that it does not always predict the exact initiation of the alternans. It is possible that the slope is flat and still alternans appear, or that the slope is pronounced and alternans do not appear.

- **Calcium dynamics**

In this case, the mechanism that produces alternans is the existing non-linear relationship between the amount of calcium in the sarcoplasmic reticulum and the calcium concentration that it can release. At increasing rate, more calcium enters into the cell because the calcium channels are activated more frequently. Due to this, the reticulum stores more amount of intracellular calcium, and because the relationship between loading and release is nonlinear, it may happen that the SR releases more calcium that what was stored in this pulse, oscillating between two states and causing alternans in intracellular calcium. This behavior is illustrated in Figure 2.8.

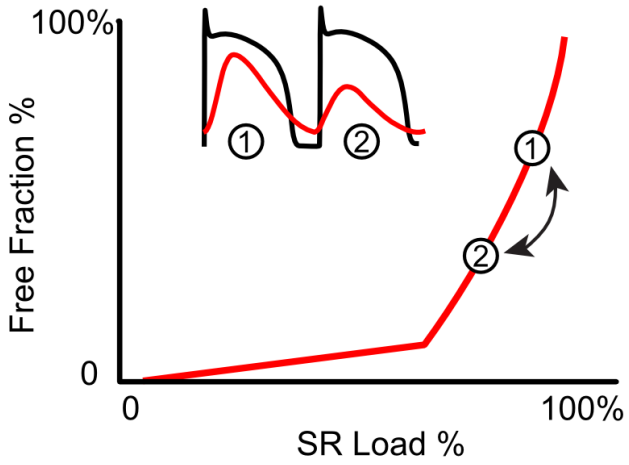

Figure 2.8 – Curve load/release of SR calcium and its relation to the alternans of CaT

- **Calcium-voltage bidirectional coupling**

The above points considered nonlinear dynamics of membrane voltage regardless of the calcium cycle, or calcium dynamics regardless of membrane potential. However, these systems are coupled bidirectionally, so to clarify the mechanisms that develop alternans, these must link the two systems. Consequently, two behaviors that promote alternans at the cellular level can be observed; (i) changes in the dynamics of the transmembrane potential affect the calcium domain (V → Ca), or conversely, (ii) that calcium modules the transmembrane potential (Ca → V). Examples of both behaviors are illustrated in Figure 2.9.

1. Coupling V → Ca: In this case, the L-type calcium current available during the action potential directly affects the amount of calcium released from the SR. ICaL availability in a given heartbeat depends critically on the previous diastolic interval. The higher the DI, the longer it takes for L-type calcium channels to recover; therefore, the release of calcium increases in response to an increase of DI in the previous heartbeat.

2. Coupling Ca → V: This coupling can be positive or negative. In the positive coupling, an increase in CaT is capable of increasing the incoming exchanger calcium sodium current, which causes an elongation of APD. By contrast, in the negative coupling, an increase of CaT may also cause inactivation by excesive calcium of ICa, which tends to shorten the APD.

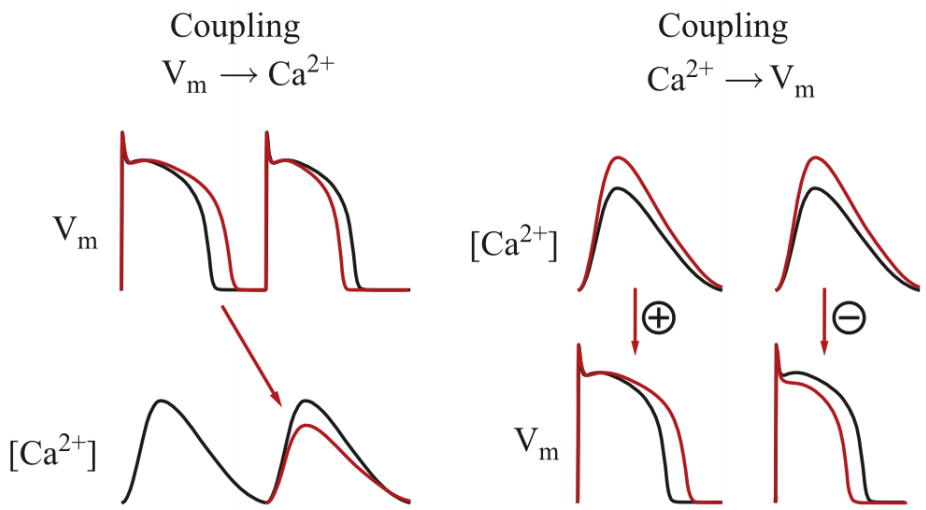

Figure 2.9 – Example V → Ca coupling and coupling Ca → V positive and negative

If the voltage alternans are synchronous to calcium, they are called electromechanically phase alternans. If they are out of phase, as in the Ca → V negative coupling, they are called electromechanically out of phase alternans.

2.2.3 Spatial alternans

The previously exposed alternans mechanisms occur at the cellular level and are described from the temporal point of view. However, it is necessary to go to the organ level and the spatial distribution of the alternans to understand the importance of this phenomenon at the onset of cardiac arrhythmias.

Spatially, cardiac alternans can be classified as concordant or discordant (Pastore et al. 1999). In the case of spatially concordant alternans (Figure 2.10A), all tissue regions alternate in phase with each other which means that for a given rate, the APD or CaT shows the same pattern throughout the whole tissue. However, in the spatially discordant alternans (Figure 2.10B), some tissue regions oscillate out of phase relative to others. These regions that are out of phase are separated by a nodal line where alternation is not present. In this nodal line, spatial gradients of APD or CaT are more abrupt, and that causes a blockage in the wavefront propagation. Therefore, the spatially concordant alternans are less arrhythmogenic than spatially discordant alternans.

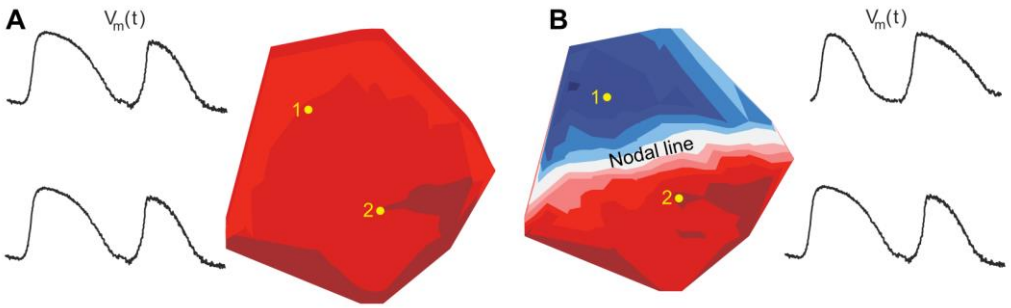

Figure 2.10 – Types of spatial alternans.

(A) Spatially concordant alternans. (B) Spatially discordant alternans.

Spatially discordant alternans may be a favorable substrate for initiation of reentry after ectopic beats. Also, if the tissue is heterogeneous, some regions are more susceptible to alternating than others, obtaining a reentry event even in the absence of a premature ectopic beat. For these reasons, these types of alternans are of special interest to study the onset of cardiac arrhythmias.

2.2.4 Atrial fibrillation

Atrial fibrillation (AF) is the most common supraventricular arrhythmia (Haïssaguerre et al. 2000; John Camm et al. 2013). It is characterized by chaotic and fast excitation patterns of the atrial tissue. Atrial cells depolarize at very high frequencies during atrial fibrillation that can exceed 400 activations per minute. This disorganized activity alters the synchronized activation of the atria and thus causes inefficiency in the contractile forces of these cardiac chambers. As a result, the blood circulation is inefficient and increases the risk of thromboembolism (John Camm et al. 2013).

AF also promotes an abnormal ventricular function, since the atrioventricular node receives numerous electrical wavefronts and transmits a disordered sequence to the ventricles, filtering some of them and allowing patients to survive. However, the ventricular rate does not suit the sinus rhythm and therefore does not respond to the patient's requirements at any time, leading to discoordination of ventricular depolarization (Nattel 2002; Nieuwlaat et al. 2005).

The processes accountable for the initiation and sustainability of AF have not been fully grasped and have remained a subject of debate in the clinical practice. Over time, the incidence of AF in patients may differ and the clinician uses the recurrence of the symptoms to create a diagnosis. Although there are different classifications of AF according to the clinical guidelines used, the most widely used incidence classification is as follows (Fuster et al. 2006):

- Detected for the first time. Although the event may or may not be symptomatic, the clinician may categorize it as a first event of AF in case of doubt.
- Recurrent. It is regarded recurrent when the person has had two or more periods of AF.
    - Paroxysmal. When AF accidentally begins and ends.
    - Persistent. If AF is kept for 7 days and return to sinus rhythm needs pharmacological therapy or cardioversion. Also included in this category are long-term FA cases (over a year).

The first AF detected can either be persistent or paroxysmal.

- Permanent. It occurs when the patient has an unstoppable state of continuous AF, or when the patient takes a new episode of AF after a short time after cardioversion.

AF maintenance mechanisms are not yet known and several hypotheses state different theories. The main hypothesis can be reduced to three: multiple wavelet, ectopic foci and rotor hypothesis, mechanisms depicted in Figure 2.11.

1. Multiple wavelet hypothesis states that AF is generated by several wavefronts spreading chaotically across atria (Moe 1962). However, the ability to treat AF by removing high frequency areas in recent years has made this theory less relevant (Guillem et al. 2016b).
2. Ectopic focci hypothesis states that wavefronts resulting from high frequency focal sources become fractionate in atrial tissues, thus maintaining the AF (Nattel 2002).
3. Rotor hypothesis says that the AF is a structured process in the spatio-temporal domain that is caused at high frequency focal locations by rotors or structural reentries that generate chaotic activity in the surroundings. In addition, this hypothesis is compatible with the presence of multiple wavelets and ectopic foci for the underlying AF mechanism (Guillem et al. 2016b).

As the evidence of a hierarchical distribution of the dominant frequency during AF episodes has been described, the scientific community has argued that the initiation and maintenance of AF requires a driver (rotor or ectopic focus) or a variable number of drivers and a substratum that promotes turbulent propagation through the atrium (Jalife et al. 2011). Still, all these mechanisms do not necessarily have to be exclusive.

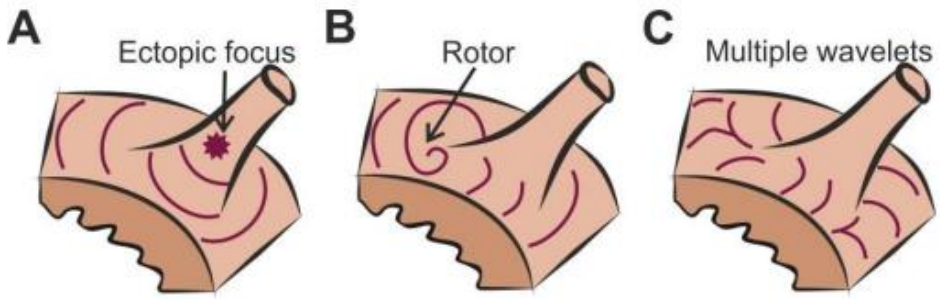

Figure 2.11– Maintenance mechanisms of AF. Modified from (Swissa et al. 2002). *(A) Ectopic focci, (B) rotor (C) Multiple wavelet theories are depicted.*

Regardless of the hypothesis, the main factors favoring AF are changes in AP biomarkers such as shortening the duration of AP and effective refractory periods in conjunction with a reduction in tissue conductivity (Dössel et al. 2012). In addition, both electrical remodeling caused by permanent AF and structural remodeling caused by atrial cavity dilation leading to fibrosis due to decreased contractibility enhance these factors (Burstein and Nattel 2008). This remodeling has significant effects when attempting to treat AF, since patients with paroxysmal AF can be treated with high-frequency driver surgical ablation. In the case of patients with chronic or persistent AF, due to changes produced by atrial remodeling process, this method is not sufficient to stop the arrhythmia.

2.2.5 Clinical treatment of atrial fibrillation

One of the therapies used to stop AF by applying controlled electrical impulses that synchronize the electrical activity of the atria is electrical cardioversion. This technique does not eliminate the underlying causes of AF episodes. Treatments based on radiofrequency ablation or pharmacological compounds are used to suppress or inhibit the arrhythmia. AF therapies combine both types of therapy to enhance the results.

Antiarrhythmic drugs

The most common methodology for reducing AF episodes or their symptoms is pharmacological therapy. The main goals of these drugs are to prevent episodes of arrhythmia, control cardiac frequency (sinus and atrioventricular nodes), anticoagulate blood, or chemical cardioversion.

Antiarrhythmic drugs are categorized according to the impacted receptor or ionic processes. Notice that antiarrhythmic drugs can simultaneously have an impact in many ionic currents despite getting a widespread impact in some ion channels. The following families of antiarrhythmic drugs are distinguished according to the Vaughan–Williams classification (Nattel and Singh 1999; Williams 1984):

- Class I: They have a significant impact on Na^+ channels and are categorized into three subclasses based on the AP length impact. These drugs decrease cell excitability and are therefore called membrane stabilizers.
  - Class Ia: These drugs slow down stage zero and lead to a delay in repolarization and an increase in the effective refractory period.
  - Class Ib: At high frequencies, these antiarrhythmic agents have a significant effect over the Na^+ channels. This effect, however, is accompanied by a reduction in the duration of the AP and an effective refractory period.
  - Class Ic: It also affects Na^+ channels but does not change the repolarization stage in this situation.
- Class II: or β–blockers, act by blocking the sympathetic activity of the heart, reducing the number of propagations through the atrioventricular node for supraventricular tachyarrhythmias.
- Class III: These drugs block the potassium channels leading to an elongation of the action potential and the effective refractory period. Since Na^+ channels are not impacted, they prevent reentrant tachyarrhythmias from being maintained.
- Class IV: These drugs block ICaL channels and are usually used by the atrioventricular node to reduce the number of propagations. These medicines have the inconvenience of reducing heart contractility but allow heart rate control that is considerably reduced by β-blockers.

Since antiarrhythmic drugs do not only impact the atria, they may have significant side effects that boost mortality levels (Calkins et al. 2009; Nattel 1998).

Radiofrequency ablation

Radiofrequency ablation is an invasive treatment that damages the region of the atria that causes the arrhythmia and thus eliminates the AF origin (Calkins et al. 2009; Fuster et al. 2006). This source's identity and place is an important objective to accomplish before this source's ablation. Haissaguerre recognized pulmonary veins as the most common place of AF drivers (Haissaguerre et al. 1997) leading to a revival in the clinical therapy of AF, as vein isolation has become a gold standard in the AF treatment (Jalife et al. 2011), with achievement levels of 70% in patients with paroxysmal AF and 22% in children with permanent AF (Oral et al. 2002). However, in other regions of the atria, such as the upper vena cava, left posterior free wall, crista terminalis or coronary sinus, AF sources have also been detected (Haissaguerre et al. 1997). Consequently, different strategies based on an electrogram-guided identification of the specific primary AF drivers can be performed in order to increase the success ratios or reduce the damaged area (Calkins et al. 2009). In this context the ablation of complex fractionated atrial electrogram (CFAE) areas or highest dominant frequency areas has been evaluated.

The ablation of CFAE is justified on the premise that primary sources of AF support fractionated and complicated electrograms. However, while some writers maintain that AF termination was successful for 95% by targeting CFAE regions (Nademanee et al. 2004), other clinicians obtained a success level of just 57% for the same circumstances (Oral et al. 2007). Other authors attempted to isolate faster-electric regions (Atienza et al. 2009; Atienza et al. 2006; Mansour et al. 2001; Sanders et al. 2005). Atienza et al. also found that ablation achievement in patients with no frequency gradients was very small, similar in most instances to constant AF patients (Atienza et al. 2009), indicating that ablation therapies should be prevented under some circumstances.

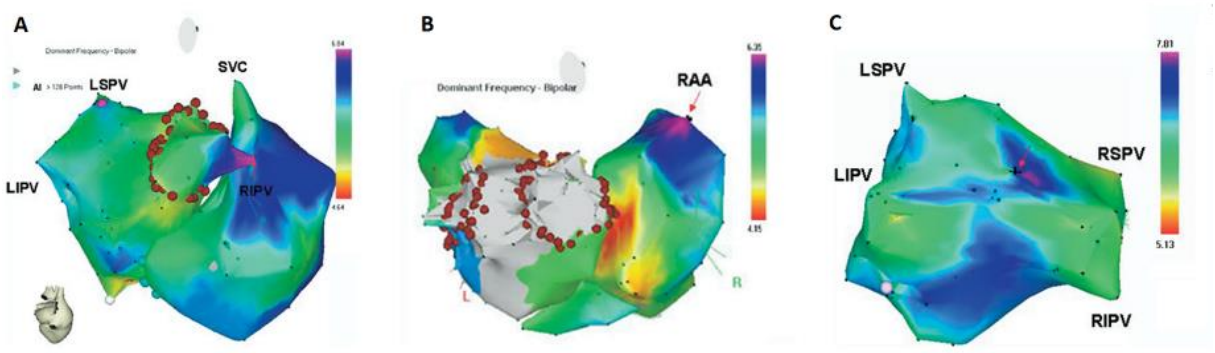

Figure 2.12 – Dominant frequency maps in three AF patients. From (Atienza et al. 2009).

For a patient with paroxysmal AF, (A) it indicates a dominant frequency chart showing an elevated dominant region in the right pulmonary inferior vein. The fibrillation finished with the ablation peaks shown in blue after this region was isolated. (B) It indicates a paroxysmal AF patient. In the right atria appendage, the largest dominant frequency was observed here. (C) It indicates a patient without frequency gradient with constant AF. The method of ablation could not prevent the arrhythmia.

2.3. Modalities for investigating cardiac activity

2.3.1 The surface electrocardiogram

Electrocardiogram (ECG) recorded on the human torso has become one of the most powerful diagnostic techniques in cardiology since Einthoven invented this recording technique in 1903 (Einthoven 1906). Due to the importance of cadiac electrical activity in cardiac diseases, ECG signals were widely studied for all cardiac diseases, and more specifically in cardiac arrhythmias. Since this ECG signal was discovered and analyzed, it has been used for non-invasive diagnosis of heart disease.

By placing 3 electrodes on the right arm, left arm and left foot respectively, Willem Einthoven determined the standard ECG leads. Electrode positions define a triangle with the heart in the center called the Einthoven's triangle:

$$\begin{aligned} &\text{Lead I:} && DI = \phi_L - \phi_R \\ &\text{Lead II:} && DII = \phi_F - \phi_R \\ &\text{Lead III:} && DIII = \phi_F - \phi_L \end{aligned} \qquad (2.1)$$

where

DI = the voltage of Lead I

DII = the voltage of Lead II

$DIII$ = the voltage of Lead III

ϕ_L = potential at the left arm

ϕ_R = potential at the right arm

ϕ_F = potential at the left foot

By assessing the potential between a single electrode and the midpotential of the two surviving electrodes used as a guide, Goldberger launched three extra leads. These leads are regarded as augmented leads due to the increase in the signal.

$$AVR = \phi_R - \frac{\phi_L + \phi_F}{2}$$
$$AVL = \phi_L - \frac{\phi_R + \phi_F}{2} \qquad (2.2)$$
$$AVF = \phi_F - \frac{\phi_R + \phi_L}{2}$$

The augmented leads are completely redundant with respect to the leads defined by Einthoven and obtain information from the cardiac activity projection on a single plane defined by the three electrodes. On the anterior and left side of the chest six more electrodes additional electrodes can be placed, defining the precordial leads labeled as V1-V6. As shown in Figure 2.13, electrodes corresponding to V1 and V2 are located at the fourth intercostal space on the right and left side of the sternum respectively, V4 is in the fifth intercostal space on the midclavicular line; V3 between V2 and V4; V5 at the same horizontal level of V4 but on the anterior axillary line and V6 in line with V4 and V5 but on the midaxillary line. Precordial leads are evaluated using the Wilson Central Terminal (WCT), which is described as the center of Einthoven's triangle and is calculated as an average of the three electrodes' potential:

$$V_{WCT} = \frac{\phi_R + \phi_L + \phi_F}{3} \qquad (2.3)$$

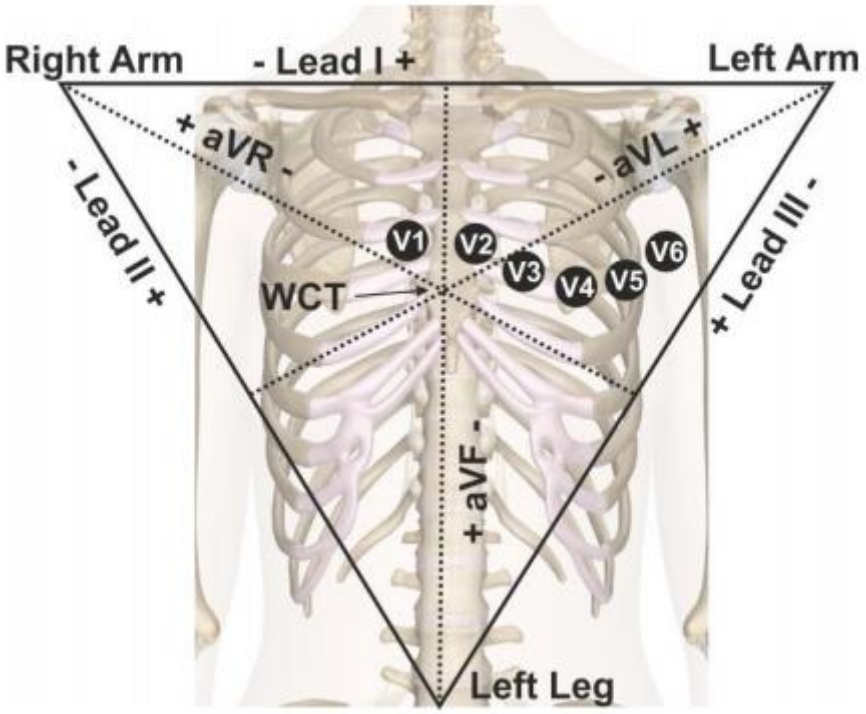

Figure 2.13 – Precordial leads in the torso.

ECG imaging triangle (right hand, left hand and left leg). Leads I, II, and III at the triangle's three corners and augmented leads (aVR, aVL, and aVF) between each side's vertex and midpoint. Precordial leads (V1-V6) are calculated as the potential of the Einthoven's triangle vertex between each precordial recording site and the Wilson Central Terminal (WCT).

The ECG recording shows several deflections or waves that reflect the electrical activity of the heart chambers. The ECG is a spatial summation of the APs active in the heart at each instant. A normal, non-pathologic electrocardiogram is shown in Figure 2.14. The so-called P wave corresponds to the atria depolarization. After the P wave it is possible to observe the delay introduced by the AV node as an inactive period. Then there is ventricular depolarization, which is reflected in the QRS complex. Note that due to the greater mass of the ventricles and the synchronization at which the ventricles contract, the amplitude of this complex is higher compared to the P wave. This is in part due to the bundle of His and Purkinje fibers that allow a considerably rapid spread of the AP through the ventricular tissue. The T wave corresponds to the ventricular repolarization or returns to the resting state, while the QRS complex masks the repolarization of the atria (Malmivuo, Malmivuo, Plonsey 1995).

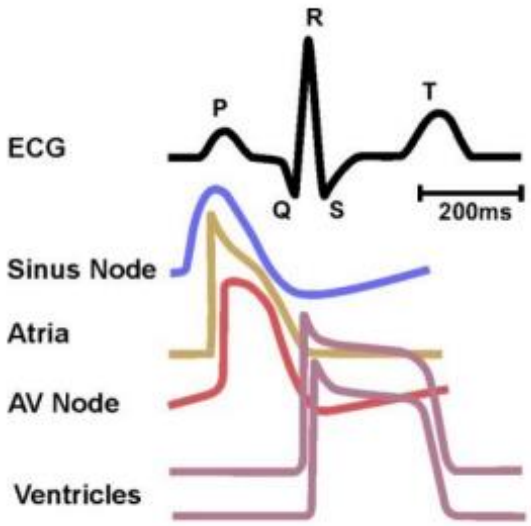

Figure 2.14 –Formation of the standard ECG signal. From (Rodrigo et al. 2015). *The black ECG signal and the APs responsible for each wave are shown. It can be observed that depolarization of atrial cells leads to the P wave, ventricular depolarization and repolarization produce QRS complex and T wave respectively.*

2.3.2 Body Surface Potential Mapping

It was believed for a long time that the 12-lead ECG could capture all the appropriate clinical electrocardiographic data on the torso. Frank (Frank 1954) stated that it was possible to model roughly 95 percent of the QRS complex as an equal single dipole with a set location. Taccardi (Taccardi 1963) refuted this hypothesis years ago, showing that some pathologies demonstrate patterns in the torso with various peak and minimum prospective fields, thus requiring several dipoles to acquire a right model. This principle has been applied to diseases such as Brugada syndrome (Guillem et al. 2010) and is of particular interest to diseases involving simultaneous wave fronts such as atrial fibrillation (Guillem et al. 2009a; Guillem et al. 2013). To enhance the non-invasive diagnosis of these complicated illnesses, it was suggested to register the electrocardiographic signals throughout the torso using a larger number of electrodes.

Body Surface Potential Mapping (BSPM) is a method consisting on the acquisition of the cardiac electrical activity on the entire torso to obtain more data about cardiac electrical activity than with the standard electrocardiogram. It makes it possible to detect events that could not be identified in the standard 12-lead ECG (Finlay et al. 2005; Taccardi et al. 1998). The heart electrical field is therefore recorded on the whole

torso surface with a number of electrodes ranging from 32 to 256 (Hoekema, Uijen, Van Oosterom 1999). Although there is no a defined amount of electrodes or location, most study organizations strive to position more electrodes on the front of the torso as there are considerably larger potential changes on the front.

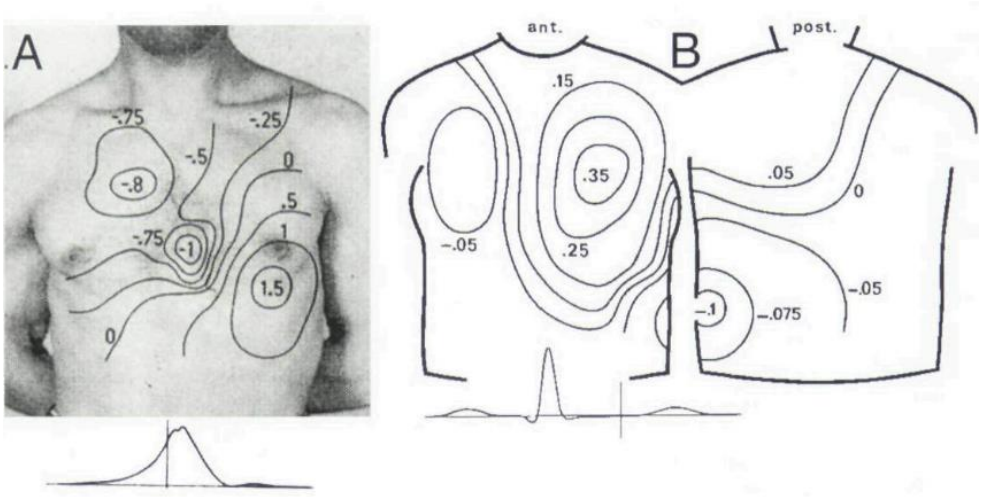

Figure 2.15 – Body surface potential maps. From Taccardi el al. (Taccardi 1963). *Panel A shows a normal BSPM after 30ms of QRS onset. Panel B shows a map of a patient with angina, during de ST interval, an abnormal minimum can be observed in the left–posterior part of the torso. This area is not registered in the standard 12–lead ECG.*

By using BSPM, several studies have shown an improved diagnosis. By analyzing the QRS integral and the ST segment gradient in BSPM recordings, Bruns et al. (Bruns et al. 2002) elucidated that upper right precordial leads enabled better detection of Brugada syndrome with ECG markers. Eckardt et al. (Eckardt et al. 2002) demonstrated that inducibility of ventricular tachyarrhythmias in patients with Brugada syndrome was predicted by the presence of late potentials and ST segment elevation on BSPM recordings. For the location of accessory pathways in Wolf–Parkinson–White patients, Dubuc et al. (Dubuc et al. 1993) used isopotential maps from BSPM recordings to guide catheter ablation. In the field of atrial arrhythmias diagnosis, Sippens Groenewegen et al. demonstrated that the origin of focal tachycardias (SippensGroenewegen et al. 1998) could be determined by analyzing BSPM maps. Wavefront propagation maps were introduced by Guillem et al. as a technique to summarize the pattern of electrical propagation in a single map during atrial flutter

(Guillem et al. 2009b) and to characterize the degree of organization during atrial fibrillation (Guillem et al. 2009a). Guillem et al. also demonstrated that spatial frequency gradients of activation in AF can be detected on BSPM recordings by calculating the power spectral density of several surface derivations (Guillem et al. 2013), which cannot be achieved using the standard 12-lead ECG. Rodrigo et. introduced band-pass filtering and phase analysis (Rodrigo et al. 2014) to differentiate atrial fibrillation episodes driven by the right atria from those driven by the left atria. These works demonstrate how several techniques have been developed to compute and display clinically relevant information obtained from BSP recordings. However, the need to validate these results in a larger population hinders the introduction of BSPM into the clinical practice.

2.3.2 Electrocardiographic imaging

Electrocardiographic testing (ECGI) is a medical tool to estimate electrical activity on the heart non-invasively. Together with the surface electrical activity recorded with a BSPM system, this technique uses three-dimensional torso and heart models of the patient to reconstruct electrical activity on the heart surface (see Figure 2.16). Reconstruction of intracardiac activity requires a mathematical procedure that solves the so-called inverse electrocardiography problem, i.e. calculating epicardial potential from BSPM recordings. On the other hand, electrical activity on the chest (ECG) from cardiac electrical activity (EGM) offers the forward problem of electrocardiology. Since the forward problem has a closed mathematical formulation defined by the biophysical equations and the volume of the torso, this formulation can be inverted to obtain the electrical epicardial activity from the rest of the known variables (Horácek and Clements 1997a). This methodology was validated in animal models and human studies under pathological conditions (Oster et al. 1997).

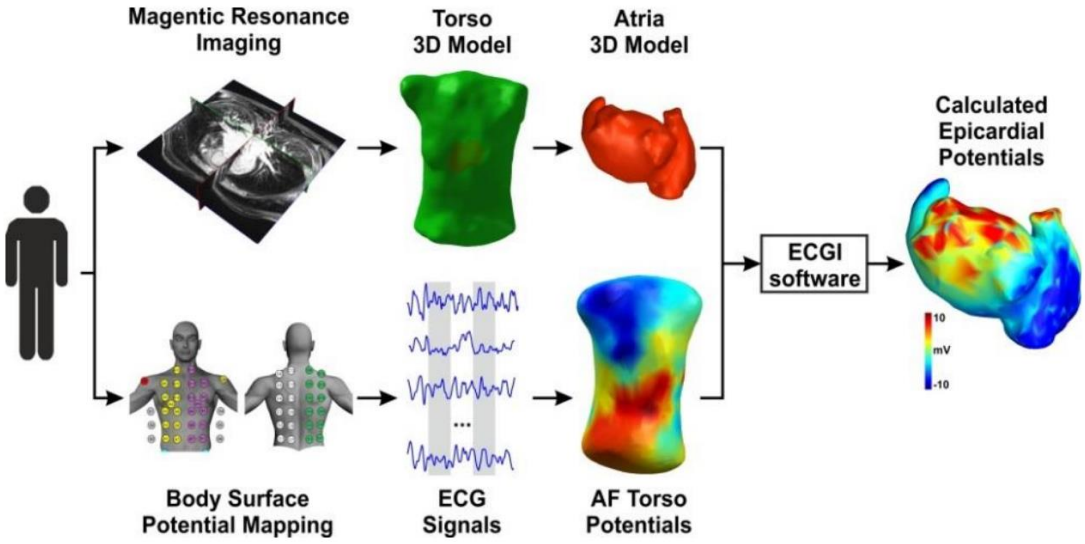

Figure 2.16 – Workflow of electrocardiographic imaging technique.

3D models of torso and atria patient are segmented from MRI images and together with BSPM recordings, epicardial potentials can be determined.

ECGI has been commonly used to explore cardiovascular diseases (MacLeod et al. 1995; Oster and Rudy 1997), as it offers intracardiac activity in a comparable manner to invasive catheter-based techniques but with higher spatial resolution, non-invasiveness and more versatility as it can also be used prior to surgical procedures. In patients with congestive heart failure, ECGI has allowed the activation sequences to be reconstructed to identify suitable candidates for cardiac resynchronization therapy and guide the placement of the lead (Jia et al. 2006; Silva et al. 2009). In patients with myocardial infarction (Cuculich et al. 2011), ECGI was also used to delimit the scar region and to identify slow conductive regions that could provide reentrant arrhythmias. Because of the elevated spatial resolution and the simultaneity of the rebuilt electrograms, ECGI is extremely suitable for the research of ventricular arrhythmias, such as ventricular tachycardia (VT), as it enables to demonstrate its development and continuity at acceptable risk (Wang et al. 2011).

2.3.2 Optical mapping

Optical mapping is a technique that enables the recording of membrane potential (V_m) and ionic concentrations, such as intracellular free calcium ($[Ca^{2+}]_i$), at in vitro and in vivo level with high spatial and temporal resolution (Lee et al. 2012). Using this technique it is possible to study V_m and $[Ca^{2+}]_i$ interactions simultaneously in different preparations such as single cells, cell culture monolayers or the entire heart. An example of this system is shown in Figure 2.17.

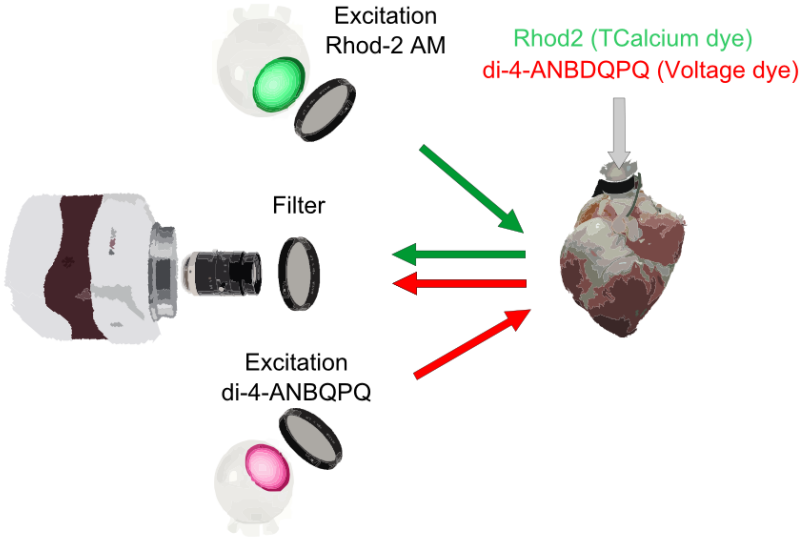

Figure 2.17 – Scheme of an Dual Optical Mapping System.

The key to this technique is that recordings are performed in the optical domain. This is achieved with the use of some chemicals, known as fluorescent dyes. They have the characteristic of emitting an amount of photons when being excited by an external light source that is proportional to the amount of the ligand to which they are coupled. Depending on the dye, a specific excitation wavelength should be used for each type. For example, when applying a potentiometric dye on the surface of a heart, the intensity of the light emitted by the dye is directly related to the phase of the action potential in which each cell is at a specific time.

Stimulation of fluorescent dyes is performed by light emitting diodes (LEDs), which offer a more effective and efficient excitation than other alternative light sources. Then, the emitted light is filtered by filters in the emission band of the different dyes. It is preferable that these bands of excitation and emission do not

overlap, allowing simultaneous recording of multiple parameters, as illustrated in Figure 2.18.

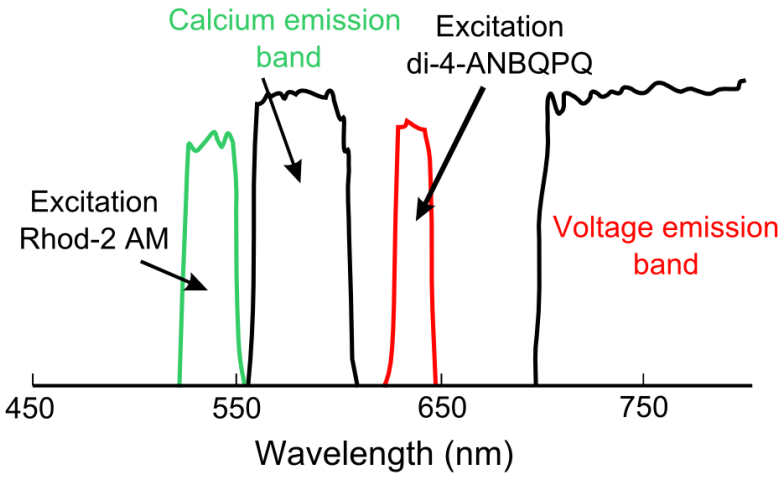

Figure 2.18 – Transmission and emission spectrum of the dyes of V_m and $[Ca^+]_i$.

The filtered light is recorded by low noise and high speed photodetectors, which are responsible for performing optoelectric conversion, thus obtaining the parameter studied simultaneously throughout the capture zone.

One of the main advantages of this system is the possibility to record the action potential with a suitable spatial and temporal resolution in a wide region of the epicardium, allowing to study the ionic or AP spread in the heart surface. In addition, this recording method can be combined with different stimulation protocols, with spatial and temporal variations such as the pacing rate, or to characterize drug effects.

The major drawback of optical mapping is the need for isolation to apply a highly toxic chemical to the heart, therefore requiring ex-vivo hearts. Moreover, the applied dye may have side effects affecting the generation of the action potential. Another problem associated with optical mapping technique is the lack of an accurate calibration measurement of the action potential in each optical experiment.

Finally, the presence of artifacts that are introduced into the acquired signal due the associated mechanical motion of the heart represents an important disadvantage. To prevent this from occurring, drugs that decouple mechanical activity of the heart's electrical activity are used, inhibiting the movement of the heart but keeping electrical activity interrupted. However, despite the fact that these drugs are able to reduce the artifacts in the recorded optical signal, these drugs can also introduce changes in AP morphology (Lee et al. 2012).

2.4. Human cardiac modeling

Cardiac modeling has become a tool for improving the understanding of atrial physiology and pathophysiology over the past decades. Mathematical modeling enables access and control of variables not available in experimental or clinical research while reducing costs and avoiding technical and ethical issues.

2.4.1 Action potential modeling

Hodgkin and Huxley designed the first AP mathematical model in the 1950s (Hodgkin and Huxley 1952). It was based on experimental voltage clamp data applied to squid giant axons and was the basis of most of the electrophysiological models developed since then. In general, Hodgkin–Huxley-based models are based on the equivalent circuit of a membrane-defined system and intra-and extracellular media as shown in Figure 2.19.

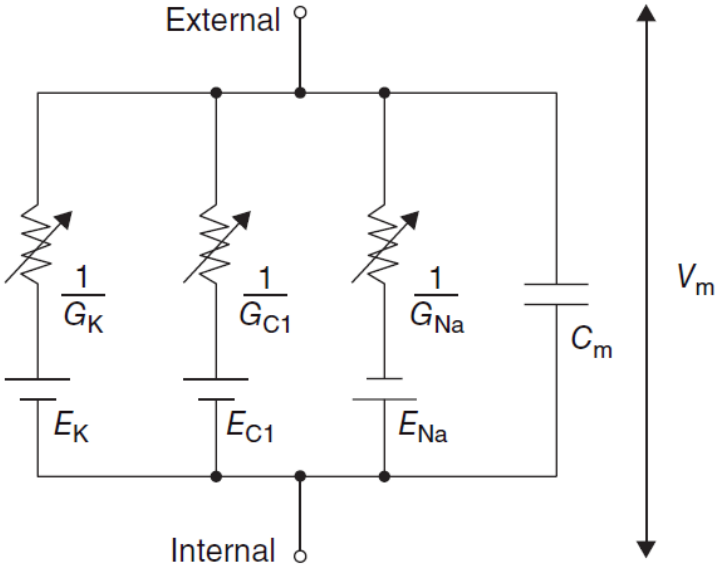

Figure 2.19 – Equivalent electric model of a cardiac cell. From (Jalife et al. 2011). *Membrane voltage V_m depends on the charge of the ionic channels (modelled as variable resistors or conductances) controlling the different ionic currents of the membrane capacitor C_m.*

The diagram shows internal and external media and the lipid membrane is presented as a C_m capacitor, the variable plotting APs is the membrane potential (V_m).

The variables that modulate the AP shape are ion channels, which can be opened, closed or inactivated depending on the various conditions associated with voltage, time, or chemical messaging. All this activity can be summarized electrically as variable resistors and Ohm's Law can be used to define the magnitude of the current circulating in each channel group, which depends on the equilibrium potential of each ion at the same time:

$$I_x = (V_m - E_x) \cdot G_x \qquad (2.4)$$

The currents associated with each channel, pump or ion exchanger group are summarized in the resulting current I_{ion}, which charges or discharges the V_m modulating capacitor.

$$\frac{\partial V_m}{\partial t} = -\frac{I_{ion}}{C_m} \quad \text{being} \quad I_{ion} = \sum_{x=1}^{n} I_x \qquad (2.5)$$

Although the basis of mathematical modeling is relatively simple, all ionic currents need to be exhaustively characterized for an electrophysiologically accurate model. In this sense, countless patch clamp experiments were performed allowing the individual measurement of all these ionic currents in isolated cells, and these measures were used to extract the electrical parameters that define the main ionic currents. Denis Noble made the first mathematical model of cardiac myocytes by modifying Hodgkin and Huxley model (Noble 1962), and subsequent experimental data enabled his cardiac myocyte model to be improved by describing ionic pumps and differentiating ionic currents (McAllister, Noble, Tsien 1975). Luo and Rudy modified this model to build the first mammalian ventricular myocyte model (Luo and Rudy 1991), which Iyer and ten Tusscher (Iyer, Mazhari, Winslow 2004; Ten Tusscher et al. 2004) also improved.

Human atrial myocyte modeling started with two different models published simultaneously in the 1990s: the model of Courtemanche (Courtemanche, Ramirez, Nattel 1998) and the model of Nygren (Nygren et al. 1998). They presented some differences in the possible shape of the AP, as can be seen in Figure 2.20, although both were based on the same experimental data. Maleckar et al. subsequently enhanced the formulation of some repolarizing currents (Maleckar et al. 2008), Koivumäki et al. included a exhaustive formulation of sarcoplasmic reticulum and Ca^{2+} dynamics

(Koivumäki, Korhonen, Tavi 2011) and Grandi et al. also upgraded the management of Ca^{2+} (Grandi et al. 2011).

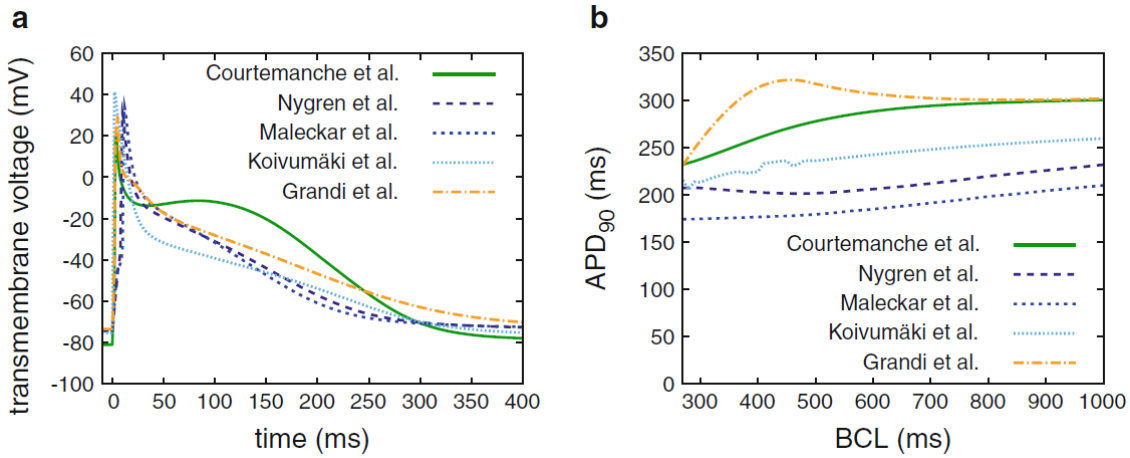

Figure 2.20 – Action potentials and APD restitution curves of the different models of human atrial electrophysiology. From (Dössel et al. 2012).

Atrial myocyte mathematical models were primarily used to assess the effect of AF-induced electrical and structural remodeling and its relationship with arrhythmia inducibility. Electrical remodeling was observed to cause a reduction in the duration of the AP, which was reported to be caused by changes in certain specific ionic behaviors (Brundel et al. 2001; Dössel et al. 2012; Skasa et al. 2001; Workman, Kane, Rankin 2001). It has also been shown that a reduced handling of Ca^{2+}, which corresponds to lower intracellular Ca^{2+} transients, results in a decrease in cell contractility, another characteristic property of remodeled cells (Schotten et al. 2001). Lastly, the electrophysiological effect of structural remodeling was mathematically modelled as atrial myocytes electrically connected to cardiac fibroblasts (Maleckar et al. 2009) and dilated atrial cells resulting in increased membrane capacitance (Corradi et al. 2012; Koivumäki et al. 2014; Schotten et al. 2002). All these mathematical simulations of single atrial myocytes have made it possible to investigate the relationships between the various ionic currents and their effect on the electrophysiological behavior of atrial cells as well as the effect on AF progression such as electrical and structural remodeling.

2.4.2 Tissue level modeling

The AP propagates through the tissue by depolarizing local current that flows through gap junctional channels from the depolarized cells to their neighboring myocytes. This current increases the membrane potential and leads to the opening of Na^+ channels that initiates a new action potential.

This behavior is modeled as a continuous excitable medium with diffusion of membrane voltage local excitation, known as the reaction-diffusion model. The monodomain model describes the simplest description of possible propagation of APs:

$$\frac{\partial V_m}{\partial t} = -\frac{I_{ion}}{C_m} + \nabla \cdot D\nabla V_m \qquad (2.6)$$

The transmembrane voltage, as shown above, is the difference between intracellular and extracellular potentials. Unlike the monodomain model, the bidomain model considers variation in ionic concentrations and potential in extracellular space, but the resulting system of equations is much more complex and increases computational costs. Since the monodomain model reproduces most of the wave propagation-related phenomena, it is the most commonly used (Clayton and Panfilov 2008; Dössel et al. 2012). However, these models can not address the variations in the extracellular domain such as current injections in electrical cardioversion defibrillation (Trayanova 2006).

2.4.3 Geometrical models

The addition of the previously described tissue model in an anatomical geometry enables simulations of electrical patterns in a entire structure or organ. These complete simulations enable propagation patterns to be realistically reproduced in a physical environment with the cardiac characteristics.

Various geometric models following atrial anatomy have been developed for this purpose. These models can be represented as a single surface and based on triangular meshes (Dam and Oosterom 2003; Jacquemet et al. 2003) because the atrial wall tends to be thin. However, there are models whose elements are defined by tetrahedrons or cubes, including the thickness of the atrial wall (Aslanidi et al. 2011; Krueger et al.

2011; Krueger et al. 2013; Tobón et al. 2013) They are commonly extracted from medical imaging techniques, such as computer axial tomography (Burdumy et al. 2012) or magnetic resonance (Virag et al. 2002). Anisotropic conduction properties can also be implemented (Dössel et al. 2012), as well as several atrial regions with different electrophysiological properties taken from the cell model (Tobón et al. 2013), as it is depicted in Figure 2.21.

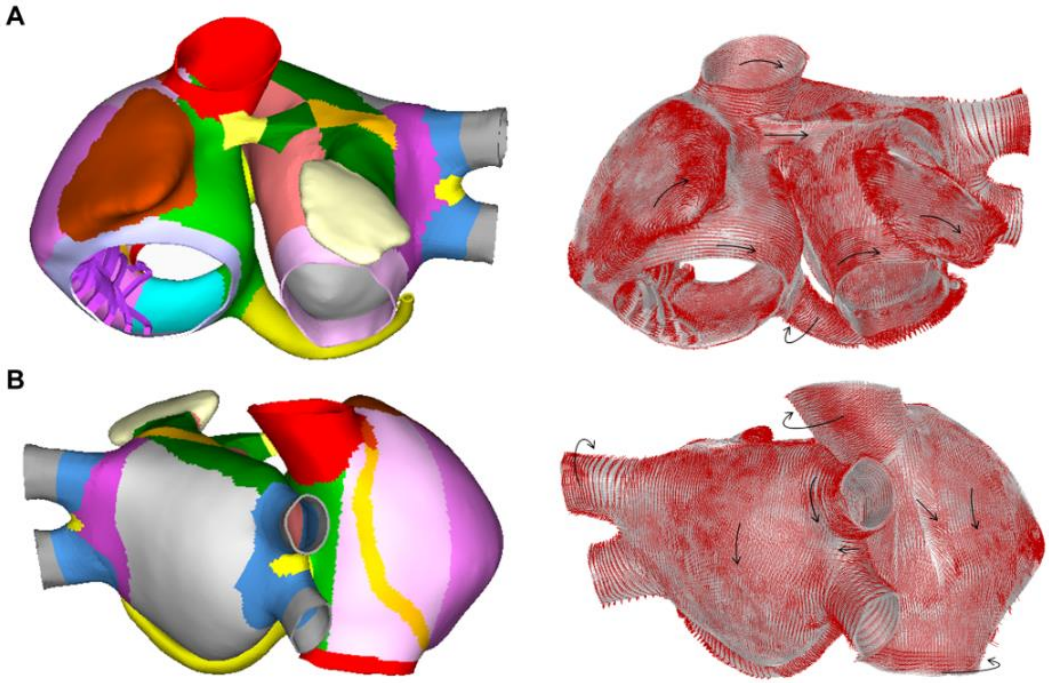

Figure 2.21 – 3D atria model. By (Tobón et al. 2013).
The model is divided in 42 areas depending on the atrial structure and the atrial bundles (left) and fiber orientation is defined by the red lines (right).

Atrial models were used to study the mechanisms that promote and maintain episodes of AF, similar to tissue models. Virag et al. studied rotor distribution in the presence of anatomical barriers (Virag et al. 2002) and Blanc et al. studied how alternating depolarization could be the mechanism responsible for rotor initiation in the presence of anatomical barriers (Blanc et al. 2001). Anatomical models also studied electrical and structural remodeling and their susceptibility to functional reentries (Colman et al. 2013; Kharche et al. 2008; McDowell et al. 2012). Lastly, detailed anatomical AF models were used to develop catheter ablation therapies (Blanc et al.

2001; Reumann et al. 2008) or to assess the effect of ablation lines gaps (Dang et al. 2005).

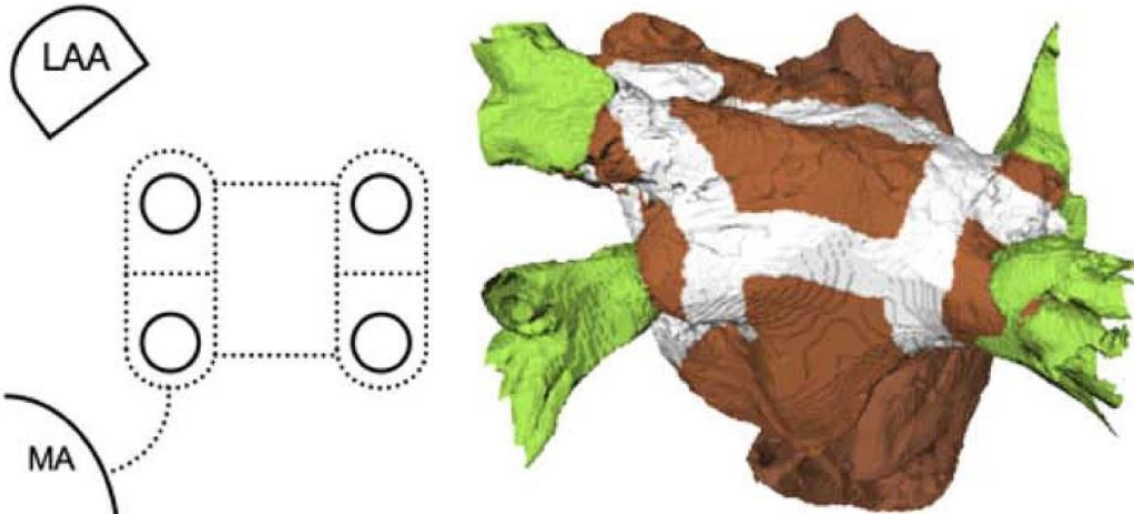

Figure 2.22 – 3D atrial model and ablation strategies. By (Reumann et al. 2008).
Ablation strategy on the left describing the pulmonary vein isolation and the ablation line from the pulmonary veins to the MA (LAA= Left atrial appendage and MA= Mitral valve Annulus). The implementation can be observed in the model: the green structures represent the pulmonary veins, the white patches represent the ablated areas and the brown volume is the rest of the atria.

Chapter 3

Complete-Chamber Conduction Velocity Estimation During Arrhythmias

3.1. Introduction

Generation and sustainment of arrhythmias are deeply conditioned by cardiac substrate properties. Although arrhythmic mechanisms are not yet fully understood, it is generally accepted that the chaotic electrical activity present in these events is caused by features such as slow conduction velocity (CV) and conduction blocks (Jalife et al. 2011; Kléber and Rudy 2004). In particular, the existence of atrial fibrillation (AF), one of the most common arrhythmia in clinical practice (John Camm et al. 2013), has been related to the nature of its structure-based substrate (Burstein and Nattel 2008; Marrouche et al. 2014). Recent consensus has pointed out that success of catheter-based ablation procedures during AF implies a substrate modification and requires of further investigations (Calkins et al. 2017). Therefore, the identification of regions that are prone to maintain arrhythmias is a key factor for the characterization of substrate properties.

Electrocardiographic imaging (ECGI) is a non-invasive electrical mapping technique that aims to reconstruct the electrophysiological activity on the heart surface from body surface potentials (Brooks and MacLeod 1997; Gulrajani 1998). It requires solving an ill-posed inverse problem and regularization of the solution (Oster and Rudy 1997; Willoughby 1979). This methodology has obtained promising results to

characterise arrhythmogenic substrates as ischemia (Álvarez et al. 2012; Wang et al. 2013) and dominant high-frequency regions (Pedrón-Torrecilla et al. 2016). Thus, ECGI may be a promising tool with the enough spatial resolution to describe other atrial substrate properties as CV. In clinical practice, CV measurements may provide a biomarker to identify slow conduction zones, where fibrosis or altered cell-to-cell coupling exists, being prone to form reentrant circuits and anchor regions for rotors (Honarbakhsh et al. 2019). However, the current generation of clinical electroanatomic mapping systems does not support the real-time construction of conduction velocity maps, necessitating off-line manual analysis (Cantwell et al. 2015), and making difficult the use of this metric during catheter ablation cases.

The CV measurement describes the speed through the direction of propagation of an action potential wavefront across excitable cardiac tissue. It can provide important quantitative information about the structure, fiber orientation of the myocardium and the properties of the intrinsic substrate; factors that may help to elucidate potential arrhythmogenic mechanisms (Cantwell et al. 2015; Roney et al. 2019). At first glance, the approach to measure CV over atrial chambers might appear obvious; detecting the activation of a wavefront at different times and dividing the distance travelled by the time interval. Following this, several approaches have been tested during sinus rhythm in atria (Cantwell et al. 2015; Dallet et al. 2018). However, the complexity of activity during fibrillatory rhythms, where trajectories can be chaotic, makes this measure challenging. Furthermore, the complicated atrial morphology geometry handicaps the feasibility of other proposed methods (Bayly et al. 1998; Kay and Gray 2005), suitable for analyzing re-entrant activity in 2-D regular grids as optical mapping recordings.

In order to determine CV during simple and complex rhythms, this study presents a method that remeshes 3D geometries to obtain a uniform sampling domain, which is able to represent the inserted nodes as a new domain, i.e. a square 2D grid. Using the gradient of phase information to obtain the direction normal to the wavefronts and storing them in the 2D grid, the paths that excitation wavefronts follow are traced with a streamline approach over the generated vector field and CV is estimated over each path projected to the original geometry. The estimated CV, orientation of vector fields, and wavefront velocities are then translated to the whole local myocardial surface.

This study is divided in two parts. First, the estimation of the propagation velocity during simple rhythms and atrial anatomies is presented, and a systematic evaluation is

undertaken. Then, the proposed methodology is tested in an ECGI context using data from an in-silico AF model and compared with ECGI target parameters (as dominant frequency) carried out on clinical data.

3.2. Methods

3.2.1 Remeshing Data in Uniform sampling domain

Geometric models tend to have complex connectivity between their nodes due to their irregular disposition. In order to recreate similar measurement conditions between different models, a remeshing algorithm to homogenize the geometries was implemented. This methodology uses parametrizations of the models in a spherical domain (Choi, Lam, Lui 2015), and it permits to resample the data in this domain and reorganize the data in a uniformly spaced 2D grid with simple boundary symmetries (Praun and Hoppe 2003). This equivalent planar domain is called geometry image (Gu, Gortler, Hoppe 2002). A modification of the remeshing workflow of this method was introduced to conserve the nodes of the original geometry. From the electrophysiological perspective, the nodes of the geometries contain relevant information, and thus, they need to be preserved to keep that data in the source position. Once the spherical parametrization is obtained, the associated nodes to the uniform domain are inserted and connected as it can be seen in Figure 3.1. The connectivity between nodes is optimized using a convex hull algorithm over the spherical surface (Barber et al. 1996). Thus, the final geometry is composed of the original and new nodes corresponding to a regular distribution.

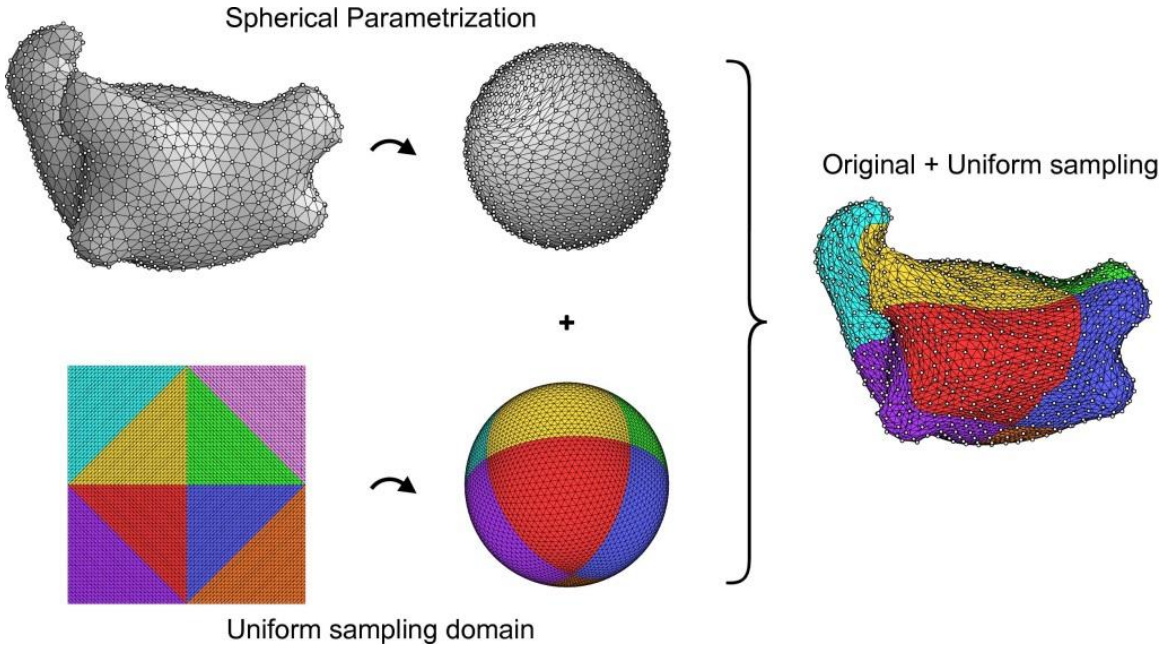

Figure 3.1 – Remeshing process using spherical parametrizations.

Illustration of the methodology for remeshing 3D surfaces to uniform planar domains.

An interpolation method for triangulated 3D surfaces was used to calculate the values at all unknown vertices of the mesh using the source known values (Amidror 2002). The interpolated data using this approach has the advantage of being able to be represented as geometry image configuration. Figure 3.2 shows examples of the benefit of such approach, which permits a uniform representation and efficient storage of the data. Therefore, this equivalence can be used as an exchange platform between the 3D surface and 2D plane domains.

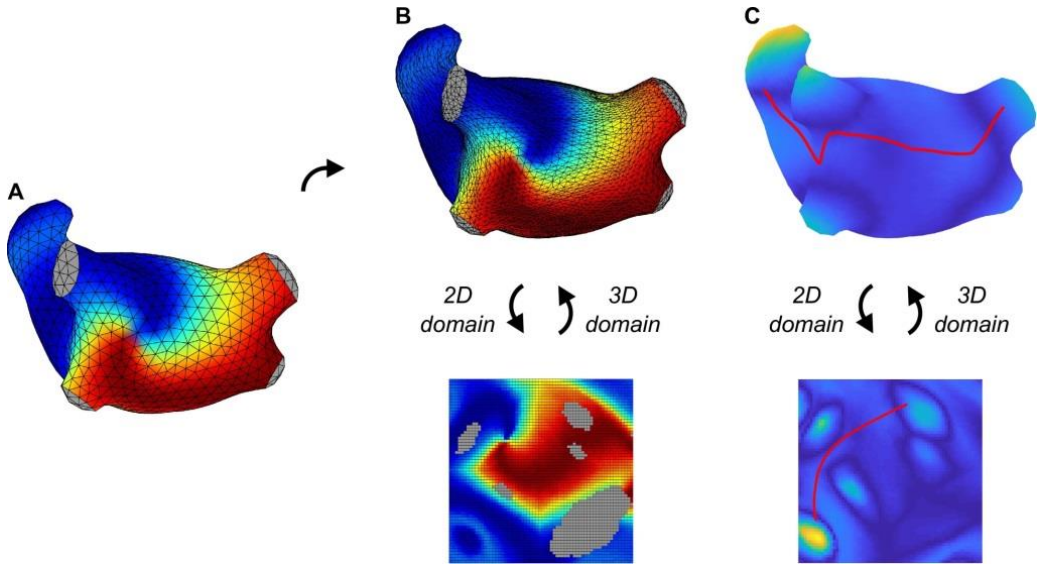

Figure 3.2 – Equivalence between the 3D surface and 2D plane domains.

Example of the interpolated data on the remeshed surface and linear interpolation of new points/trajectories into the evenly spaced grid and over the surface.

3.2.2 Conduction Velocity Estimation

The estimated CV method is based on the hypothesis that the direction of propagation is normal to the wavefront. A similar approach has been described to measure curvature and velocity of a vector field in a 2D grid (Kay and Gray 2005). However, when the wavefronts are observed at a 3D surface, the mixture of normal vectors projected on the cardiac surface will result in an observable propagation velocity. The different steps of this methodology are depicted in Figure 3.3. Calculation of CV requires obtaining the sequence of activation times without aberrations and avoiding time leaps that introduce failures in the estimation. Ideally, isochrones could be used to extract the spatial isovalues to define the propagation fronts. However in case of complex rhythms, obtaining a coherent activation map remains as a challenge. Therefore, the instantaneous phase transformation was used to delineate wavefronts and avoid time leaps in the next steps.

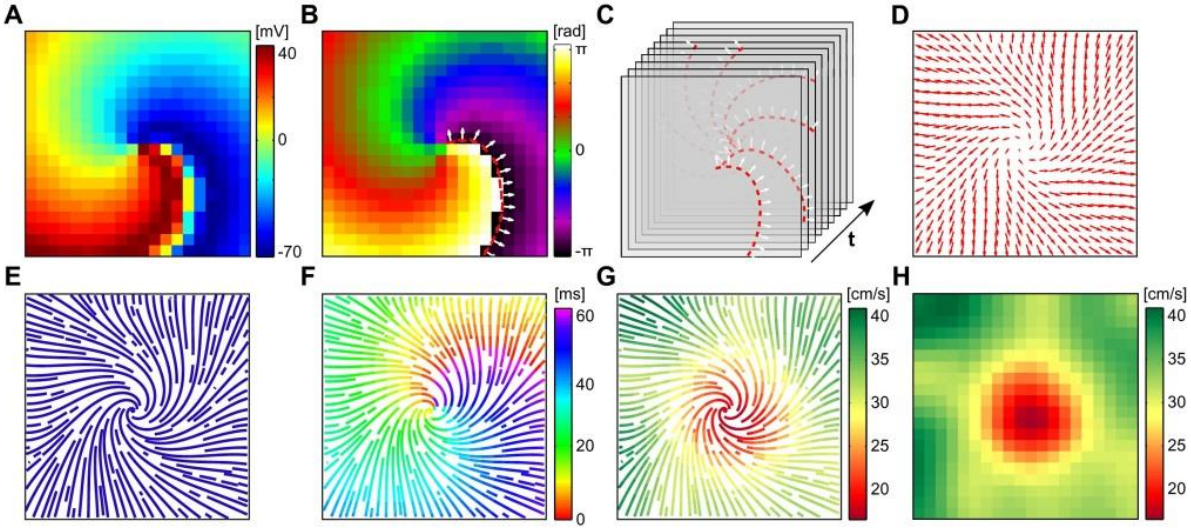

Figure 3.3 – Workflow of the CV method on a reentry simulation.

(A) Amplitude voltage map of a reentry. (B) Instant of the phase transformation and wavefront detection. (C) Reconstruction of the vector field during an interval of 60 ms. (D) Computed streamlines of the vector field. (E) Reconstruction of the activation times sequentially ordered using the pathline trajectory. (F) Cross-section view of the

reconstruction of the activation times. (G) Conduction velocity computed in steps of 5 ms over each pathline. (H) Projection of the averaged magnitude of the velocity in each original pixel.

The phase of each signal was calculated using the phase operator of the Hilbert transform (HT) (Rodrigo et al. 2015; Zlochiver et al. 2008). The phase signal ranges from 0 to 2π and represents the relative delay of each signal in one period.

$$Phase\ signal\ = \angle(\ HT(\ Signal\ )) \qquad (3.1)$$

To obtain the direction of propagation over 3D surfaces, the surface gradient was applied. For a surface S with the scalar field u contained in it, the surface gradient is defined as:

$$\nabla_S u = \nabla u - \hat{n}(\hat{n} \cdot \nabla u) \qquad (3.2)$$

where $\hat{n}$ is a unit normal to the surface.

The calculation of isophase lines was performed until all the values of normal vectors were computed during a custom interval of time, obtaining a vector field (Figure 3.3C). Vector fields were constructed using the gradient over the uniform 2D grid, using the methodology explained in the previous section (Figure 3.3D).

Generated vector fields were interpreted as a flow field, where streamlines were calculated. Streamlines are composed of pathlines, trajectory curves of individual particles that are instantaneously tangent to the direction vectors (Figure 3.3E). Displayed trajectories can be used as a guide to reconstruct coherent distributions of activation times during the time interval under study. In Figure 3.3F, activation times are been sequentially ordered using the pathline trajectories. The velocity was computed in steps of 5 ms using the isochrones previously calculated and the distance covered over each pathline of the surface (Figure 3.3G). In Figure 3.3H, a nominal CV map was created projecting the values of each trajectory over the regular grid.

3.2.3 Synthetic data model

In order to obtain a gold standard to check the accuracy of a CV measurement method, two propagation scenarios were recreated with self-imposed isochrones over the surface of two 3D geometries: (i) a sphere composed of 602 nodes, chosen for testing the methodology in a simple geometry, and (ii) a more complex one representing a left atrium with 977 nodes. The simulated isochrones maps were generated calculating the geodesic distances over the surfaces of the models (Bommes and Kobbelt 2007), and these distances were multiplied by different factors (1, 1.33 and 2) in contiguous zones to obtain dependent activations times with the geodesic distance, which result in exact velocities of 100, 75 and 50 cm/s.

3.2.4 Effects of spatiotemporal resolution

To test the accuracy of the methodology depending on the resolution during the remeshing process, the previous models were measured varying the number of introduced nodes. The amount of nodes was increased in function of the ratio of octahedral sampling $(2^{n+1}+1)^2$ used during the spherical parametrization from 25 to 66,049 nodes (n from 1 to 7).

Estimated values of CV in the original nodes were calculated using two methodologies, applying a linear interpolation or calculating the median using the 100 nearest measures of the pathlines to each node in both cases.

To evaluate the similarity between the real (x) and estimated ($\hat{x}$) measures, we use the Pearson's correlation coefficient (CC) and the relative difference measurement star (RDMS) is computed using all the nodes. The RDMS is computed as

$$\mathrm{RDMS} = \sqrt{\sum_{k} \left(\frac{x_k}{\|x^2\|} - \frac{\hat{x}_k}{\|\hat{x}^2\|} \right)^2} \qquad (3.3)$$

3.2.5 Mathematical model

A realistic 3D model of the atrial anatomy composed by 284,578 nodes and 1,353,783 tetrahedrons (673.4±130.3 μm between nodes) was used to simulate the

atrial electrical activity during sinus rhythm and atrial fibrillation (Figuera et al. 2016). A gradient on the electrophysiological properties of the atrial myocardium, specifically on $I_{k,ACH}$, I_{K1}, I_{Na} and I_{CaL} currents, was introduced into the atrial cell formulation on left atrium to obtain propagation patterns with different CV values. Computations were performed on a GPU Tesla K20 (5GRAM DDR5) using Forward-Euler algorithm with a fixed time step of 0.01 ms.

For each simulation, a uniform mesh of unipolar EGMs was calculated at 1 mm from the epicardial surface under the assumption of a homogenous, unbounded and quasi-static conducting medium by summing up all effective dipole contributions over the entire model. To calculate the local activation time of the EGM of each node, the maximum negative deflexion (maximum negative dV/dt) was taken.

The ECG potentials on the torso model were calculated by solving the Forward Problem in a mesh formed by 771 nodes and 1538 triangular patches, in which the atrial model was co-located within the torso by using the images from the Visual Human Project (MacLeod, Johnson, Ershler 1991).

3.2.6 Patient data

Six patient data were recorded during sinus rhythm and AF using the Body Surface Potential (BSPM) technique (Guillem et al. 2013) and one simultaneously by invasive endocardial electro-anatomical mapping during sinus rhythm. Intracardiac unipolar electrograms and atrial anatomy were collected from the patient using both the ablation catheter (Therapy Cool Path, Abbott, St. Paul, USA) and the circular mapping catheter (Optima, Abbott, St. Paul, USA). Activation times were automatically assigned by the electroanatomical navigation system (Ensite VelocityTM Cardiac Mapping System, Abbott, St. Paul, USA), at maximum negative dV/dt, during sinus rhythm. Electrograms with maximum peak signal below 0.5 mV were removed. Multichannel electrocardiograms were recorded with 57 chest ECG leads by using a commercial system (ClearsignTM Amplifier, Boston Scientific, Natick, USA). Image acquisition, registration and processing were made following previous procedures (Rodrigo et al. 2017). Patients arrived in sinus rhythm and AF was induced using electrical burst pacing (Atienza et al. 2006). Then, a venous bolus of adenosine (12-18 mg) was administered in order to produce an atrio-ventricular block and to remove the QRS

activation during AF (Atienza et al. 2005). At peak adenosine effect, ECGs segments surrounding the longest RR interval were used for the analysis.

3.2.7 Inverse solution and CV estimation

Inverse-computed EGM (icEGM) of sinus rhythm and AF in both patient recordings and mathematical models were estimated by using the zero-order Tikhonov's method (Pedrón-Torrecilla et al. 2016; Tikhonov 1963). The optimal regularization parameter was chosen using the L-curve method (Horácek and Clements 1997b).

In sinus rhythm, activation maps were obtained from the icEGM signals of each P wave complex (Figure 3.4).

Cross-correlation between activation maps was calculated to choose the most stable activation pattern for each patient (Figure 3.5). CV estimation was performed using this selected activation pattern.

3.2.8 Dominant frequency analysis

Dominant Frequency (DF) analyses were performed on icEGM signals during AF. They were baseline-removed and low-pass filtered with a 10^{th} order Butterworth filter with a cut-off frequency of 10 Hz (Guillem et al. 2013). Power spectral density of all signals was calculated using Welch periodogram (65536 point Fast Fourier transform, 0.5 seconds-length Hamming window and 80% overlap) (Guillem et al. 2013). A histogram of the prone regions to manifest the highest DF (HDF) for each patient was calculated, dividing the signals in segments of 1 second of duration and storing the zones that showed a value greater than 0.9 in the normalized DF map of each segment. Histograms of DF maps were compared with CV maps obtained during sinus rhythm.

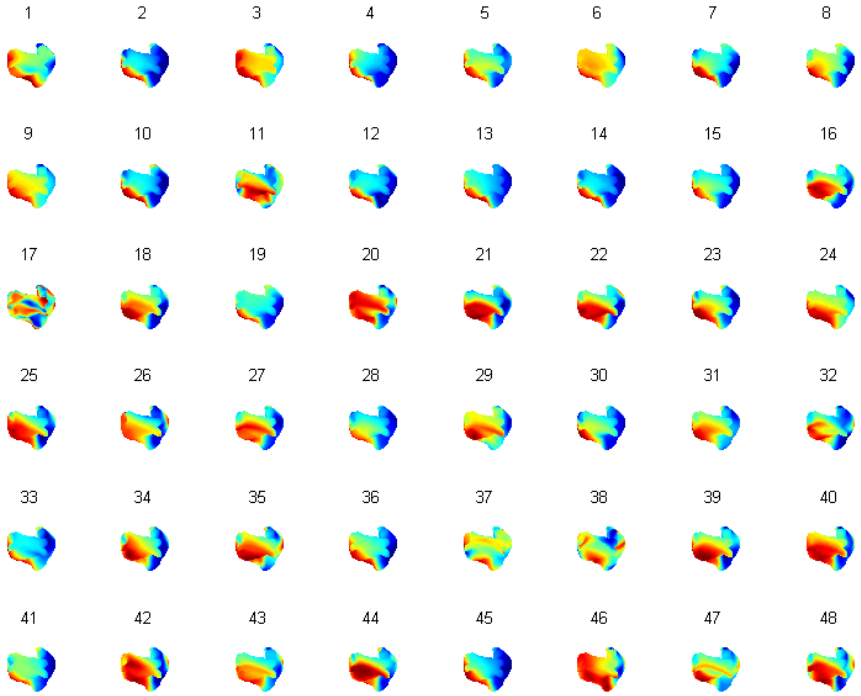

Figure 3.4 – Activation maps obtained during sinus rhythm from icEGM in a patient.

Subsequent activation time map, numbers represent the order in the signal.

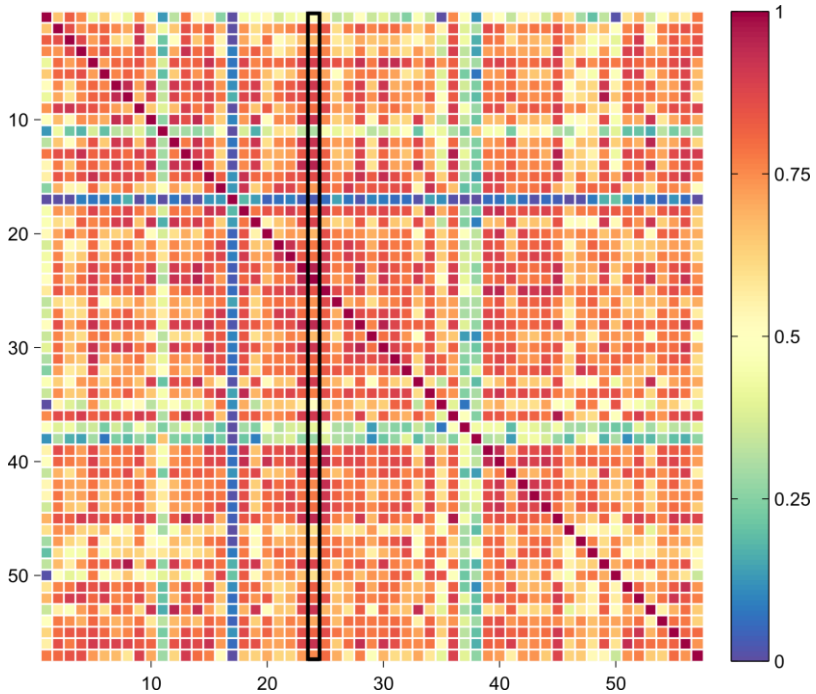

Figure 3.5 – Cross-correlation between activation maps.

Illustration of the cross-correlation between activation maps of the same patient recording, and selected.

3.2.9 Statistical analysis

Student's T–test was used to evaluate the statistical significance between continuous paired or unpaired variables, and statistical significance was considered for $p<0.01$. All data are reported as mean ± SD (standard deviation).

3.3. Results

3.3.1 Performance of conduction velocity estimation on synthetic data

The proposed methodology was first tested in a spherical model of synthetic isochrones. In Figure 3.6, the generated isochrones map and its corresponding CV map are represented in Figure 3.6A and 3.6B respectively. In Figure 3.6C, the pathlines that show the trajectories corresponding to the electrical propagation follow and the calculated CV in steps of 5 ms are displayed. The interpolation and calculation of the median was made over each original node of the sphere using the nearest 100 measures of CV data belonging to each pathline. An example of the interpolation process is shown in Figure 3.6D, making the comparison with the original data possible. The performance of the methodology depending on the resolution during the remeshing process is depicted in Figure 3.7. The increase of resolution supposed a similar performance in both processes with CC > 0.99 from n = 4, equivalent to 1089 nodes added (Figure 3.7A). In terms of RDMS, differences were the smallest around n = 6, being the median approach the best performance with a RDMS = 0.096 (Figure 3.7B).

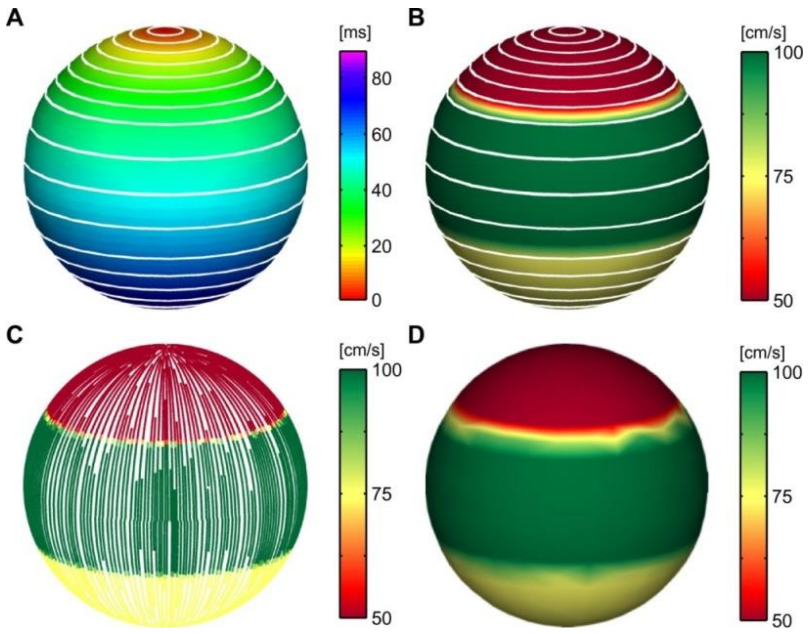

Figure 3.6 – Estimation of conduction velocity in a sphere with synthetic data.

(A) Generated activation map, white isolines represent steps of 5 ms.(B) Exact nominal value of conduction velocity of the generated isochrones. (C) Estimation of CV with the proposed methodology. (D) Projection of nominal value of CV estimated.

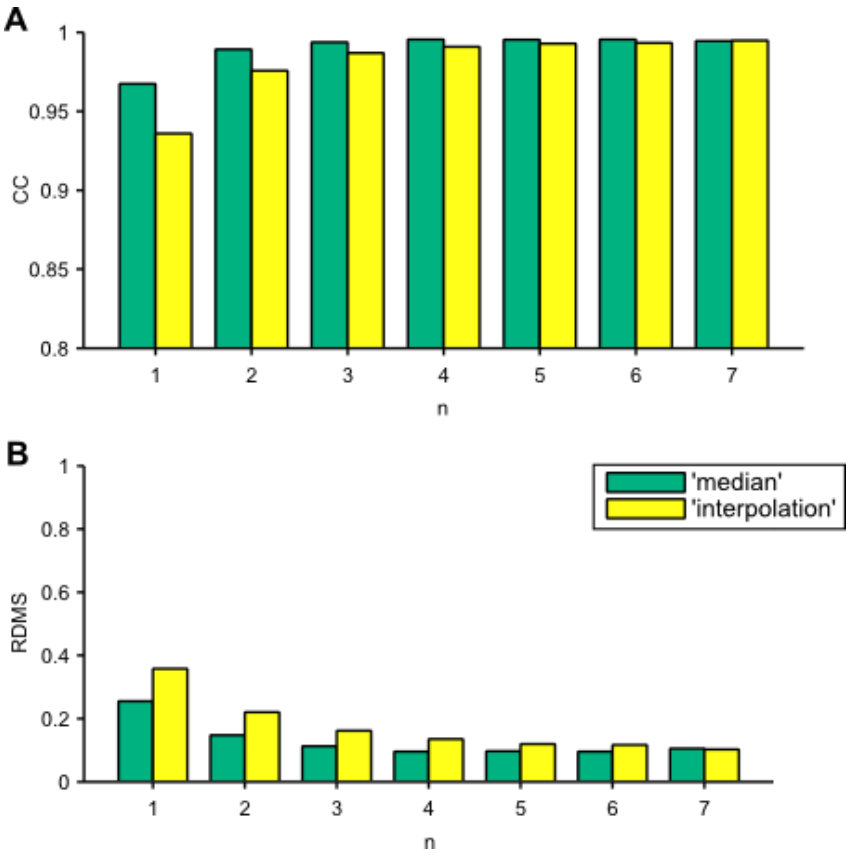

Figure 3.7 – Performance metrics of CV estimation in a spherical model.

(A) Pearson's correlation coefficient. (B) Relative difference measurement star.

Next, a similar approach was done using a LA model of synthetic isochrones how is shown in Figure 3.8. The generated isochrones map (Figure 3.8A) and its corresponding CV map (Figure 3.8B) were done with the same methodology as the spherical model and are represented. The CV pathlines and an example interpolation of CV are displayed in Figure 3.8C and 3.8D respectively. Figure 3.9 shows the evolution of the metrics depending of the resolution in same way that the previous case. The increment of geometric complexity due to the left atrium model supposed degradation in both metrics in comparison to the spherical model. CC and RDMS exhibited a better performance using the median value that the interpolation, being the best resolution n = 6 (equivalent to 16641 nodes added) in both processes with CC = 0.994 and RDMS = 0.107 for the median vs. CC = 0.985 and RDMS = 0.175 with the linear interpolation.

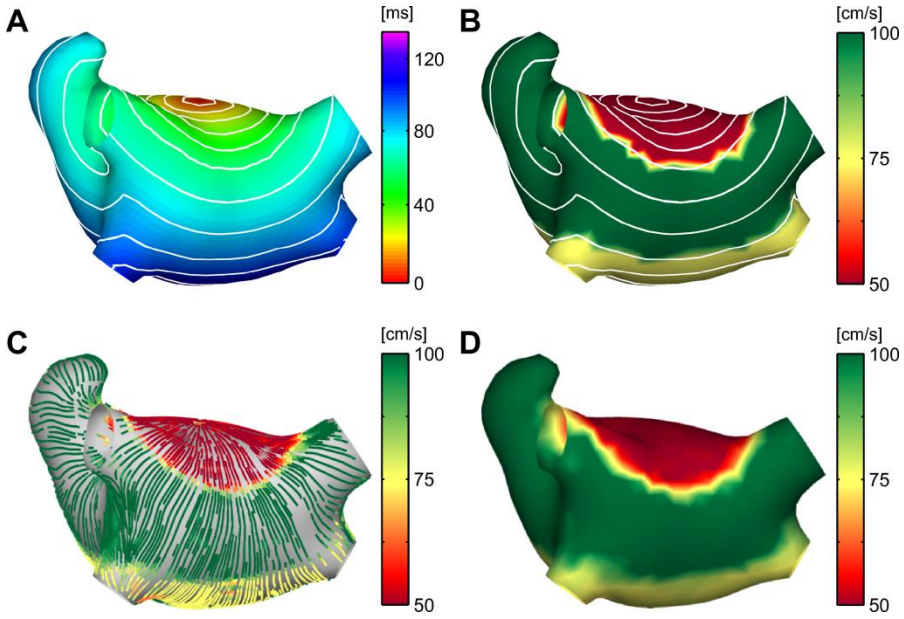

Figure 3.8 – Estimation of conduction velocity in a left atrium model with synthetic data.

(A) Generated activation map, white isolines represent steps of 10 ms. (B) Exact nominal value of conduction velocity of the generated isochrones. (C) Estimation of CV with the proposed methodology. (D) Projection of nominal value of CV estimated.

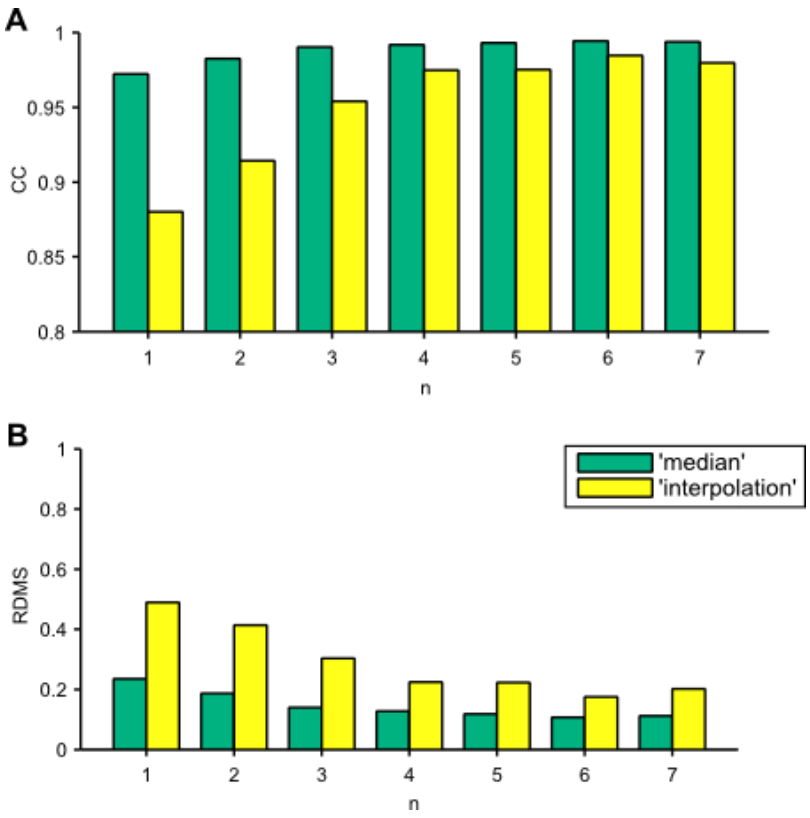

Figure 3.9 – Performance metrics of CV estimation in a left atrium model.

(A) Pearson's correlation coefficient. (B) Relative difference measurement star (RDMS).

3.3.2 Results on realistic computer model

After verifying the feasibility of CV measurement in a controlled model, realistic models of atrial fibrillation with remodeled tissue were tested. First, CV measurements were measured on the model directly during sinus rhythm and after initiating a simple reentry as shown in Figure 3.10. In both rhythms, slowest CVs were present on the left pulmonary veins coinciding with the region where the remodeled gradient was introduced (Figure 3.10A). The isochrone map for both environments is represented together with the trajectories and the CVs projected. It can be observed that the gradient of CV, that presents lower CV at the left atrium than at the right one, is maintained despite the fact that different activations take place at different rhythms and trajectories. This result was achieved after stimulating at 1 Hz on the right atrium during sinus rhythm and, as a consequence, fibrillation is maintained at 4.5 Hz on left atrium. The confidence interval of the CVs distributions was from 41.08 to 161.95 cm/s

for sinus rhythm and from 29.83 to 150.80 cm/s for AF. A lower CV during higher rhythms of stimulation is in agreement with the characteristics of restitution of cardiac tissue.

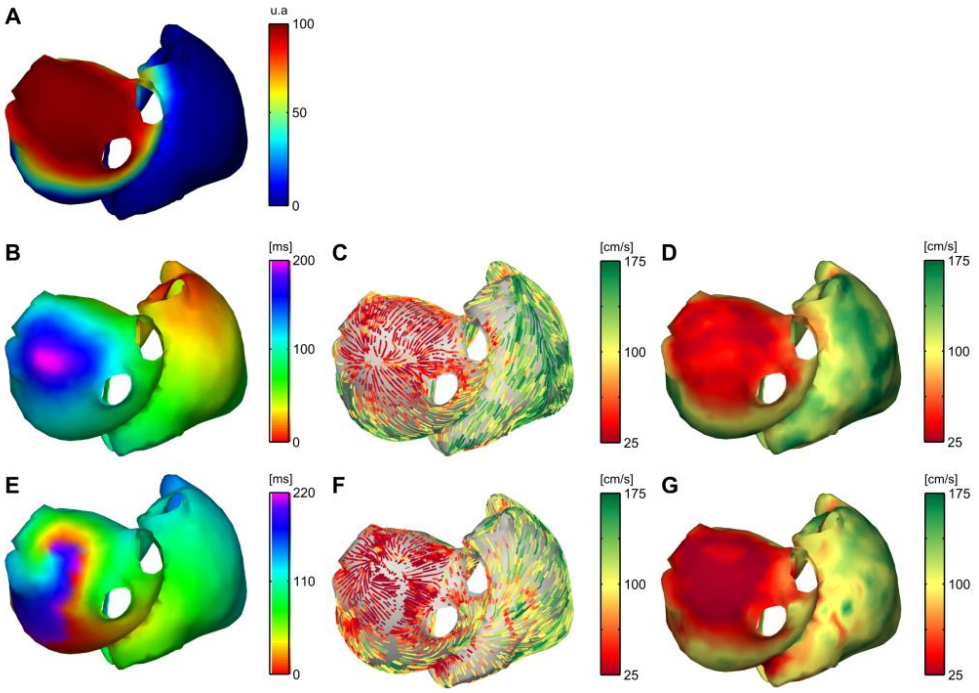

Figure 3.10 – Relationship between the estimated CV in sinus and fibrillatory rhythms from the raw signals.

(A) Remodeling gradient distribution, left atrium has a 100% of remodeling and right atrium is not remodeled. (B) Acquired activation map during sinus rhythm. (C) Estimation of CV with the proposed methodology during sinus rhythm. (D) Projection of nominal value of CV estimated during sinus rhythm. (E) Acquired activation map during AF. (F) Estimation of CV with the proposed methodology during AF. (G) Projection of nominal value of CV estimated during AF.

Next, the same process was repeated after ECGI estimation on mathematical models outcome. Figure 3.11 shows the performance of the CV calculations for this case. It can be noticed that isochrones maps obtained (Figure 3.11A and 3.11D) differ slightly and show artifactual jumps in comparison with the activation times computed directly on the model. These errors were dragged during the calculation of the trajectories and CV estimation. The performance of metrics between the obtained isochrones had a CC = 0.989 and RDMS = 0.146 for sinus rhythm and CC = 0.981 and

RDMS = 0.195 in the case of AF. However, the confidence interval of the CV distributions was from 24.62 to 182.46 cm/s for sinus rhythm and from 18.81 to 162.17 cm/s for AF, and gradients between both atria are more blurred in this case. Being the metric performance, CC = 0.867 and RDMS = 0.515 comparing the sinus raw model with its ECGI outcome and CC = 0.872 and RDMS = 0.506 in the case of AF.

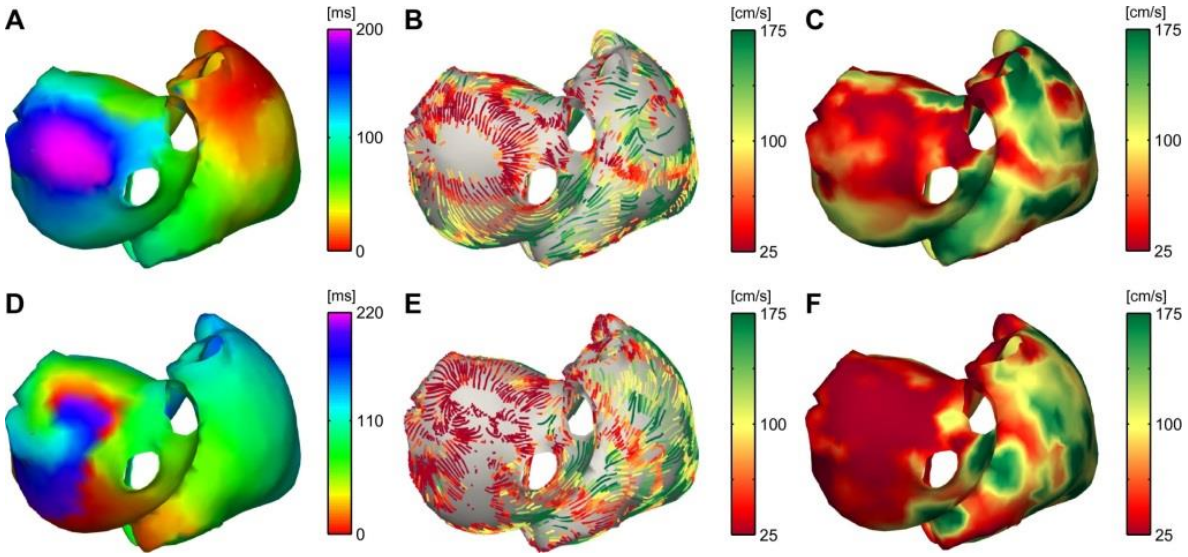

Figure 3.11 – Relationship between the estimated CV in sinus and fibrillatory rhythms from the ECGi signals.

(A) Acquired activation map during sinus rhythm. (B) Estimation of CV with the proposed methodology during sinus rhythm. (C) Projection of nominal value of CV estimated during sinus rhythm. (D) Acquired activation map during AF. (E) Estimation of CV with the proposed methodology during AF. (F) Projection of nominal value of CV estimated during AF.

3.3.3 Results on clinical data

Figure 3.12 exemplifies the application of the methodology on the invasively recorded endocardial EGM and reconstructed ECGI from clinical data. The endocardial EGM were recorded during slow stimulation (1 Hz) from right atrium and the reconstructed ECGI were taken during regular sinus rhythm and after AF induction. Figure 3.12A-C shows activations maps computed from the different recordings.

Isochrones from endocardial EGM show a clear slow region close to the left superior pulmonary vein and inferior pulmonary vein, but after CV estimation, the slow region can be also delimited over right inferior pulmonary vein (Figure 3.12D). Despite activation patterns are different during ECGI recording during both sinus rhythm and AF (Figure 3.12 B and D respectively), a similar CV pattern is observed around pulmonary veins (Figure 3.12E and 3.12F). In addition, the biggest difference is observed in the appendage.

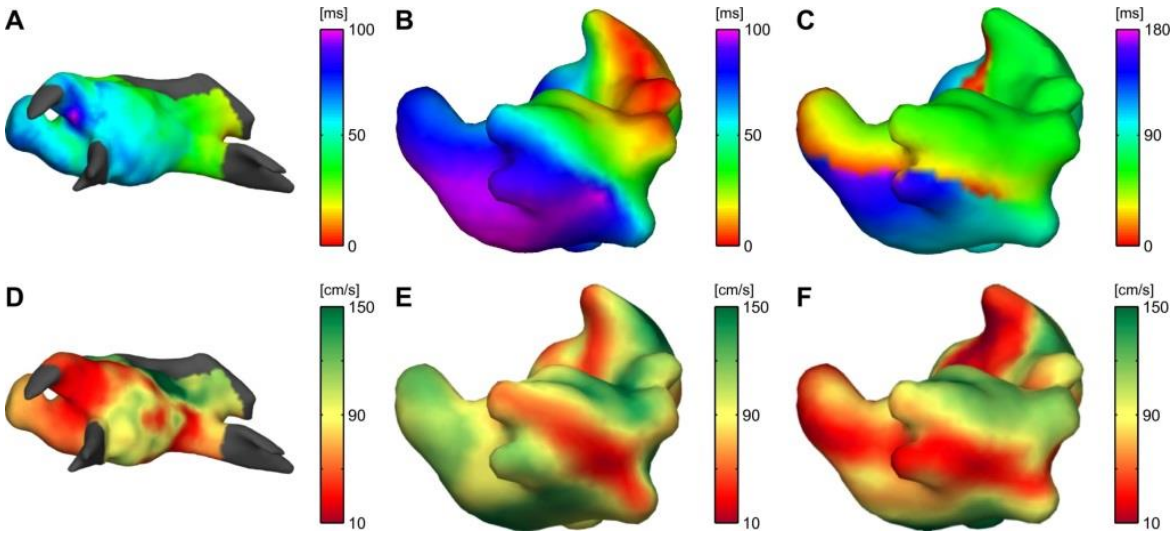

Figure 3.12 – Relationship between estimated CV in sinus and fibrillatory rhythms in patient data of different sources.

(A) Recorded activation map by the electroanatomical navigation system during pacing at 1 Hz. (B) Acquired activation map during sinus rhythm using ECGI signals. (C) Acquired activation map during AF using ECGI signals. (D) Estimation of CV during pacing . (E) Estimation of CV during sinus rhythm using ECGI. (F) Estimation of CV during AF using ECGI.

To assess if it exists some relationship between the estimated CV and other classical parameters calculated from ECGI of patients, the collected data of 5 patients was examined. Therefore, the recurrence of HDF areas during complex rhythm were compared to CV maps obtained during simple rhythms. Figure 3.13 shows the comparison between histogram of HDF obtained from ECGI reconstruction AF segments and the estimated CV during sinus rhythm previous to AF induction. It can be observed that regions with more recurrence of HDF are above slow CV regions.

In patients, the confidence interval of the CVs distributions was from 15.67±4.9 to 156.78±3.7 cm/s. Areas with larger DF recurrences were in areas of low CV, below 40.6 ± 14.2cm/s, showing a good spatial correspondence between patients. Figure 3.14 shows this trend on the patient data, where atrial areas prone to have high activity sustained in time, above 85% of time, match with low CV areas measured during sinus rhythm. Other regions with less capacity to maintain the high frequencies have more variability in their propagation properties.

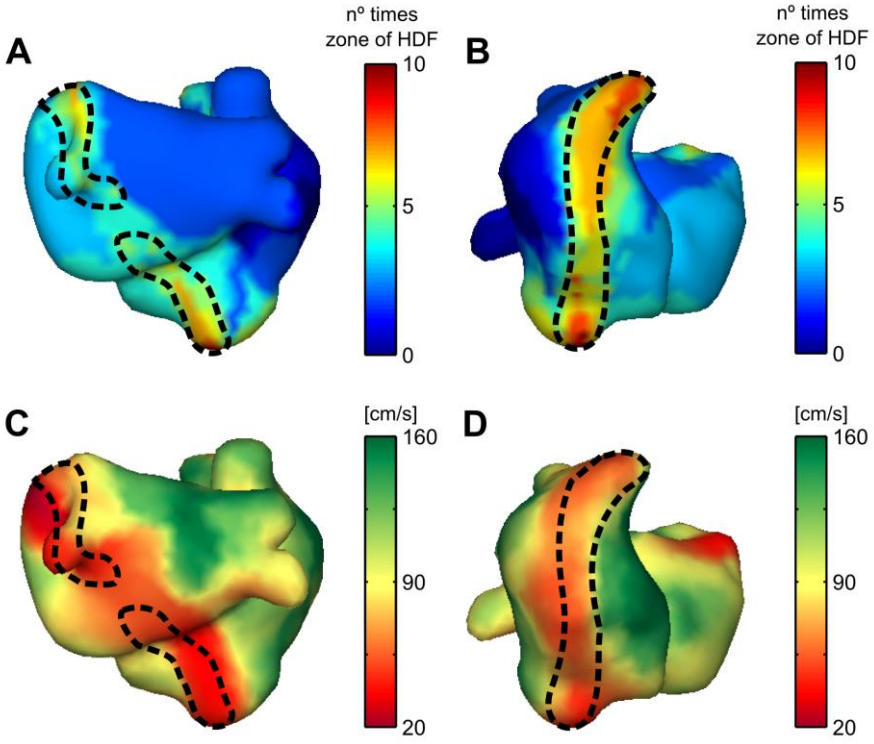

Figure 3.13 – Comparison between CV during sinus rhythm and recurrence of DF during fibrillatory rhythms in patient data.

(A) Recurrence of HDF from posterior view of the left atrium. (B) Recurrence of HDF from anterior view of the left atrium. (C) Nominal value of estimated CV from posterior view of the left atrium. (D) Nominal value of estimated CV from anterior view of the left atrium. Dash lines highlight regions with more recurrenceof HDF.

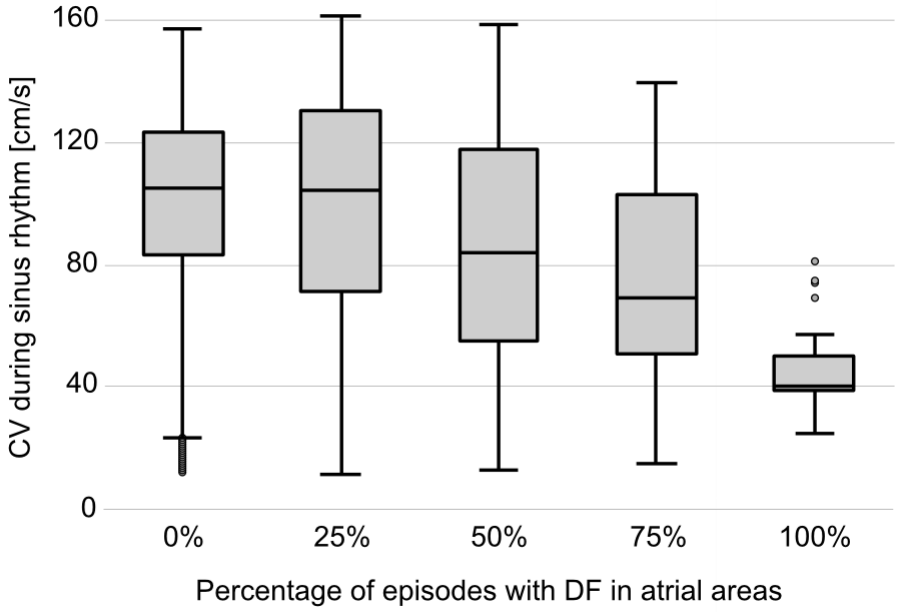

Figure 3.14 – Estimated CV according to the rate of recurrence of episodes with DF.

3.4. Discussion

3.4.1 Main findings

A novel methodology to estimate conduction velocity during irregular cardiac activation patterns has been proposed and its applicability was tested in three different scenarios: simulated data, computer simulations of atrial fibrillation and ECGI recordings.

The novelty of this methodology includes its application on atrial fibrillation recordings, which is the arrhythmia with most prevalence worldwide and with current treatments of limited efficacy. The method allowed the estimation of CVs during simple and fibrillatory patterns on realistic atrial geometries. The analysis from ECGI has been validated with intracardiac recordings. In addition, this proof of concept, demonstrates that this novel technology could serve to stratify AF patients based on the areas of lower CV.

3.4.2 Performance of Conduction Velocity Estimation

The main drawback of the already existing techniques for measuring CV is the lack of precision construing the activation front. Determining the activation sequence in arrhythmic process or errors related to the fitting process always derive on individual interpretation of the calculation for each segment. Our algorithm uses the advantages of the instant phase transformation, previous to the fitting process, to extract the spatial distribution of the propagation front. Through this process, it is possible to build a structure to guide the reconstruction of a coherent map of electrophysiological parameters as activation time, and thus speed of the propagation. Examples displayed have shown how our CV mapping is able to identify substrates, such as anchoring zones, collision of wavefronts and remodeled substrate of risk.

Implementing a strategy that is able to reconstruct coherent maps and interpret CV in the current mapping is a promising tool for the understanding arrhythmic mechanisms and helping to the correct diagnosis and treatment of arrhythmias. Such concepts will be adapted and integrated in future studies.

3.4.3 Noninvasive diagnosis from the surface ECG

The suggested technique for identifying atrial tachyarrhythmias can be used in clinical practice. Endocardial information from advanced electro-anatomical imaging devices will also be needed to validate the proposed algorithm. This technique can also be implemented to ventricular tachyarrhythmias to recognize tissues and infarcts that are composed by structures that trigger and maintain tachycardia reentrants, speeding down the wavefront of stimulation and offering unidirectional blockage. However, only information acquired from a surface computer model and atrial arrhythmias were validated in the current research. In figure 3.12, we can see that the activation maps of endocardial activity registered invasively and the reconstructed epicardial propagation maps are comparable.

3.4.4 Limitations and future work

Indeed, the CV vector field over 3-D surface mesh is the projection of the combination of velocity from the cardiac tissue.

The presented evaluation of AF conduction velocity measurements allowed the validation with intracavitary signals, but this was a first proof of concept study that requires a larger database to confirm the robustness and the clinical applicability of the method.

3.4.5 Conclusion

In the present study, we have developed a method that allows the estimation of CV during simple and fibrillatory patterns on realistic atrial geometries. The use of CV maps obtained from our algorithm gave new information and interpretation of results to the existing in the clinical procedure with intracavitary recordings. Therefore, this methodology could serve to stratify AF patients and change the clinical management of patients.

Chapter 4

Characterization of events prior to the initiation of fibrillation

4.1. Introduction

The initiation of ventricular arrhythmias is promoted by the presence of (i) dynamic factors and (ii) a heterogeneous substrate, e.g. structurally abnormal hearts or myocardial ischemia, which allows the maintenance and perpetuation of the arrhythmia (Hayashi, Shimizu, Albert 2015). Dynamic factors are related to the ability of a region to show electrophysiological time variations between beats, associated with steep conduction velocity (CV) restitution (Karma 1994; Weiss et al. 1999) and instability of calcium cycling factors (Hayashi et al. 2007; Pruvot et al. 2004). Spatial heterogeneities are due to gradients of expression levels of ion channel and transporter proteins (Opthof et al. 2017) in healthy tissue (Ashman and Byer 1943; Wilson et al. 1934), or caused by structural pathologies or ischemia (Kessler et al. 2015), manifesting three-dimensional patterns of action potential durations (APD) and ionic concentration flows, as in intracellular calcium transients (CaT).

At high cardiac rates, heterogeneous cardiac substrate leads to an arrhythmogenic behavior and electric instability, which may manifest in the form of alternans. The presence of alternans is a biomarker commonly associated with the onset of ventricular fibrillation (VF) and sudden cardiac death in clinical practice (Pastore et al. 1999). Alternans are defined as oscillations in AP and CaT amplitude and duration between successive beats, which can produce two types of spatial patterns: (i) spatially discordant alternans (SDA), when alternans in adjacent regions occur in opposite

phases, and (ii) spatially concordant alternans (SCA), if they occur in phase between the regions.

The presence of SDA is clinically relevant because the increase of heterogeneity of repolarization is assumed to be more arrhythmogenic (Pastore et al. 1999; Qu et al. 2000). Formation and progression of SDA have been closely linked to the nature of the cardiac substrate (Hayashi et al. 2007; Mironov, Jalife, Tolkacheva 2008). Moreover, some antiarrhythmic drugs have shown their effectiveness in reducing the incidence of VF by modifying these specific cardiac features (Hirayama et al. 1993; Jin et al. 2014; Riccio, Koller, Gilmour 1999; Swissa et al. 2002). However, the sequence of events and the multiple electrophysiological factors by which SDA can promote VF, and how these are modified by an antiarrhythmic treatment, have not been fully studied.

In this study, we use simultaneous optical mapping of transmembrane voltage and intracellular calcium concentration to analyze the role of these parameters on the onset of VF. More specifically, we studied the relation of reduced CVs and the spatial distribution and magnitude of alternans with the initiation of reentry and VF. In addition, these measurements were also compared with those under the administration of verapamil, an L-type calcium channel blocker which modulates the appearance of alternans and incidence of sudden cardiac death. Our main findings support that heterogeneous distribution of cardiac substrate and dynamic factors of calcium cycling at the organ level have a main role in the generation of reentry and VF, and that the therapeutic control of these factors can avoid the trigger of these events.

4.2. Methods

4.2.1 Isolated Heart Preparation

Experiments were performed in five New Zealand rabbits at Hospital Gregorio Marañon in Madrid. This study was carried out in accordance with the recommendations of the directive 2010/63/EU on the protection of animals used for scientific purposes as well as the European and Spanish regulations on the subject, after the approval by the committee of ethics in animal experimentation of Hospital Gregorio Marañon. In particular, rabbit hearts were isolated by thoracotomy after general anesthesia using pentobarbital and immersed in cardioplegic solution at 4 °C for their

transport (in mM: 140 NaCl; 5.4 KCl; 1 MgCl2; 5 HEPES; 11 Glucose; 1.8 CaCl2 with a pH of 7.4). After removal of coronary blood, hearts were retrogradely perfused through the aorta using a cannula with a constant flow of modified Tyrode's solution at 36.5 °C (in mM: NaCl, 120, NaHCO3, 25, CaCl2, 1.8, KCl, 5.4, MgCl2, 1, glucose, 5.5, H2PO4H2O, 1.2, pH 7.4). The medium was continuously oxygenated by the bubbling of carbogen (95% oxygen / 5% carbon dioxide). All compounds were purchased from Sigma-Aldrich (Dorset, UK)..

4.2.2 Optical mapping system

Hearts were infused with Di-4-ANBDQPQ voltage-sensitive dye (excitation/emission wavelength of ~640 nm/~750 nm) with an aortic bolus through the cannula of 20 μL at 35 mM (donated by Dr. Loew, University of Connecticut Health Center) for 5 minutes and 250 μL at 1 mM of Rhod2-AM calcium sensitive dye (excitation/emission wavelength of ~555 nm/~585 nm) (Biotium, Hayward, CA, USA) for 30 minutes, replacing the infusion with fresh Tyrode's solution containing 10 mM of Blebbistatin (Biotium) (Lee et al. 2012). Di-4-ANBDQPQ was excited by the use of a CBT-90-R (LED1; Peak Wavelength 628 nm, Luminus Devices, Billerica, MA, USA) LED light using an excitation-filter D640/20X (F1; Chroma Technology, Bellows Falls, VT, USA). Rhod-2AM was excited by a white light (LED2; LED-CBT-90-W65S-C11-LA100; Luminus Devices) using an excitation-filter S555/25X (F2; Chroma Technology) (Wang et al. 2015). The lights were collimated with a flat-convex lens (L1 and L2; LA1951; Thorlabs, Newton, NJ, USA). The fluorescence emission of the dyes was recorded through a specifically designed multiband filter ET585/50-800/200M (F0; Chroma Technology) plus a long-pass filter with significant transmission at wavelengths >575 nm (F0; BLP01-561R-25; Semrock, Rochester, NY, USA), placed in front of the camera lens (L0, Navitar, Rochester, NY, USA) for adequate collection of fluorescence emission (Wang et al. 2015). The voltage and calcium recordings were performed using a high-density optical mapping system based on an electron-multiplied charge-coupled device (Evolve 128 EMCCD, 128x128 pixels, 24-um-square pixels, 16 bit; Photometrics, Tucson, AZ, USA). The signal was digitized with a 16-bit analog/digital converter with a sampling frequency of 512 Hz. A diagram of the system is represented in Figure 4.1.

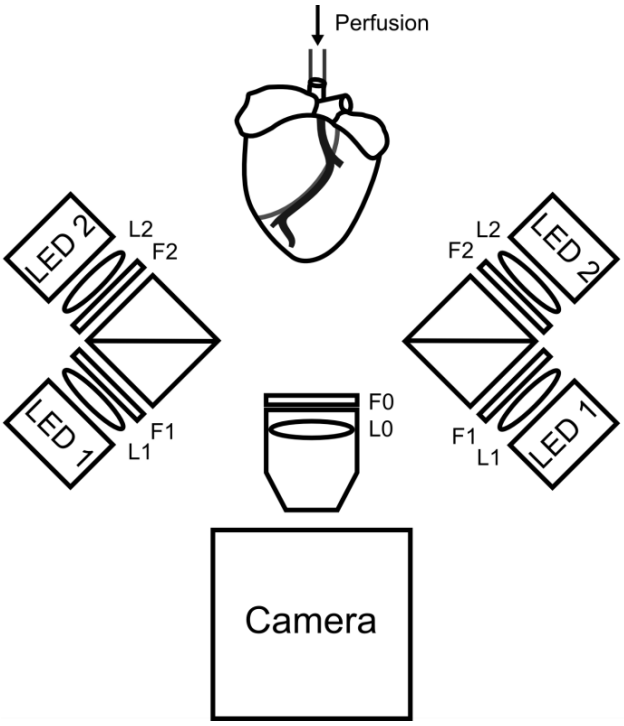

Figure 4.1 – Optical mapping system setup.

Include the perfused isolated heart, the LEDs for the excitation of the fluorescent dye, and the EMCCD camera for the recording of the emitted light with the adequate optical filters.

4.2.3 Experimental Protocol

Ventricular pacing was performed with standard clinical catheters with platinum iridium bipolar electrodes (diameter, 0.125 mm; inter-electrode distance, 1 mm). Pacing (2-ms bipolar rectangular pulses, intensity of 1-2 V twice the diastolic threshold) was carried out with a home-made high pacing unit. Hearts were defibrillated with a biphasic pulse of 30 J on the epicardium. All hearts were defibrillated after the first shock. Each animal was defibrillated only once. VF inducibility protocol was repeated after infusion of verapamil (2μM, 16.7 mg/Kg heart weight), using an aortic bolus through the cannula. The concentration was chosen in the rank in which its electrophysiological effects were observable.

A pacing protocol was applied at increasing rates, starting with a pacing cycle length (PCL) of 350ms and gradually increasing the frequency until the onset of VF (i.e. 350, 250, 200, 190, 180, 170, 160, 155, 150, 145, 140, 135, 130, 125, 120, 115,

110, 105, 100, 95, 90, 85, 80 ms). For each pacing rate, two consecutive movies of 5 seconds were recorded. Pacing protocol and movie recording was automatized to ensure the shortest duration of the experiment. In case VF was induced, pacing protocol was finalized and 6 movies of 10 seconds were recorded before the defibrillation. Total duration of the pacing protocol was less than 10 minutes. Schematic diagram of the experimental protocol is shown in Figure 4.2.

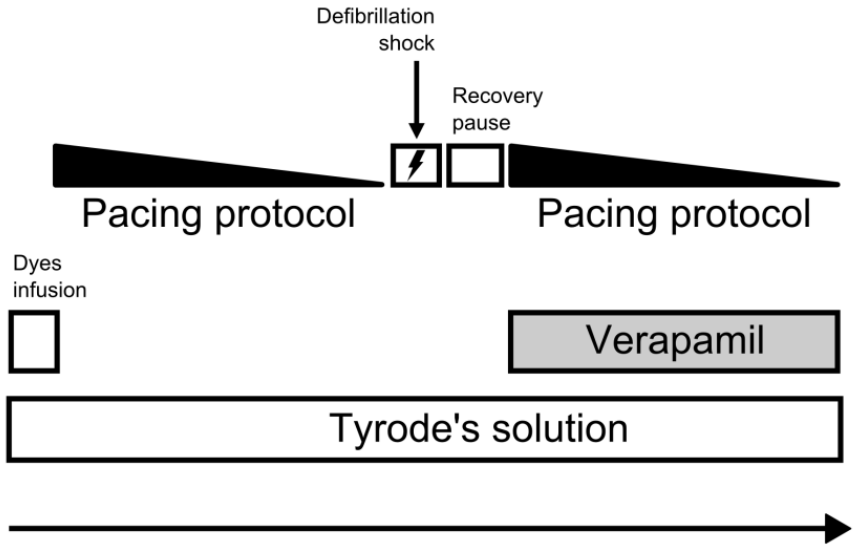

Figure 4.2 – Description of the experimental protocol.

First, the fluorescent dye was infused. Later on, the pacing protocol at increasing frequencies was applied until the heart underwent fibrillation. A defibrillation shock was later applied, and after a recovery pause, the pacing protocol was repeated under the infusion of verapamil. During the whole procedure the heart was perfused using Tyrode solution.

4.2.4 Voltage and Calcium imaging processing

Optical mapping signals were analyzed by using our customized software designed in MATLAB (The MathWorks, Massachusetts, United States). Raw data was filtered to eliminate fluorescence noise, applying a spatial Gaussian filter (size 7 × 7 pixels) and a temporal Savitzky-Golay filter (size 15 samples). For each pixel, baseline was removed by subtracting the lower envelope of the signals. Finally, voltage and calcium signals of each pixel were normalized between 0 and 1. Pixels outside the area of cardiac tissue were automatically discarded applying a user-defined mask (Laughner et al. 2012).

APDs were measured at 80% of repolarization. CaT magnitude was defined as the peak-to-peak amplitude of a calcium transient, which lies between 0 and 1 due to the pixel-by-pixel normalization.

4.2.5 Identification of Voltage and Calcium Spatial Alternans

Spatial analysis of the distributions of alternans for voltage and calcium signals was independently performed as follows: APD alternans were defined as the APD difference between simultaneous activations (Eq.1) and the CaT alternans maps as the percentual difference in amplitude of calcium transients between consecutive (n and n + 1) activations in each pixel (Eq. 2):

$$\Delta\mathrm{APD}(\mathrm{x},\mathrm{y})_{\mathrm{n}} = \mathrm{APD}(\mathrm{x},\mathrm{y})_{\mathrm{n+1}} - \mathrm{APD}(\mathrm{x},\mathrm{y})_{\mathrm{n}} \qquad (4.1)$$

$$\Delta\mathrm{CaT}(\mathrm{x},\mathrm{y})_{\mathrm{n}} = \frac{\mathrm{CaT}(\mathrm{x},\mathrm{y})_{\mathrm{n+1}} - \mathrm{CaT}(\mathrm{x},\mathrm{y})_{\mathrm{n}}}{\max(\mathrm{CaT}(\mathrm{x},\mathrm{y})_{\mathrm{n+1}}, \mathrm{CaT}(\mathrm{x},\mathrm{y})_{\mathrm{n}})} \qquad (4.2)$$

where n is a time interval between successive activation times and x, y are the pixel coordinates. Applied thresholds were defined according to already validated values (Gizzi et al. 2013; Visweswaran et al. 2013). Only differences in APD above 2 ms and CaT differences above 5% were considered. Alternans were defined as present only when the short-long-short variation was found for at least 6 consecutive beats.

The alternating phase was determined positive for long-short APDs (represented by red scale) and for high-low CaT pulses; and negative for short-long APDs and for low-high CaT pulses. The regions without alternans were defined as nodal lines and shown in white. Percentage of area covered by alternans was calculated by dividing the amount of pixels that displayed alternans by the total number of recorded pixels. Mean values (and standard deviation, SD) of APD, ΔAPD and ΔCaT parameters were computed for each recording. ΔAPD and ΔCaT areas were fitted to single exponential curves (Eq. 3):

$$\mathrm{f}(\mathrm{x}) = \mathrm{a}\, e^{bx} \qquad (4.3)$$

4.2.6 Identification of Conduction Velocities

CV was measured in each pixel of voltage optical mapping with a variation of the method presented by Bayly et al. (1998). Specifically, the workflow of CV estimation included: (1) the phase of the voltage signal for each pixel was calculated using the Hilbert transform (Liberos et al. 2016), (2) isochronal maps were obtained by detecting 2π changes in the phase, (3) a subpixel edge detector was used to identify the normal vector of propagation of wavefronts (Trujillo-Pino et al. 2013)., (4) normal vectors of propagations were used to identify wavefront trajectories and (5) CVs were computed in steps of 5ms over each trajectory of each wavefront. Distributions of CV were represented within isochrones, denoted by isolines that connect all the pixels with the same CV value.

4.2.7 Statistical Analysis

T-student test was used to evaluate null hypothesis of differences between basal and treated conditions in all 5 animals. Specifically, APD, alternans and CV were compared during basal conditions and after the administration of verapamil. P-values lower than 0.05 were considered statistically significant. All measurements are presented as mean ± standard deviation.

4.3. Results

4.3.1 Evolution of electrophysiological properties prior to VF

In order to understand the relation between the dynamic changes of electrophysiological properties and the initiation of VF, we examined the rate-dependent distributions of APD, CaT alternans and CV with optical mapping for increasing pacing rates until the development of VF.

In Figure 4.3, a representative example of the increasing complexity of spatial alternans (i.e. APD and CaT) and the time required for a signal to propagate across the epicardium at different pacing rates is shown. In panel 4.3A, lines of propagation with

a color scale representing the CV are depicted on top of isochrones emerging from the pacing point in the left ventricle. Notice the variation of CV during the propagation from the pacing point through the epicardium, forming a CV gradient with three different bands distributed along the propagation direction: 1) a slow conduction area close to the pacing point, 2) an intermediate band where CVs are higher than that in surrounding areas, and 3) a second distal region of slow conduction. Distribution of the three CV regions remained stable for all pacing rates, while mean local CV tends to decrease with increasing stimulation rates in all three regions.

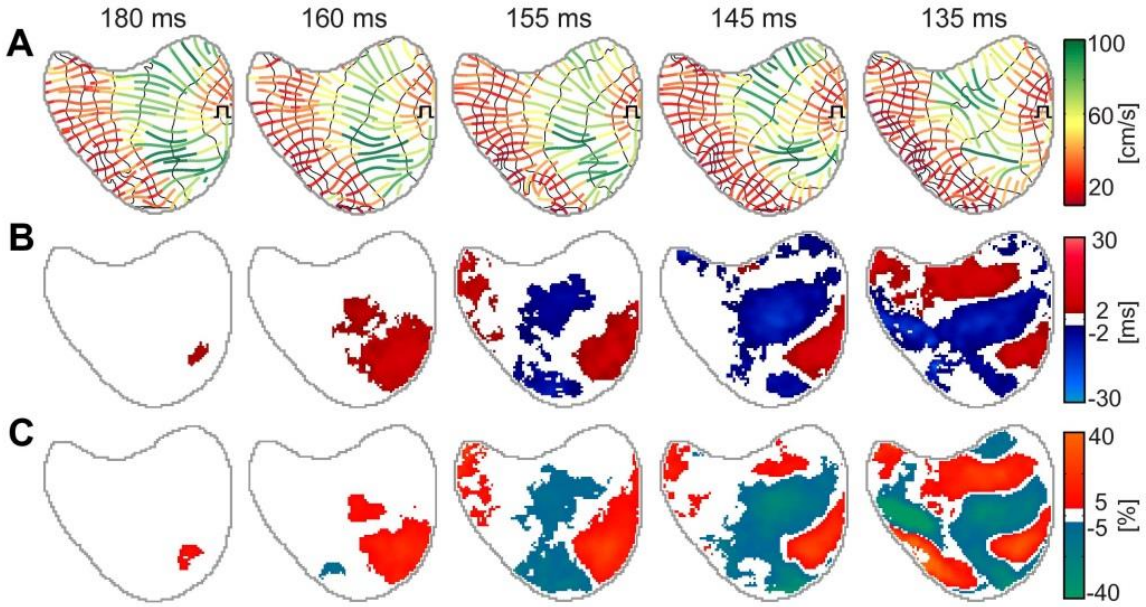

Figure 4.3 – Example of rate-dependent development of electrophysiological features obtained at different pacing cycle length in basal conditions.

(A) Distribution of local CV through the trajectory of propagation over isochrones fragmented in steps of 5 ms (black). (B) Maps of APD alternans obtained between successive wavefronts. (C) Maps of CaT alternans obtained between successive propagations.

Figure 4.3B and 4.3C show APD and CaT alternans maps respectively. The magnitude of both APD and CaT alternans and their spatial complexity are increased with the activation rate. Small isolated islets of alternans appear at PCL = 180 ms close to transition between slow and fast propagating regions. As the frequency increased, number and area of islets in the epicardial area showing alternans also increased.

Notice that, whereas for PCL of 180 ms alternans were positive in all islets, an increase in the pacing rate to 160 ms resulted in an increment in the difference of CaT and the appearance of spatial alternans with positive and negative areas (i.e. SDA). Specifically, for longer stimulation intervals, regions with SDAs were only detectable in calcium, while after an increase in the pacing rate, SDAs were also detectable in voltage. As the rate increased, the area covered by alternans grows until it covers almost the entire epicardium. We did not observe any relation between the appearance or location of nodal lines and isochrones. Interestingly, the size of each spatial alternant islet was inversely related with the distance to the pacing point; whereas spatial alternant areas close to the pacing point were large and with well-defined nodal lines, spatial alternant areas distal from the pacing point presented irregular shapes and smaller areas.

4.3.2 Mechanism of onset of VF

The previously described protocol that consisted in a gradual increase of the pacing rate allowed the induction of VF in all preparations. Under basal conditions, VF was induced at a stimulation rate of 132.5 ± 16 ms. The precursor mechanism which initiates VF can be observed in a representative example in Figure 4.4. In panel 4.4C, the sequence of isochronal maps depicts the formation of a unidirectional block (i.e. 125 ms). This unidirectional block allowed the appearance of reentrant patterns in the following isochrones and the perpetuation of the VF.

Remarkably, this unidirectional block appears in the area where (i) higher magnitudes of voltage and calcium alternans were observed and (ii) slow conduction occurred (panel 4.4B).

In all preparations the same calcium SDA trends were observed before the initiation of VF in the entire mapping area. Despite the difficulties, the specific instant of VF initiation was captured in 3 of the 5 animals. This result suggests that VF initiation was linked with a calcium dynamics mediated phenomenon.

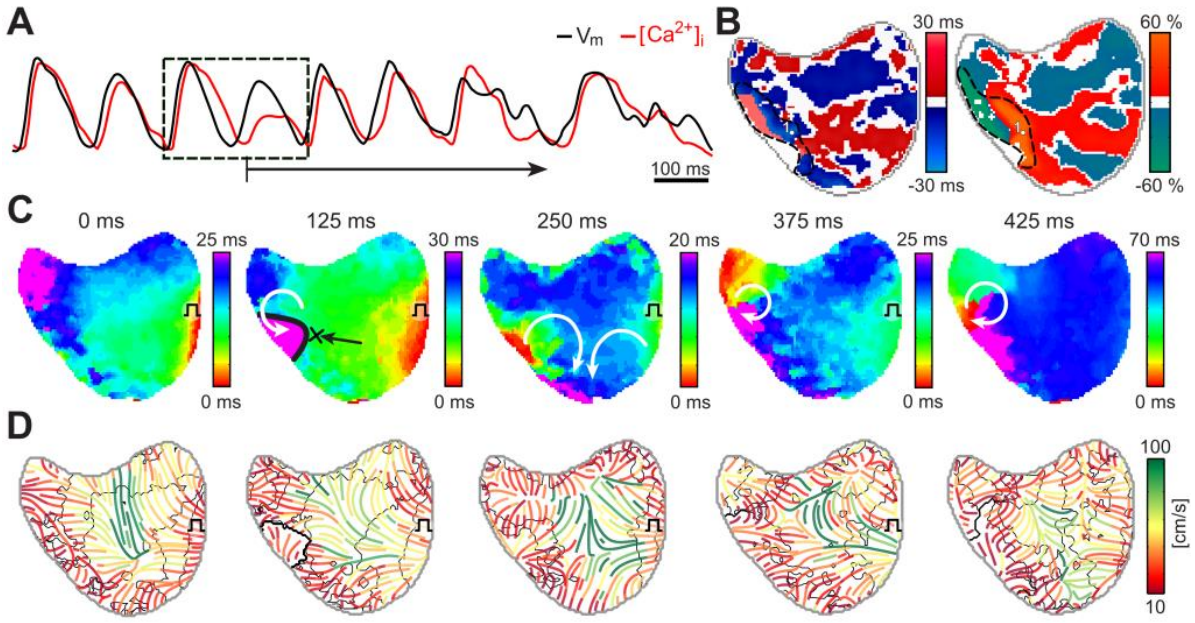

Figure 4.4 – Sequence of VF induction.

(A) Recordings of optical voltage and calcium signals of induction of VF, belonging to point 1 in panel B. (B) Distribution of APD and CaT alternans during two beats previous to the VF onset, the marked shaded line indicates the region with the highest alternans. (C) Sequence of isochronal maps corresponding to the traces depicted in panel A. Notice how during the second propagation (i.e. 9175ms) a line of block was formed. This line of block allowed the appearance of reentrant patterns in the following isochrones and the perpetuation of the VF.

4.3.3 Effect of verapamil

Previously described results indicate that during our pacing protocol calcium alternans preceded the sequence of events that produced the unidirectional block and reentrant initiation of VF. In order to evaluate the potential effect of modifying the calcium homeostasis, the previously described analysis was repeated in each preparation after the administration of a verapamil (an L-type calcium channel blocker).

In Figure 4.5A we obtained maps of voltage, calcium alternans and conduction velocity during basal conditions just before VF initiation (i.e. 140ms) and at the same pacing rate after the administration of verapamil. Notice that the existing alternans were not reproduced after drug administration; when verapamil was infused; the total area of alternans was significantly smaller, from a ΔAPD area of 76% to 19% and

ΔCaT area of 63% to 17%. Regarding the CV, the changes were not as noticeable. Panel 4.5B shows the change in morphology of action potentials and calcium transients. Notice that dual V_m/Ca^{2+} trace demonstrate a signal relationship in which the voltage signal always leads the calcium signal. This was the case in all pixels and activations both during slow and fast pacing rates.

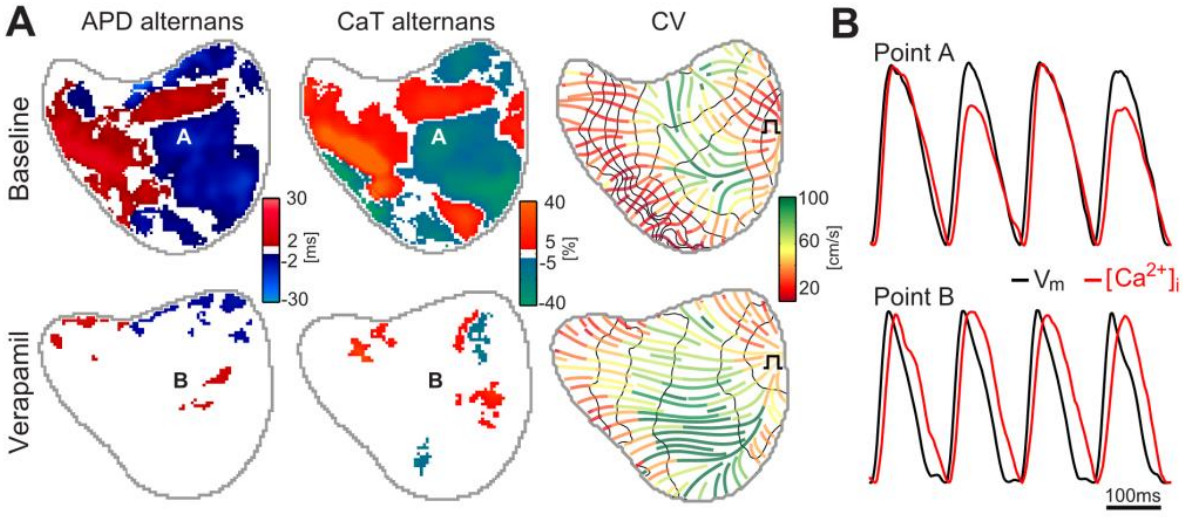

Figure 4.5 – Effect of verapamil administration on alternans and CV.
(A) Distribution of APD and CaT alternans maps together with the mean local CV at baseline, compared to same maps computed at the same pacing rate after administration of verapamil. (B) Normalized voltage and calcium optical signals of points A and B labeled on alternans maps.

As it can be observed, verapamil produced a significant reduction on the duration of action potentials and a stabilization of calcium transients, without alternans.

After the administration of verapamil, all preparations allowed faster stimulation rates before the induction of VF. A representative example of the evolution of SDA on treated preparations is shown in Figure 4.6. As expected, the increase on pacing rate was associated with a significant reduction in CV. The area covered by voltage and calcium SDA increased for fast activation rates. Interestingly, SDA patterns after the administration of verapamil presented a more patched distribution with a low correspondence between voltage and calcium alternans domains.

4.3.4 Spatiotemporal mechanisms of VF inducibility

In order to elucidate the potential role of each electrophysiological parameter on the mechanisms of initiation of VF, we examined the rate-dependent changes of APD, ΔAPD and ΔCaT magnitudes (Fig. 4.7A) and epicardial area covered by them (Fig. 4.7B), both during basal conditions and after the administration of verapamil.

As previously described by Mironov et al. (2008), during basal conditions the increase on activation rates produced a reduction on mean duration of action potentials. It is important to note that this reduction of APD was associated with higher magnitudes of APD alternans only during basal conditions. After the administration of verapamil, the magnitude of APD alternans were independent of the pacing rates. In fact, despite the significant reduction of APD produced by verapamil for slow pacing rates, those differences disappeared for fast pacing rates (i.e. 120ms and 115ms).

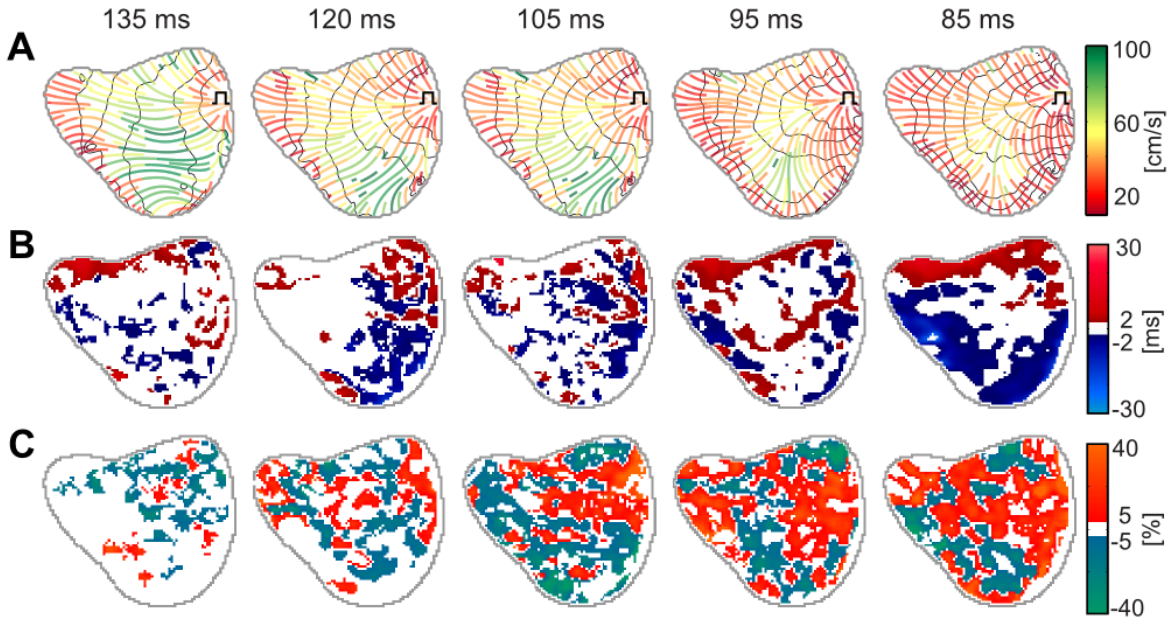

Figure 4.6 – Example of rate-dependent development of electrophysiological features obtained at different pacing cycle length after verapamil administration.
(A) Distribution of local CV through the trajectory of propagation over isochrones fragmented in steps of 5 ms (black). (B) Maps of APD alternans obtained between successive wavefronts. (C) Maps of CaT alternans obtained between successive propagations.

Regarding the trends of oscillations of ΔAPD and ΔCaT alternans during basal conditions, magnitude and standard deviation increased gradually with the activation rate until the onset of VF (i.e. blue bars). Administration of verapamil produced a dissociation between voltage and calcium alternans: ΔAPD remained at low magnitudes independently of the pacing rate, whereas ΔCaT magnitude increased following fast rates.

Notice how in all cases in the area covered by voltage or calcium alternans (Fig. 4.7B), faster activation rates were associated with higher percentage of area affected by alternans. During basal conditions VF was induced when both voltage and calcium alternans were covering almost 100% of the mapped tissue. After the administration of verapamil, VF was induced when calcium alternans were covering almost 100% of the mapped tissue, whereas voltage alternans were present on less than 70% of the tissue. These results suggest that, at least after the administration of verapamil, calcium alternans play a main role in the sequence of events that triggers VF.

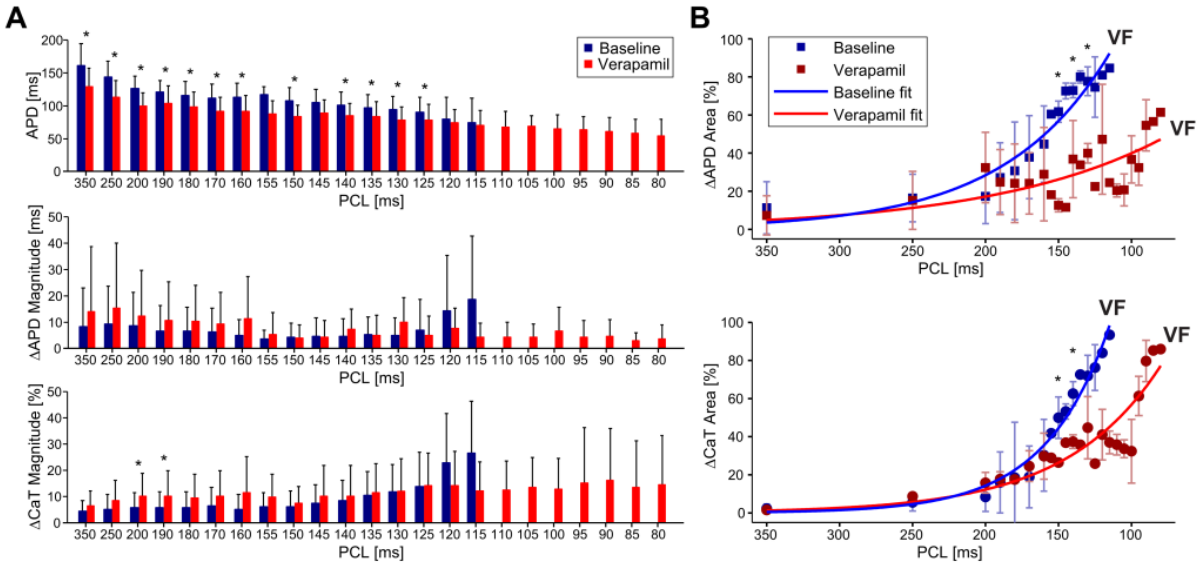

Figure 4.7 – Rate-dependent changes of APD, voltage and calcium alternans for the entire dataset both during basal conditions and after verapamil administration.

(A) Progression of APD (top panel), magnitude of APD alternans computed (middle panel) and magnitude of CaT alternans (bottom panel). (B) Percentage of area of APD (top panel) and CaT alternans (bottom panel) that covers the ventricular surface recorded during the application of the protocol of increasing rhythms during basal conditions and after verapamil administration.

Finally, in order to elucidate the role of CV on triggering VF, the variations of CV just before the initiation of VF were compared during basal conditions and after the administration of verapamil. These results indicate that the administration of verapamil produced a significant reduction of CV (Fig. 4.8A), 74.9 ± 10.4 cm/s vs 41.5 ± 9.9 cm/s, $p < 0.01$. However, if the areas with slower CV are compared; similar values of minimal CV were observed just before the initiation of VF both during basal and treated conditions, 10.9 ± 4.2 cm/s vs 8.9 ± 3.6 cm/s with not significant differences (Fig. 4.8B).

These results indicate that the combination of regions with calcium alternans and slow conduction is the mechanism behind wavefront conduction blocks that allow the initiation of reentry and VF.

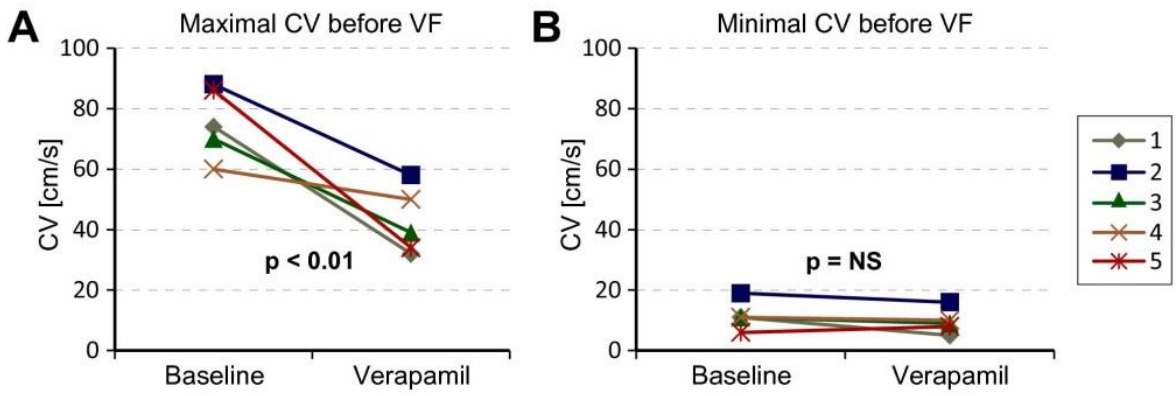

Figure 4.8 – Maximal and minimal CV measurements.

Maximal (A) and minimal (B) CV measured in the optical mapping with the fastest pacing rate previously to the induction of VF, both during basal conditions and after verapamil administration.

4.4. Discussion

4.4.1 Major findings

Major new findings of this study are as follows. First, onset of ventricular fibrillation in a high pacing rate model is linked with the conjunction of spatial calcium alternans and slow CV regions. Second, modification of L-type calcium current by means of verapamil is associated with a dissociation of the evolution between calcium and voltage spatial alternans. These results highlight the relevance of spatial electrophysiological properties such as CV and calcium SDA when a drug is applied.

4.4.2 Mechanisms of initiation of VF and Safety Pharmacology

Initiation of cardiac arrhythmias requires the combination of a trigger event and a substrate that could maintain reentry (Krummen et al. 2016). Initiation of VF has been associated with different mechanisms as for example premature ventricular complexes, caused by delayed afterdepolarizations, rapid triggers emanating from damaged areas such as Purkinje fibers or infarcted tissue (Krummen et al. 2016), or steeply sloped restitution curves that create unstable wave propagation resulting in wave break, the event that is necessary for fibrillation (Garfinkel et al. 2000). Despite these different mechanisms, one of the main risk marker commonly used as safety control in pharmaceutical trials is the QT prolongation (Nachimuthu, Assar, Schussler 2012), associated with afterdepolarizations that may produce activation blocks and reentry. From another perspective, the prolongation of action potential duration is also the target of many antiarrhythmic treatments (Pueyo et al. 2004; Torres et al. 1986), since long action potentials may reduce the probability to maintain reentry (Noujaim, Auerbach, Jalife 2007) during or after the appearance of rapid triggers.

These different scenarios perfectly illustrate the complexity of identifying a single *in-vitro* or *in-vivo* test that predicts the potential proarrhythmic effects of a novel drug. Cardiac arrhythmias, and specially VF, can be the result of many different processes. There are many factors that are rhythm and/or spatially dependent on the cardiac physiology, as the appearance of alternans or heterogeneous distributions of ionic expressions. Several experimental and computational studies have shown how initiation of cardiac arrhythmias may be the result of heterogeneous substrate regarding local CV

distribution (Choi and Salama 2000; Mironov, Jalife, Tolkacheva 2008), voltage instability driven by a steep restitution slope, development of APD (Cao et al. 1999) or CaT spatially discordant alternans (de Diego et al. 2008; Pruvot et al. 2004). Consequently, the evaluation of safety pharmacology may require mapping technologies that allow the detection of spatial heterogeneities induced by the treatment. Effects of drugs on propagation properties, such as conduction velocity or calcium associated phenomena, which remain difficult to evaluate by means of electrical mapping, may significantly influence the probability of suffering an arrhythmia. In this sense, multiparametric optical mapping has become an extended technique that allows fast and reproducible analysis of several samples, from cells to whole organs, allowing the characterization of spatiotemporal behavior (Laughner et al. 2012).

4.4.3 Role of calcium alternans and CV on VF initiation

Several studies have focused on the role of intracellular calcium on the appearance of the development of complex patterns that form a substrate prone to VF (Aistrup et al. 2006; Chudin et al. 1999; Pruvot et al. 2004), even in absence of ion current abnormalities. Specifically, overload of intracellular calcium in healthy cardiac tissue, caused by pacing rates or pressures out of the physiological limits, may form heterogeneous substrate prone to the generation of VF. The approach of these studies is usually done with isolated cells (Chudin et al. 1999), cardiac cultures (de Diego et al. 2008) or using numerical simulations (Morotti et al. 2012; Qu et al. 2000; Sato, Bers, Shiferaw 2013; Zhou et al. 2016) while similar studies of intracellular calcium distribution in whole isolated hearts are focused in other investigation lines (Gizzi et al. 2013; Harada et al. 2011; Hwang et al. 2006; Mironov, Jalife, Tolkacheva 2008; Wang et al. 2014).

In this article, we describe our approach to data processing and parameter extraction to characterize APD and CaT alternans and conduction velocity. Our results on isolated hearts are in accordance with previous studies in which the balance between increased amount of calcium instabilities and lower conduction velocity is a suitable stage prone to arrhythmic triggers (Liberos et al. 2016; Wagner, Maier, Bers 2015), suggesting that the control of this balance may work as a therapeutic target. Our results

show that during basal conditions calcium transient has a local onset similar to APD. Interestingly, this coordination was lost after the administration of verapamil, indicating that different mechanisms could be driving voltage and calcium alternans.

In order to modify the balance between sodium and calcium, we have evaluated the effects of a calcium blocker; verapamil. Different sources have shown the therapeutic effect that administration of verapamil (Chorro et al. 2000; Jin et al. 2014; Swissa et al. 2002) or other blockers (Garfinkel et al. 2000) exert on VF modulation, reducing incidence of fibrillatory episodes or reentry termination. The main conviction of its effect is the flattening of restitution curve that this class of drugs produces in the different experimental setups. However, other reports (Banville and Gray 2002) have suggested no direct link between the restitution slope with the appearance of alternans and arrhythmias. Our results indicate that after the administration of verapamil, faster activation rates are needed to produce alternans apparition, maintenance and spreading. This reduction in the alternance was correlated with a lower arrhythmogenicity. In this sequence of events, it has been shown how a reduced incidence of SDA, especially in the range of calcium alternans oscillations combined with an unchanged minimum CV, played a crucial role in reducing the generation of unidirectional blocks and reentry that promote VF. T-wave alternans together with spatial properties that could serve to estimate the heterogeneities on conduction velocities. In addition, recent studies on porcine models demonstrated that QRS duration may reflect underlying changes in CV during increased intraventricular pressure and heart failure (Quintanilla et al. 2017). However, increases of QRS duration may also be related with changes on cell size regardless of CV values (Wiegerinck et al. 2006).

4.4.4 Limitations

Our observations are restricted to healthy rabbit hearts and, therefore, extrapolating these results to other models should be done carefully. The use of pathological hearts, with for example chronic infarct hearts, could increase the efficacy of the technology evaluation the risk of novel drugs. CV measurements from optical mapping may be affected by curving of the heart or perpendicular propagation of the wavefront towards the field of view, leading to overestimated CVs. However, presented measurements have been compared between exactly same points of view; consequently CV reductions

observed during fast pacing rates or after the administration of the drug are independent of the mentioned limitation.

In this study, we choose to evaluate verapamil due to its controversial electrophysiological properties and its potential effects over alternans (Chorro et al. 2000; Liberos et al. 2016; Samie et al. 2000). Nevertheless, optical mapping technology could be used to evaluate the effect of both proarrhythmic and antiarrhytmic drugs. In addition, it is important to realize that existing optical mapping techniques require electromechanical dissociation which may influence calcium homeostasis. Despite of that, this is the only technology that is available nowadays for quantifying calcium dynamics. T wave alternans has been proposed as a clinical biomarker of arrhythmia risk (Ikeda et al. 2006) and may be a major factor in the decision to prescribe the use of an implantable defibrillator or antiarrhythmic therapy. Our results indicate that alternans are linked with the induction of VF when they are associated with slow conduction velocities. Consequently, our study emphasizes the need to analyze.

4.4.5 Conclusions

In the present study, we have shown that the combination of spatially discordant cardiac alternans and heterogeneous CVs is associated with reentry and VF initiation. This sequence of events can be modified by the administration of a drug and therefore change the onset of VF. In addition, the analysis of APD duration may not be sufficient to predict the safety or pro-arrhythmogenicity of a drug.

.

Chapter 5

Arrhythmic mechanisms of quiescent cardiac substrates

5.1. Introduction

Brugada syndrome (BrS) is characterized by distinctive ST-segment elevation in the right precordial leads of the electrocardiogram (ECG), and propensity for sudden cardiac death (Antzelevitch 2005; Brugada and Brugada 1992). According to the 2013 consensus statement on cardiac arrhythmia syndromes and the 2016 J-Wave syndromes expert consensus conference report, BrS is diagnosed in patients with spontaneous ST-segment elevation (≥2 mm) with type-1 morphology in ≥1 precordial leads, particularly V1 and V2, positioned on the 2nd and 3rd or 4th intercostal spaces (Antzelevitch et al. 2017; Priori et al. 2013). Although, BrS has been considered as a primary electric cardiac disease caused by mutations in genes coding sodium, calcium and potassium channels in ~30% of patients (Antzelevitch et al. 2017; Bezzina et al. 2013; Priori et al. 2013). Other studies have demonstrated that minor structural abnormalities are also associated with the syndrome (Coronel et al. 2005; Corrado et al. 2016; Frustaci et al. 2005).

Moreover, some environmental factors can induce ECG morphologies similar or identical to type-1 BrS in the absence of genetic mutations or ion channel dysfunction (Frustaci et al. 2005; Probst et al. 2010). The acquired form of Brugada-like ECG pattern, also termed Brugada ECG phenocopy (BrP), occurs in the presence of an identifiable underlying condition and typically disappears after its resolution (Antzelevitch et al. 2017; Baranchuk et al. 2012; Littmann et al. 2007; Priori et al.

2013; Weiss, Qu, Shivkumar 2017). Multiple metabolic conditions can lead to BrP ECG; the majority of cases are associated with serum K+ abnormalities, hyperkalemia being the most frequent single cause (Baranchuk et al. 2012). Although classical hyperkalemia produces several well-described ECG alterations, only a minority of patients develop BrP (Baranchuk et al. 2012; Weiss, Qu, Shivkumar 2017). Nevertheless, the clinical characteristics and prognostic impact on patients developing BrP are poorly known.

The main mechanism responsible for BrS phenotype relate to abnormal patterns of repolarization and/or impulse activation at the right ventricular outflow tract (RVOT) (Hoogendijk et al. 2010a; Nademanee, Hocini, Haïssaguerre 2017; Wilde et al. 2010; Zhang et al. 2015). However, whether BrP represents transient alterations in myocardial depolarization, repolarization or any other mechanism is yet to be elucidated. Moreover, the transient nature of BrP casts doubt about its genetic origin or relation to structural abnormalities, or both.

The objectives of the study were several fold, including to: 1) conduct computer simulations in a 3D model of ventricular propagation under conditions of varying hyperkalemia to analyze the implication of mutations and/or structural abnormalities in relation to the Brugada sign (Hoogendijk et al. 2010b); 2) study the mechanisms underlying hyperkalemic BrP; 3) evaluate the pro-arrhythmic risk of BrP in the presence of hyperkalemia; and 4) assess if the conduction velocity is an indicator of the arrhythmic substrate.

5.2. Methods

5.2.1 Computer Simulations

A multiscale computer model was constructed to determine conditions for the BrP ECG in patients with hyperkalemia. The model was based on several parameters, including electrophysiological dynamics, transmural differences in cell type, fiber orientation and fibrosis at varying extracellular potassium concentrations ($[K^+]_o$) ranging between 5.4 and 10.5 mM. A human wedge model of the anterior ventricular wall, including both ventricles and the RVOT, was created using a reference geometry (normal young male, NYM), available for the ECGSIM software (van Oosterom and

Oostendorp 2004). The mesh contained 281,191 nodes and 1,460,832 elements with a mean edge length of 290.8 ± 296.6 μm (Figure 5.1A).

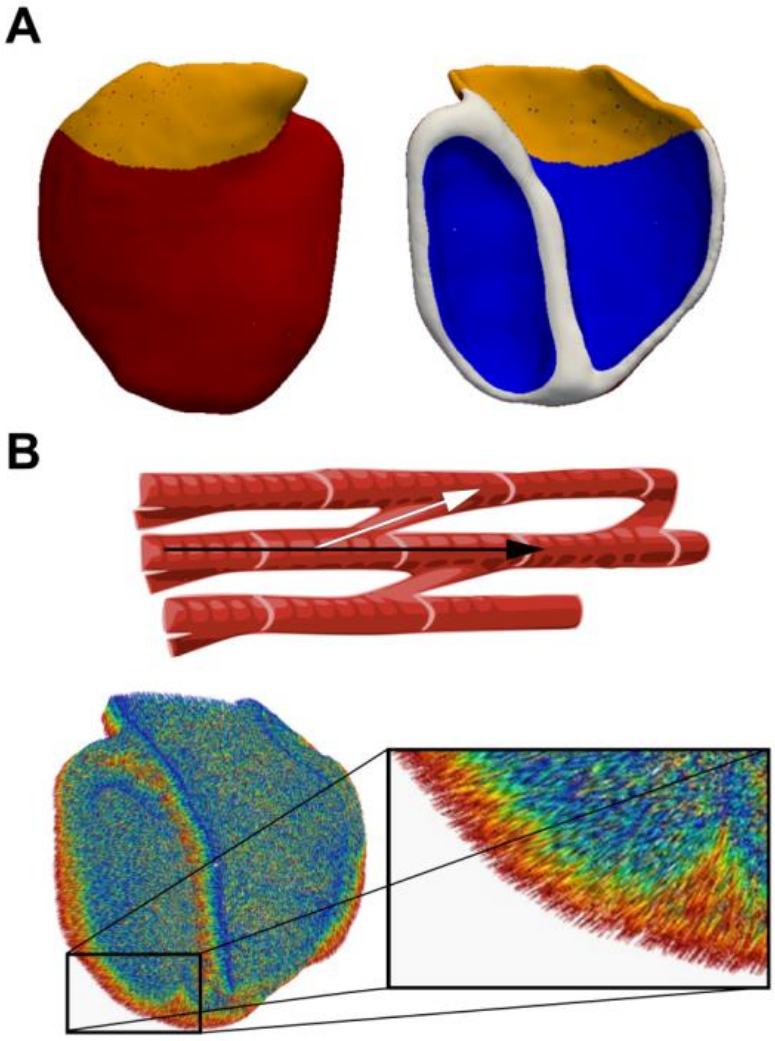

Figure 5.1 – Tetrahedral finite-element wedge of ventricular mesh.

(A) Visualization of the wedge ventricular finite-element mesh from a standard anterior view (left) along with the frontal (right) representing the selected epicardial surface (red), endocardial surface (blue) and RVOT region (orange). (B) Top, Conditions for anisotropy at the cellular level; Bottom, fiber direction in the 3D model.

Human ventricular cell dynamics and action potential morphologies of cell types were simulated using the O'Hara-Rudy model (O'Hara et al. 2011), with modifications in the sodium current suggested by Dutta et al. (Dutta et al. 2017), which enabled realistic simulations under hyperkalemic conditions. Anisotropic conduction due to fiber orientation changes was incorporated into the model using an anisotropy ratio of 10:1, $D_{\parallel}:D_{\perp}$, where $D_{\parallel}$ and $D_{\perp}$ are the longitudinal and transverse diffusion

coefficients respectively. Therefore, propagation in any direction of the 3D model depended on the fiber direction. The RVOT diffusion coefficient was 25% of either ventricle, keeping the same anisotropy ratio (Figure 6.1B). Ventricular activation sequences were based on Cardone-Noott et al. (Cardone-Noott et al. 2016), being initiated in three areas in our model (Figure 6.2A).

Simulations were performed under four different conditions: 1) healthy RVOT; 2) fibrotic RVOT; 3) RVOT with a gradient of transient outward potassium current (I_{to}); and 4) fibrotic RVOT with an epi-to-endocardium Ito gradient. Various $[K^+]_o$ concentrations (5.4, 7.5, 10.0 and 10.5 mM) were chosen considering that the level of serum K^+ registered in patients could be lower than in the extracellular space (Pelleg et al. 1989). Different $[K^+]_o$ were tested in basal conditions and RVOT with 65% of fibrotic tissue. Fibrotic tissue was modeled by randomly disconnecting a specific percentage of available nodes in the RVOT. The enhanced Ito conductance gradient (G_{Ito}) was established by increasing the maximal conductance of the current on the epicardium of the RVOT, from its basal level (0.08 mS/µF) to 0.30, 0.70 and 1.50 mS/µF; these values were consistent with experimentally derived data related to BrS (Giudicessi et al. 2011). Different cases were tested, combining the amount of fibrosis (55, 65 and 75%), $[K^+]_o$ concentrations (5.4 and 10.5 mM) and increasing G_{Ito} from baseline to the maximal conductance 1.50 mS/µF. Monodomain equations were solved using the Forward-Euler algorithm with a fixed time step of 0.01 ms on a graphic processors unit (GPU Tesla K20 5GRAM DDR5) (García-Molla et al. 2014). Three virtual electrodes were positioned at standard electrode locations for the calculation of pseudo-ECGs V1, V2 and V3 (Figure 5.2B).

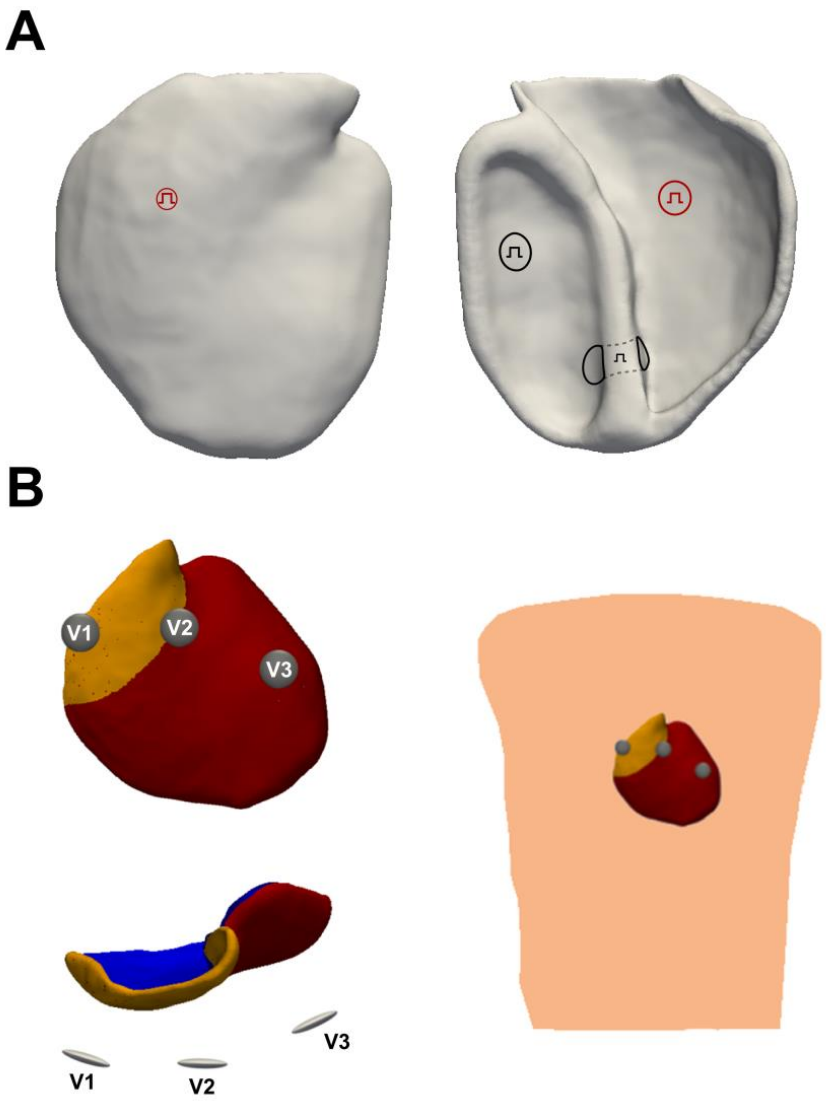

Figure 5.2 – Ventricular activation sequence and derivation lead positions.

(A) Simulated ventricular activation sequence was initiated in three areas. Stimulus locations to generate the ventricular activation sequence. Activation stared at the location marked in red followed 5 ms later by simultaneous activation of the two black regions. (B) Representation of the places where V1, V2 and V3 derivations were calculated from the anterior view (upper-left), base view (lower-left) and along the representation of the torso (right).

5.2.2 Conduction Velocity Estimation

Conduction velocity (CV) was measured in each node of the computer model using the method presented in the Chapter 3. Calculation of CV was made by means of the generated activation times. To construct the activation map, the time instant of depolarization of each simulated action potential was storage. Example of the estimated CV is shown in Figure 5.3.

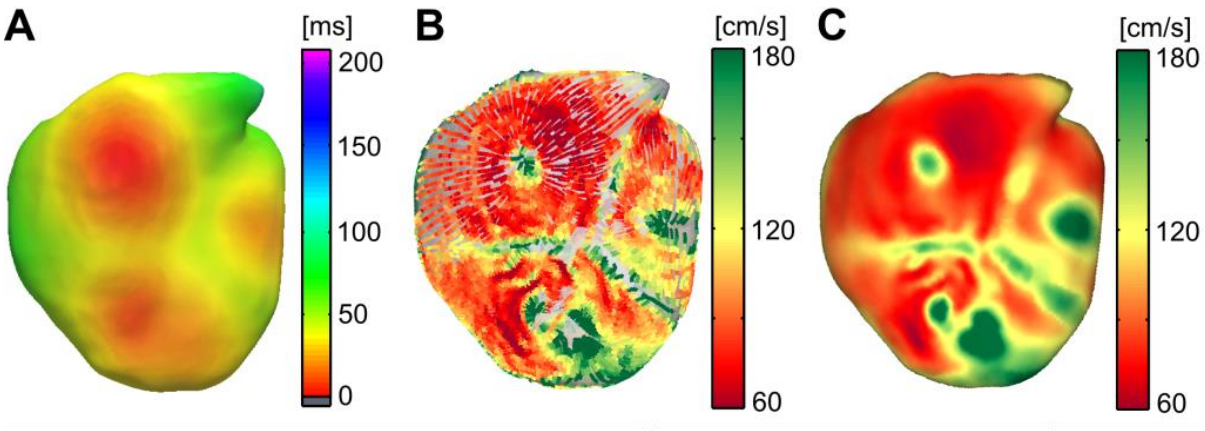

Figure 5.3 – CV estimation using activation time of the models.
(A) Activation sequence of a ventricular model. (B) Pathway representation of CV estimation with the proposed methodology. (C) Projection of nominal value of CV estimated over the ventricular mesh.

5.3. Results

5.3.1 Hyperkalemia, fibrosis and the mechanism of BrP

To differentiate between the mechanism underlying BrP versus non-Brugada ECGs during hyperkalemia, we simulated the effects of increasing $[K^+]_o$ in a human wedge model of the anterior ventricular walls, including the RVOT. Elevating the $[K^+]_o$ reduced the resting membrane potential throughout from -87.9 ± 0.1 mV at $[K^+]_o$ = 5.4 mM to -69.93 ± 0.08 mV at $[K^+]_o$ = 10.5 mM, regardless of whether or not the RVOT was fibrotic. As expected, the depolarized resting potential reduced the availability of the sodium channels and slowed the conduction velocity. Figure 5.4 shows activation

sequences and V1-V3 recordings for 4 different $[K^+]_o$ (5.4, 7.5, 10.0 and 10.5 mM) in the presence and the absence of fibrosis at the RVOT. Conduction at the RVOT was significantly altered at 65% fibrosis, with changes in the activation sequence that promoted the appearance of late and fractionated potentials on V1 to V3. There was a progressive slowing of conduction with increasing $[K^+]_o$. A similar progression was also apparent on the V1, V2 and V3 recordings for each $[K^+]_o$ and normal/fibrotic state. Notable changes occurred on leads V1 and V2, where there was delayed activation at the RVOT, which prolonged the QRS interval proportionately. Moreover, the ST-segment elevated and gradually fussed with the T wave as the $[K^+]_o$ increased. In the absence of fibrosis, at $[K^+]_o$ = 10.0 mM, the model reproduced the characteristic features of hyperkalemia in patients with healthy RVOT. In contrast, in the fibrotic case, conduction slowing or block promoted ST-segment elevation on V1 and V2 consistent with the classical BrS descriptors. In Figure 5.5, the corresponding action potential duration (APD) maps show a progressive global decrease in the APD as $[K^+]_o$ is increased. As illustrated also by the action potential recordings at specific locations, fibrosis intensified both the APD shortening and the activation delay at the RVOT and its immediate vicinity.

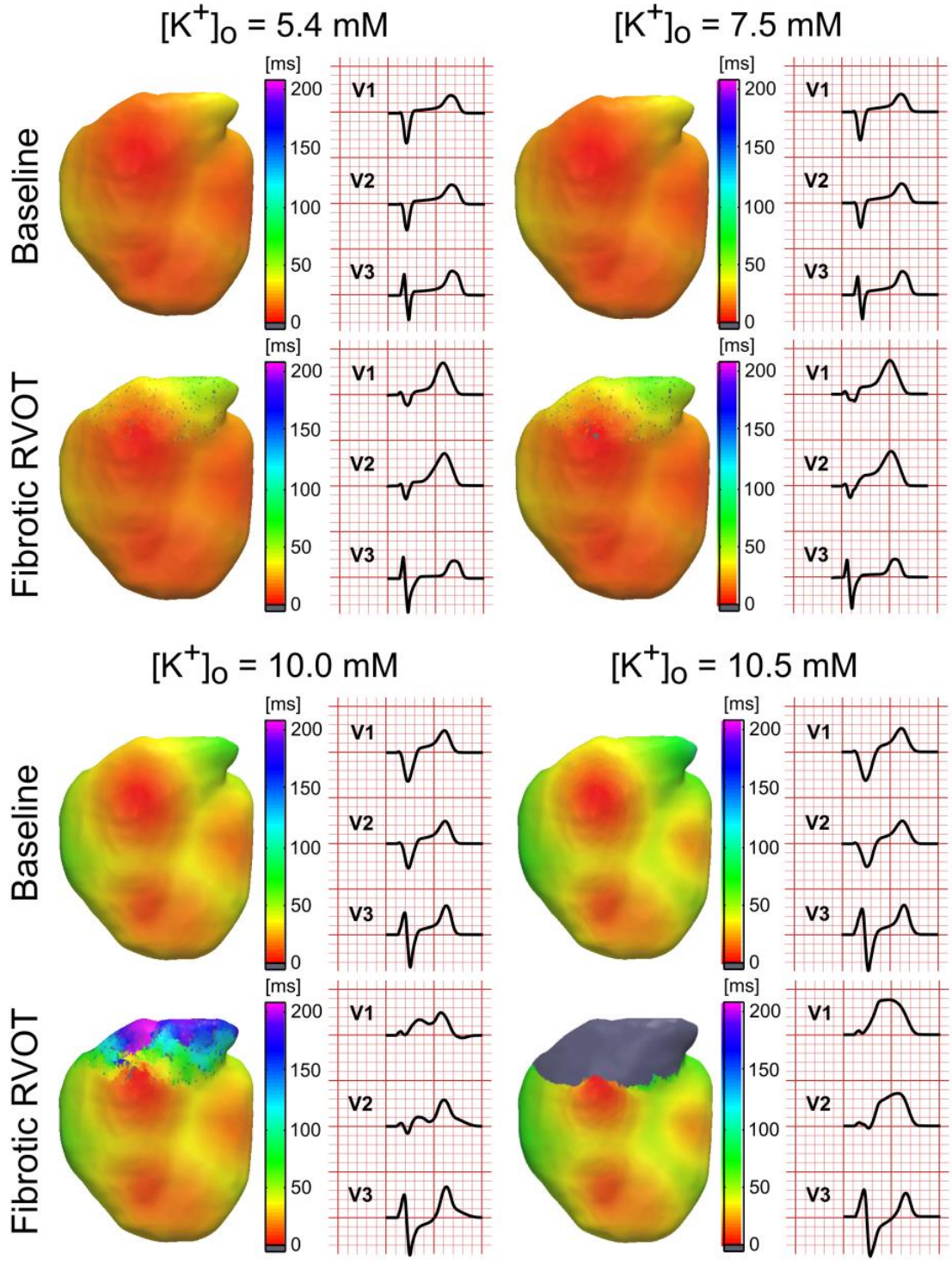

Figure 5.4 – Activation time of computer simulations testing the role of fibrosis of the RVOT at different levels of hyperkalemia.

Activation maps of the anterior wall with healthy and fibrotic RVOT, under basal conditions with $[K^+]_o$ = 5.4 mM and hyperkalemic conditions with $[K^+]_o$ = 7.5 mM, $[K^+]_o$ = 10.0 mM, and $[K^+]_o$ = 10.5 mM. Pseudo-ECGs of V1, V2 and V3 leads are shown in each case.

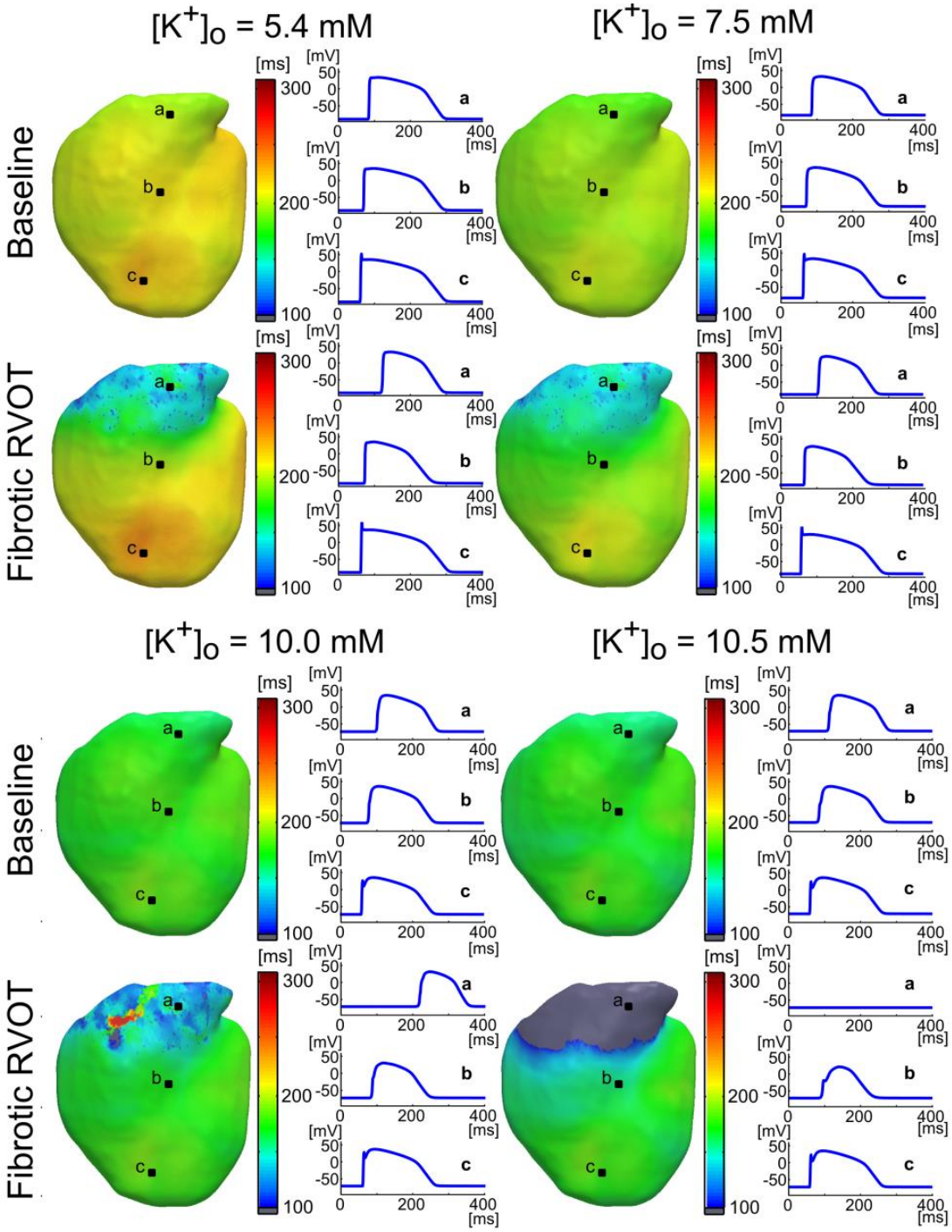

Figure 5.5 – APD of computer simulations testing the role of fibrosis of the RVOT at different levels of hyperkalemia.

APD maps of the anterior wall with healthy and fibrotic RVOT, under basal conditions with $[K^+]_o$ = 5.4 mM and hyperkalemic conditions with $[K^+]_o$ = 7.5 mM, $[K^+]_o$ = 10.0 mM, and $[K^+]_o$ = 10.5 mM. Pseudo-ECGs of V1, V2 and V3 leads are shown in each case, and corresponding APD of sites a, b and c are shown in each case.

5.3.2 Role of Ito

Previous evidence has implicated the epicardial-to-endocardial transient outward current (I_{to}) gradient within the right ventricle in the pathogenesis and phenotypic expression of Brugada Syndrome. We therefore conducted additional simulations to test the consequences of combining hyperkalemia with increased epicardial I_{to} gradient at the RVOT in the presence and the absence of fibrosis. The gradient was established by increasing the baseline value of the epicardial band to 0.30, 0.70 and 1.50 mS/µF, while leaving the endocardium at the basal level (0.08 mS/µF). In Figure 5.6, under basal $[K^+]_o$ conditions, we had to increase the maximal Ito conductance up to 1.50 mS/µF, to enable BrP, a value that is characteristic of BrS modeling.

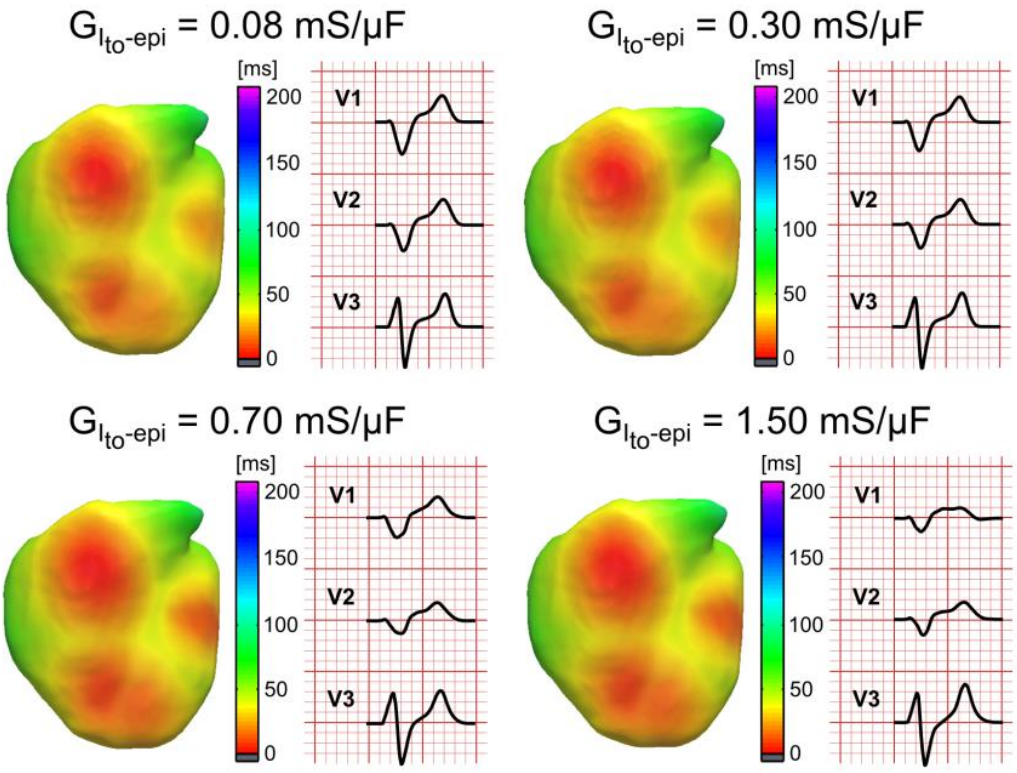

Figure 5.6 – Activation time of computer simulations testing the increment of I_{to} conductance.

Activation maps of the anterior RVOT wall with increasing I_{to} maximal conductance in the RVOT epicardium, from its basal level to a characteristic value in BrS modeling (from 0.08 to 1.50 mS/µF, showing 0.30 and 0.70 mS/µF), under severe hyperkalemia ($[K^+]_o$ = 10.5 mM). Pseudo-ECGs of V1, V2 and V3 leads are shown in each case.

Increasing I_{to} produced a progressively exaggerated action potential notch (arrow) at the RVOT while the rest of the tissue was undergoing initial depolarization during the plateau (Figure 5.7). On the electrograms, these events coincided with ST-segment elevation.

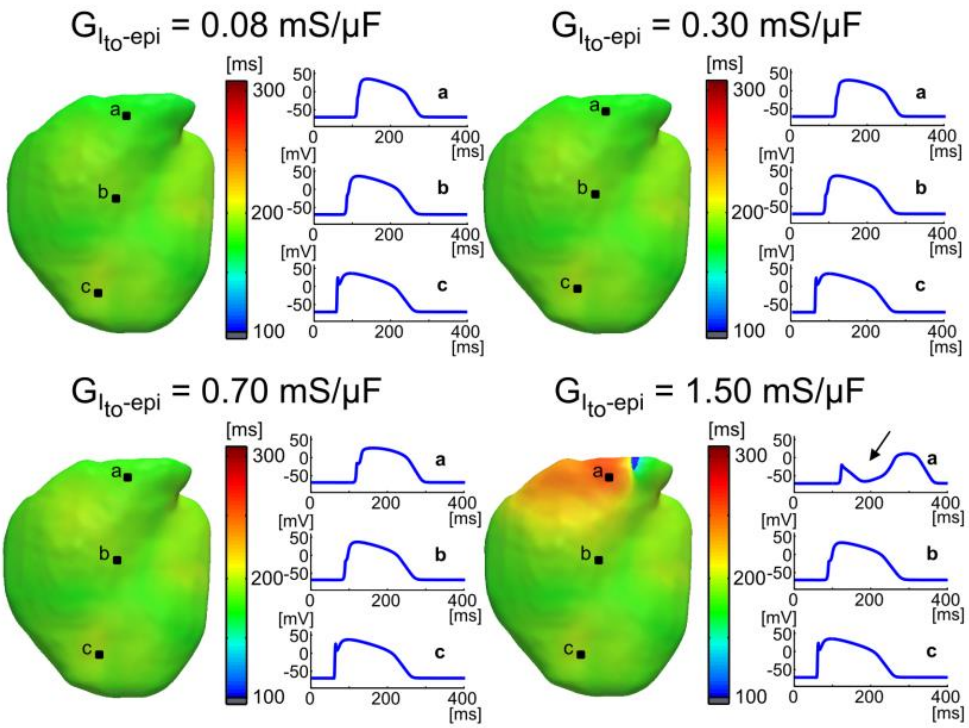

Figure 5.7 – APD of computer simulations testing the role of incremental Ito conductance.

APD maps of the anterior with increasing Ito maximal conductance in the RVOT epicardium, from its basal level to a characteristic value in BrS modeling (from 0.08 to 1.50 mS/µF, showing 0.30 and 0.70 mS/µF), under severe hyperkalemia ([K+]o = 10.5 mM) and corresponding APD of sites a, b and c are shown in each case. Notch appears in the RVOT with Ito = 1.50 mS/µF.

As illustrated in Figure 5.8, the combined effects of fibrosis, elevated $[K^+]_o$ induced membrane depolarization leading to reduced excitability, and increased Ito density greatly facilitated the appearance of BrP on leads V1-V2. In Figure 5.8A, a BrP pattern was already evident on V1 and V2 at 55% fibrosis even when the epicardial Ito was at baseline (0.08 mS/µF). The effect was even greater when fibrosis at the RVOT was increased to 75%. Here ST-segment elevation occurred at 10 mM of $[K^+]_o$ because of extreme conduction delay at the RVOT (Figure 5.8B).

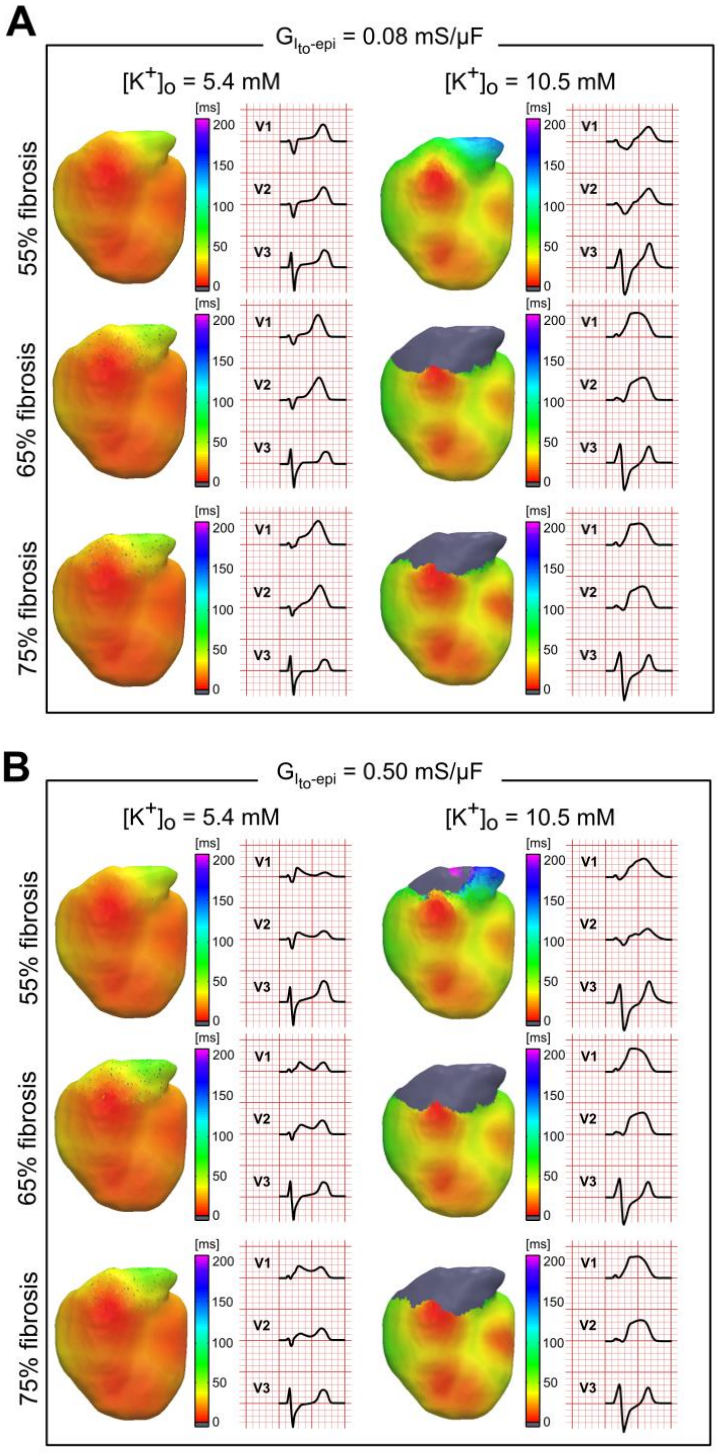

Figure 5.8 – Computer simulations testing the role of incremental fibrosis, I_{to} conductance and $[K^+]_o$ conditions.

(A) Activation maps of the anterior RVOT wall with different degrees of fibrosis (55, 65 and 75%), at baseline $[K^+]_o$ concentrations (5.4 and 10.5 mM, respectively), with a maximal conductance of Ito = 0.08 mS/µF. Pseudo-ECGs of V1, V2 and V3 leads are shown in each case. (B) Activation maps of the anterior RVOT wall with different degrees of fibrosis (55, 65 and 75%), at baseline and severe $[K^+]_o$ concentrations (5.4

and 10.5 mM, respectively), with a maximal conductance to I_{to} = 0.50 mS/µF. Pseudo-ECGs of V1, V2 and V3 leads are shown in each case.

In additional simulations, we assessed the effects of fibrosis and Ito current gradient on the entire ventricular wall. The effects were similar to those observed when such changes were only applied to the RVOT. The relative increase in Ito over the entire epicardial surface with respect to the endocardium simulated characteristics of the Brugada pattern (Figure 5.9).

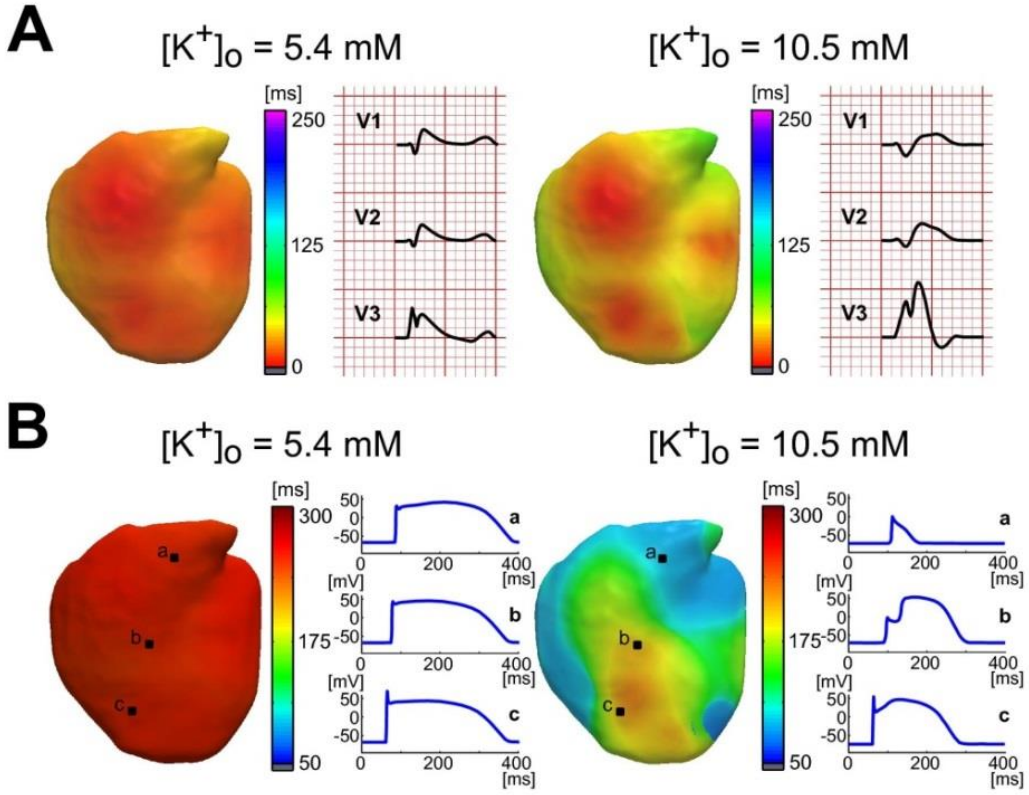

Figure 5.9 – Computer simulations testing the role of gradient of Ito conductance over the entire epicardial surface at different levels of [K+].

(A) Activation maps with Ito maximal conductance in the whole epicardium to a characteristic value in BrS modeling (1.50 mS/µF), under basal conditions ($[K^+]_o$ = 5.4 mM) and hyperkalemic conditions ($[K^+]_o$ = 10.5 mM). Pseudo-ECGs of V1, V2 and V3 leads are shown in each case. (B) APD maps and corresponding APD of sites a, b and c are shown in each case.

At baseline, the Ito gradient caused an increase in the duration of the epicardial action potential by increasing the transmembrane potassium outflow during the whole

plateau phase. This slightly elevated the ST segment and decreased the T wave amplitude, even depressing the T wave on V3. However, the $[K^+]_o$ increase also depolarized the membrane potential and reduced the availability of the sodium channels. Consequently, conduction velocity was reduced and the action potential duration was abbreviated, with the appearance of regions of activation failure.

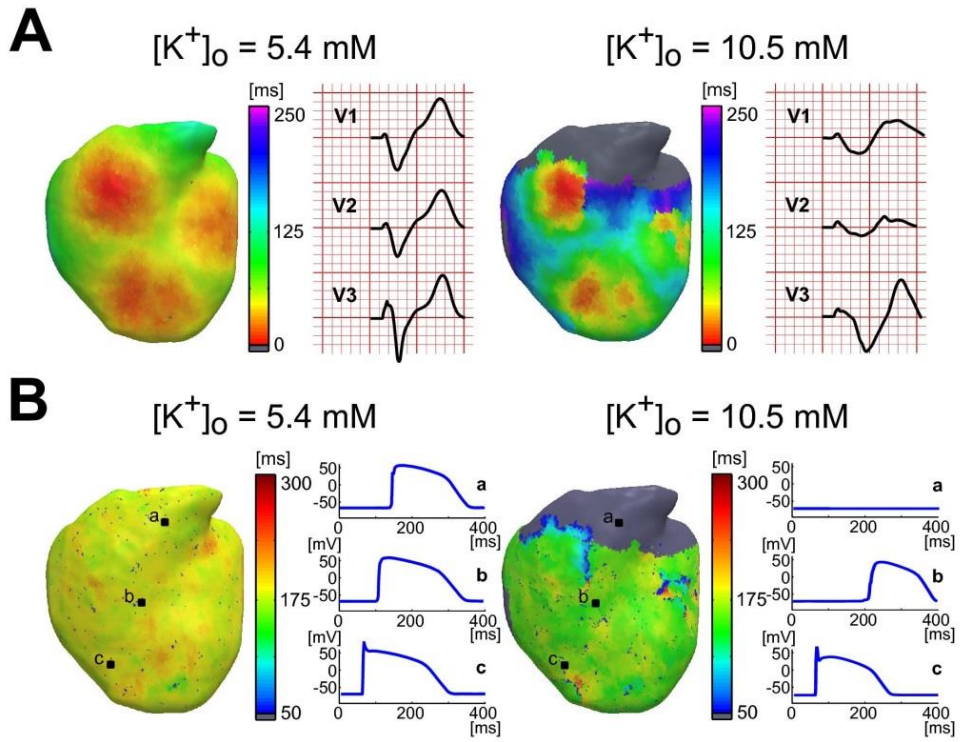

Figure 5.10 – Computer simulations testing the role of fibrosis over the entire epicardial surface at different levels of $[K^+]_o$.

(A) Activation maps with fibrosis in the whole (65%), under basal conditions ($[K^+]_o$ = 5.4 mM) and hyperkalemic conditions ($[K^+]_o$ = 10.5 mM). Pseudo-ECGs of V1, V2 and V3 leads are shown in each case. (B) APD maps and corresponding APD of sites a, b and c are shown in each case.

Fibrosis throughout the ventricular surface slowed activation and wavefront propagation (Figure 5.10), prolonging the QRS and delaying T wave activation more than when fibrosis was present in the RVOT. When the $[K^+]_o$ was raised to a pathological threshold, conduction slowed further with propagation failure in areas with less excitable cardiac tissue, including the RVOT and its surroundings. ST segment elevation did not occur under these conditions due to the conduction slowing generated.

5.3.3 Pro-arrhythmic Risk of BrP pattern

The pro-arrhythmicity of the proposed model was tested. In Figure 5.11, we used a fibrotic RVOT with hyperkalemic conditions at $[K^+]_o$ = 10.0 mM. A burst stimulus train with an extra stimulus at 400 ms, increased electrogram fractionation and caused unidirectional block that allowed stable reentry formation at the RVOT.

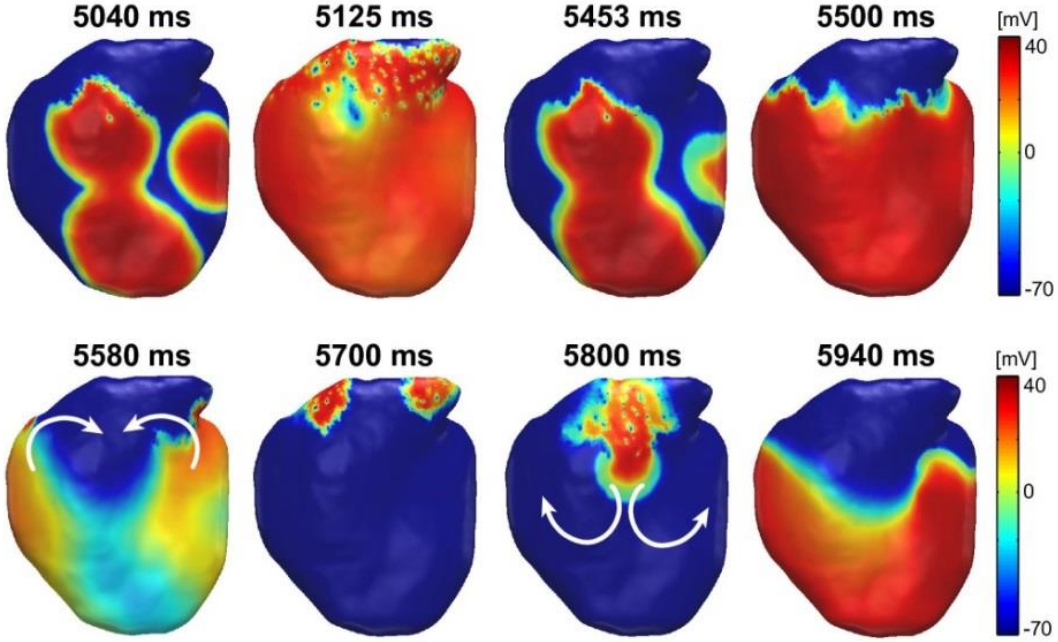

Figure 5.11 – Monomorphic ventricular tachycardia.

Monomorphic ventricular tachycardia induction during burst stimulation train followed by an extrastimuli at 400 ms allowed a stable reentry formation at the RVOT fibrotic site in a model with hyperkalemic conditions at $[K^+]_o$ = 10.0 mM.

Next, the CV was estimated in the main proposed stages. In Figure 5.12, we obtain the outcome in a non-hyperkalemic and hyperkalemic situation, with a healthy tissue, with fibrotic RVOT and with a genetic alteration of I_{to} in the RVOT.

When hyperkalemia is not present at 5.4 mM, the CV at the healthy RVOT was 143.89 ± 23.52 cm/s, 60.81 ± 12.34 cm/s when fibrosis was included in the RVOT and 140.23 ± 17.94 cm/s with Ito modification in the RVOT. In hyperkalemic conditions ($[K^+]_o$ = 10.0 mM), CV was 87.53 ± 11.04 cm/s at baseline, 28.66 ± 7.32 cm/s with the fibrotic RVOT and 55.61 ± 15.33 cm/s with Ito alteration.

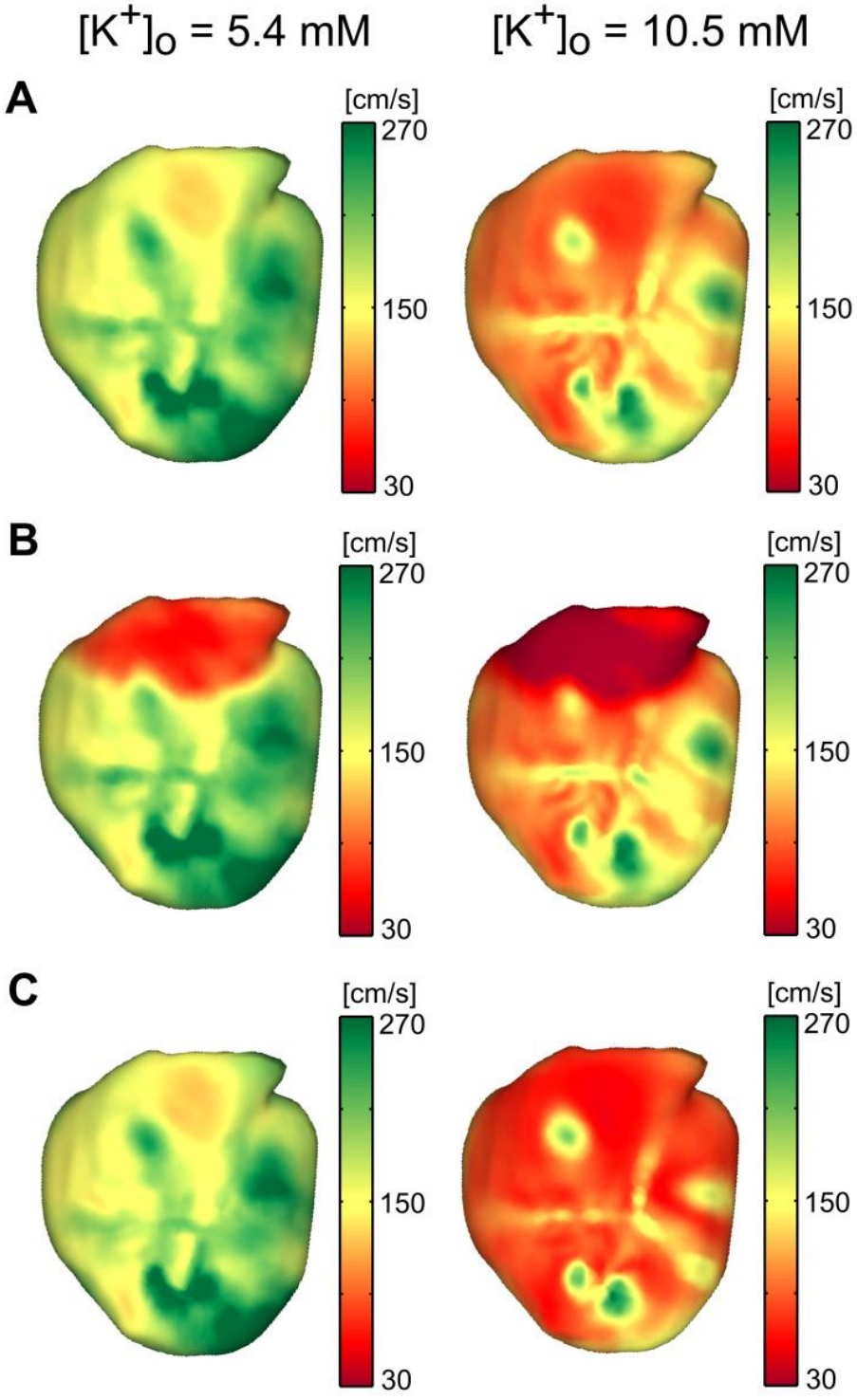

Figure 5.12 – CV estimation of computer simulations with hyperkalemia.

(A) CV estimation in a healthy tissue model with $[K^+]_o$ = 5.4 mM and $[K^+]_o$ = 10.0 mM. (B) CV estimation in a fibrotic RVOT model with $[K^+]_o$ = 5.4 mM and $[K^+]_o$ = 10.0 mM. (C) CV estimation in a genetic alteration model of I_{to} (1.50 mS/µF) with $[K^+]_o$ = 5.4 mM and $[K^+]_o$ = 10.0 mM .

5.4. Discussion

5.4.1 Major findings

The main findings of this study are as follows:

1. In cases of severe hyperkalemia, the presence of a BrS phenotype in models is associated with a high prevalence of malignant arrhythmias and all-cause mortality.

2. As shown by computer simulations, the ECG manifestations of systemic hyperkalemia are a consequence of the depolarized resting membrane potential and reduced sodium channel availability for action potential activation, which results in delayed and heterogeneous conduction, or block, particularly in the presence of fibrosis at the RVOT.

3. CV estimation can be useful to discriminate between the possible assumptions related the Brugada sign apparition.

5.4.2 Mechanism of pro-arrhythmic risk of BrP pattern

To our knowledge, the relationship between hyperkalemia and the BrS ECG manifestations had not yet been systematically investigated. Together, the clinical results and computer simulations presented above provide mechanistic insight into the manifestation of electrolytic dysregulations causing BrP phenotype. Even in the absence of genetic disease (e.g. inheritable SCN5A mutations), delays in ventricular activation and propagation failure at the RVOT, magnified by the presence of hyperkalemia and, possibly, low acid base state, promote the required electrophysiological changes, including APD shortening, membrane depolarization and reduced sodium channel availability, which enable the manifestation of BrP ECG, an effect that is magnified by RVOT fibrosis. The introduction of fibrotic tissue reduced the excitability of the RVOT and slowed CV leading to a ST-segment elevation on V1 and V2 leads, creating the substrate for the inducibility of malignant arrhythmias. In agreement with previous clinical reports, computer simulations showed that programmed stimulation caused electrogram fractionation and unidirectional block to initiate stable reentry formation without the need of an extrasytole (Coronel et al. 2005). Unexcitability due to the high concentration of potassium and its propensity to the generation of arrhythmias agrees with recent reports (Weiss, Qu, Shivkumar 2017).

These results are supported by simulations by other groups showing activation delay and right ventricular excitation failure due to current-load mismatch secondary to decrease in calcium current or increase in Ito can cause BrS (Hoogendijk et al. 2010a; Hoogendijk et al. 2010b). Similar mechanisms could be responsible for other types of BrP, with low availability of sodium channels as it occurs during hypothermia or acidosis in ischemic regions.

The relative increase in Ito density at the RVOT reduced the need for slow conduction caused by hyperkalemia and resulted in spatial gradients of membrane voltage giving rise to the typical ST-segment elevation found in BrP. In agreement with the BrS, the strong sex-related predominance found in the BrP indirectly supports the prominence of the transient outward current-mediated action potential notch in the right ventricular epicardium of males (Di Diego et al. 2002). Moreover, the combination of abnormal repolarization and abnormal conduction not only explains the phenotypic manifestation of the BrP but also its clinical arrhythmic outcomes in the form of sustained ventricular reentrant patterns. On one hand, the presence of steep repolarization gradients causes asymmetry in excitability that gives rise to unidirectional block. On the other, slow conduction shortens the wavelength of the reentrant AP facilitating reentrant stabilization (Figure 5.11). Therefore, severe hyperkalemia leading to inactivation of the sodium channel in conjunction with the presence of subtle structural abnormalities of the right ventricular outflow tract were responsible for the BrP manifestation and the reentrant arrhythmias occurrence in this setting.

5.4.3 Limitations

Although the computer simulations support the theory that RVOT has a major role producing Brugada patterns, further clinical data (histological and image data) and cellular studies are necessary to accurately define the substrate of this clinical entity in this environment (Guillem et al. 2016a; Nademanee, Hocini, Haïssaguerre 2017). For example, imaging (e.g, MRI) data in patients presenting with a BrP ECG could have shown enhanced fibrosis in the RVOT, as predicted by the modeling results. However, MRI was nearly impossible in our study due to the fact that many of the patients were

critically ill and had a very poor outcome, which substantially limited the number of patients available to study.

5.4.4 Conclusions

This report adds to our understanding of the electrocardiographic features of hyperkalemic BrP patients. In patients with severe hyperkalemia due to critical medical conditions, a BrP ECG is associated with a high prevalence of malignant arrhythmias and high all-cause mortality. The BrP ECG manifestations in patients with hyperkalemia are due to depolarized resting membrane potential and reduced availability of inward sodium channels. While Ito elevation contributes, it is not essential to generate the hyperkalemic BrP phenotype.

Chapter 6

Conclusions and Future Work

In this chapter a global conclusion of the results given in this dissertation is presented. First, the main conclusions of this thesis are listed by assessing the resolution of the objectives. The chapter is closed with a guideline for future work, highlighting aspects of this work that can be improved and the range of future lines of research.

6.1. Conclusions

A novel signal processing tools to characterize cardiac activity, and specifically conduction velocity, has been developed and validated helping to increase our knowledge regarding arrhythmias and to improve treatments efficacy. This novel technology has been validated by using mathematical model, exvivo isolated heart experiments and clinical data. The development of those research models has been also an important achievement of the present thesis.

The conclusions of each specific objective are:

1. ***To develop a robust methodology to measure conduction velocity both during regular and during fibrillatory activity from different invasive and non-invasive techniques.***

A new methodology was designed to measure conduction velocity in fibrillatory functional and re-entrant patterns. The proposed methodology was validated with the

use of simple and realistic cardiac 3D models. The described technique was designed under an structure that allows its implementation to measure conduction velocity on epicardial mapping techniques but also from non-invasive ECGI mapping.

2. ***To validate the proposed conduction velocity measurement during atrial fibrillation patterns and to study its potential use as clinical predictor of ablation regions causing of the arrhythmia from ECGI.***

The developed methodology was applied to in atrial fibrillation, which is the arrhythmia with most prevalence worldwide and with current treatments of limited efficacy. The proposed method allowed the estimation of CVs during simple and fibrillatory patterns on realistic atrial geometries. The analysis from ECGI has been validated with intracardiac recordings, in addition the proof of concept results demonstrate that this novel technology could serve to stratify AF patients.

3. ***To apply the proposed conduction velocity measurement during under experimental set-ups that allow the clarification of the mechanisms of alternants on the initiation of ventricular fibrillation***

Thanks to the application of the developed technology, we have shown that the combination of spatially discordant cardiac alternans and heterogeneous conduction velocities is associated with reentry and ventricular fibrillation initiation. This sequence of events can be modified by the administration of a drug and therefore change the onset of ventricular fibrillation. In addition, our study demonstrated that the classical analysis of action potential duration may not be sufficient to predict the safety or pro-arrhythmogenicity of a drug.

4. ***To clarify the arrhythmic mechanisms of the manifestation of Brugada pattern under hyperkalemic environment by employing the proposed methodology.***

Thanks to the application of the proposed technology and the developed mathematical models, the present thesis adds to our understanding of the electrocardiographic features of hyperkalemic Brugada patients. In patients with severe hyperkalemia due to critical medical conditions, a Brugada ECG is associated with a high prevalence of malignant arrhythmias and high all-cause mortality. The Brugada

ECG manifestations in patients with hyperkalemia are due to depolarized resting membrane potential and reduced availability of inward sodium channels which reduces conduction velocity. While Ito elevation contributes, it is not essential to generate the hyperkalemic Brugada phenotype. CV measurements could serve to discriminate between the possible causes related the Brugada manifestation.

6.2. Guidelines for future works

Nowadays, cardiac arrhythmia patients' treatment selection {which can follow pharmacological and/or surgical approaches} is mostly based on population-derived statistics {considering risk factors such as age, body habitus, etc.} and not based in the specific cardiovascular manifestation of the disease in each patient. Therefore, it is not surprising that both pharmacological and surgical treatments have suboptimal outcomes, and each patient can go through a plethora of therapies until one of them shows positive results.

The technology developed in the present thesis has demonstrated that the characterization of conduction velocity can be measured from non-invasive techniques such as ECGI and help to understand the behavior of different cardiac arrhythmias. This technology can help to become possible to deliver a precision medicine strategy based on the personalized characterization of each arrhythmia manifestation. Personalization of cardiovascular therapies in patients based on the individual characterization of the specific disease is therefore not only an option, but a need for health providers, motivated by the lack of success of the current therapy track

Our results and technology, together with the efforts of many groups around the world will enclose the scenario which successful personalization therapies could be offered based on the individual characterization of the cardiac disease for each patient. To make that a reality several actions are required:

- To validate the presented technology and its clinical applicability under a large clinical trial. This is now under development inside the project STRATIFY-AF funded by the Instituto de Salud Carlos III.
- To ensure that the developed technology is introduced in a medical device that could be distributed to all hospitals and help to increase the efficacy of

antiarrhythmic treatments. Our team is in the process of transfer of these technologies through the recently constituted Start-up Corify Care S.L.

In addition to those clinical applications of the developed technology, technological advances are required to increase the quality of research models and to continue improving the efficacy of characterization techniques. Those efforts are only being possible thanks to the multidisciplinary collaboration between clinicans, engineers, biologist, etc. that the team of the Laboratory for Research on Translational Cardiology of Hospital Gregorio Marañon of Madrid has been able to set-up.

Chapter 7

Contributions

7.1. Main contributions of this thesis

7.1.1 Journal papers

- **Hernández-Romero I.**, Rivera-Juárez, A., Puertas, C., Zhang-Wang, S., Sánchez-Álamo, B., Martins, R. & Tejedor, A. (2019). Clinical Characteristics and Electrophysiological Mechanisms Underlying Brugada ECG in Patients With Severe Hyperkalemia. Journal of the American Heart Association, 8(3), e010115.
- **Hernández-Romero, I**., Guillem, M. S., Figuera, C., Atienza, F., Fernández-Avilés, F., & Climent, A. M. (2019). Optical imaging of voltage and calcium in isolated hearts: Linking spatiotemporal heterogeneities and ventricular fibrillation initiation. PloS one, 14(5), e0215951.
- **Hernández-Romero, I**., Guillem, M. S., Rodrigo, M., Liberos, A., Atienza, F., Fernández-Avilés, F., & Climent, A. M. Complete-chamber Conduction Velocity Estimation for Electrocardiographic Imaging during Atrial Fibrillation. (Under review)

7.1.2 International conferences

Computing in Cardiology Conference (CinC), 2016. *Mechanism behind hyperkalemic brugada phenocopy: A computational study*
Authors*: I Hernández-Romero, I., Giménez, P., Rivera, A., Figura, C., Guillem, M. S., Fernández-Avilés, F., Climent, AM., Atienza, F.
Year: 2016

Computing in Cardiology Conference (CinC), 2017. *Pathline Strategy for Reconstructing Coherent Conduction Velocity Maps during Arrhythmias*
Authors*: Hernández-Romero, I., Rodrigo M., Liberos A., Figura, C., Guillem, M. S., Fernández-Avilés, F., Atienza, F, Climent, AM
Year: 2017

Frontiers in Cardiovascular Biology 2018. *Electrophysiological characterization of a chronic infarction model with high ventricular tachycardia inducibility rate*
Authors*: I. Hernandez-Romero, A. Liberos, M.S. Guillem, F. Atienza, V. Crisostomo, A. Arenal, A.M. Climent, F. Fernandez-Aviles
Year: 2018

52nd Annual Scientific Meeting of the European Society for Clinical Investigation. *Action potential duration and conduction velocity as predictors of ventricular tachycardia inducibility.*
Authors*: I. Hernandez-Romero, A. Liberos, A. Arenal, P.M. Ruiz-Hernandez, V. Crisostomo, R. Sanz, F. Atienza, M.S. Guillem, J. Bermejo, F.M. Sanchez-Margallo, A.M. Climent.
Year: 2018

Computing in Cardiology Conference (CinC), 2018. *Complete-chamber Conduction Velocity Estimation during Arrhythmias*
Authors*: Hernández-Romero, I., Rodrigo M., Liberos A., Figura, C., Guillem, M. S., Fernández-Avilés, F., Atienza, F, Climent, AM
Year: 2018

Computing in Cardiology Conference (CinC), 2019. *Non-invasive Conduction Velocity Estimation during Sinus Rhythm in atrial fibrillation patients.*
Authors*: Hernández-Romero, I., Rodrigo M., Liberos A., Figura, C., Guillem, M. S., Fernández-Avilés, F., Atienza, F, Climent, AM
Year: 2019

7.1.3 Co-founder of the start-up Corify Care SL

Corify Care is a spin-off that develops a non-invasive high-density group of electrodes and an innovative image processing technology that resolves the main shortcomings of existing solutions in Atrial Fibrillation.
Corify's product will improve the current procedure in patient selection and personalized treatment of Atrial Fibrillation in a high cost-effective way based on ECGI technology. Future versions of the Corify Care product may incorporate software developments fruit of the present thesis.

7.2. Contributions related to this thesis

7.2.1 Journal papers

- Figuera, C., Suárez-Gutiérrez, V., **Hernández-Romero, I.**, Rodrigo, M., Liberos, A., Atienza, F., & Alonso-Atienza, F. (2016). Regularization Techniques for ECG Imaging during Atrial Fibrillation: A Computational Study. Frontiers in physiology, 7, 466.
- Liberos, A., Bueno-Orovio, A., Rodrigo, M., Ravens, U., **Hernandez-Romero, I.**, Fernandez-Aviles, F., & Climent, A. M. (2016). Balance between sodium and calcium currents underlying chronic atrial fibrillation termination: An in silico intersubject variability study. Heart Rhythm, 13(12), 2358-2365.
- Liberos, A., Bueno-Orovio, A., Rodrigo, M., Ravens, U., **Hernandez-Romero, I.**, Fernandez-Aviles, F., & Climent, A. M. (2017). Reply to the Editor-Onmisuse of null hypothesis testing: Analysis of biophysical model simulations. Heart Rhythm, 14(4), e50-e51.

- Rodrigo, M., Climent, A. M., Liberos, A., **Hernández-Romero, I.**, Arenal, Á., Bermejo, J., Fernandez-Aviles, F., Atienza, F.,. & Guillem, M. S. (2018). Solving inaccuracies in anatomical models for electrocardiographic inverse problem resolution by maximizing reconstruction quality. IEEE transactions on medical imaging, 37(3), 733-740.
- Liberos, A., Rodrigo, M., **Hernandez-Romero, I.**, Fernandez-Aviles, F., Atienza, F., Climent, A. M. & Guillem, M. S. (2019). Phase singularity point tracking for the identification of typical and atypical flutter patients: A clinical-computational study. Computers in biology and medicine, 104, 319-328.

7.2.2 Book chapter

- Rodrigo M, Pedrón–Torrecilla J, **Hernández I**, Liberos A, Climent AM, Guillem MS. Data Analysis in cardiac arrhythmias. Eds: Fernández–Llatas C, García–Gómez JM. Data Mining in Clinical Medicine. Methods in Molecular Biology 2015. 1246:217–236.

7.2.3 International conferences

Computing in Cardiology Conference (CinC), 2016. *High Resolution Microscopic Optical Mapping of Anatomical and Functional Reentries in Human Cardiac Cell Cultures.*
Authors*: Climent, AM., I Hernández-Romero, Monserrat, N., Guillem, MS., Atienza, F., Fernández-Avilés, F.
Year: 2016.

European Heart, 2016. *Microscopic analysis of anatomical and functional reentrant mechanisms in human cardiac cell cultures.*
Authors*: Climent, A. M., **Hernandez, I.**, Guillem, M. S., Montserrat, N., Fernandez, M. E., Sanz-Ruiz, R., ... & Fernandez-Aviles, F.
Year: 2016.

Computing in Cardiology Conference (CinC), 2016. *Role of substrate flexibility on cardiac cell culture electrophysiological properties.*
Authors*: Gomez-Cid, L., Fuentes, L., **Hernández-Romero, I.**, Guillem, M.S., Atienza, F., Fernández-Avilés, F., & Climent, A. M.
Year: 2016.

Computing in Cardiology Conference (CinC), 2016. *Noninvasive identification of atrial fibrillation drivers: Simulation and patient data evaluation.*
Authors*: Guillem, M. S., Climent, A. M., Rodrigo, M., **Hernández-Romero, I.**, Liberos, A., Fernandez-Avilés, F., ... & Atienza, F..
Year: 2016.

Computing in Cardiology Conference (CinC), 2017. *Evaluation of inverse problem with slow-conducting channel in scar area in a post-infarction model.*
Authors*: Chen, Z., Rodrigo, M., Liberos, A., **Hernandez-Romero, I**., Requena, J., Climent, A. M., & Guillem, M. S.
Year: 2017

Computing in Cardiology Conference (CinC), 2017. *Including a priori knowledge in the solution of the inverse problem during atrial fibrillation*
Authors*: Suárez-Gutiérrez, V., Cámara, M. Á., Barquero-Pérez, Ó., Hernández, I., Guillem, M. S., Climent, A. M., ... & Figuera, C.
Year: 2017.

Computing in Cardiology Conference (CinC), 2017. *Electrophysiological parameters in the electrical propagation during atrial fibrillation: A population of models study*
Authors*: Simon, A., Liberos, A., **Hernandez-Romero, I.,** Bueno-Orovio, A., Rodrigo, M., Guillem, M. S., ... & Climent, A. M.
Year: 2017.

Computing in Cardiology Conference (CinC), 2017. *Solving inaccuracies in the heart position and orientation for inverse solution by using electric information*
Authors*: Rodrigo, M., Climent, A. M., Liberos, A., **Hernández-Romero, I**., Arenal, A., Bermejo, J., ... & Guillem, M. S.
Year: 2017.

Computing in Cardiology Conference (CinC), 2017. *Personalization of atrial fibrillation antiarrhythmic drug treatments: A population of models approach*
Authors*: Liberos, A., Bueno-Orovio, A., **Hernandez-Romero, I.**, Rodrigo, M., Guillem, M. S., Fernandez-Aviles, F., ... & Climent, A. M.
Year: 2017.

Cardiovascular Research, 2018. *The role of fibroblast-myocyte electrotonic coupling in the formation of unidirectional blocks*
Authors*: Gomez-Cid, L., De La Nava, A. S., Casasnovas-Orus, V., Sanz-Gutierrez, D., Liberos, A., **Hernandez-Romero, I.,** ... & Fernandez-Aviles, F.
Year: 2018.

Cardiovascular Research, 2018. *Inter-subject variability explains juxtaposed effects in pharmacological treatments: an in-silico approach for the personalization of atrial fibrillation drug treatments*
Authors*: Liberos, A., **Hernandez-Romero, I.**, De La Nava, A. S., Rodrigo, M., Bueno-Orovio, A., Rodriguez, B., ... & Fernandez-Aviles, F.
Year: 2018.

Computing in Cardiology Conference (CinC), 2018. *In Silico Safety Pharmacology on Intersubject Variability Population of Models: A Regression Model Approach*
Authors*: De La Nava, A. S., Liberos, A., **Hernandez-Romero, I.**, Guillem, M. S., Atienza, F., Fernandez-Aviles, F., & Climent, A. M.
Year: 2018.

7.3. Research stages

During the development of this thesis Ismael Hernández-Romero has completed two a research stages at:

"University of Michigan", Ann Arbor, Michigan, EEUU, in the "Center for Arrhythmia Research", leaded by Pr. Jose Jalife. Dates: From 1st June until 15th September 2016.

"University of Utah", Salt Lake City, Utah, EEUU, in the "Scientific Computing and Imaging Institute", leaded by Pr. Rob MacLeod. Dates: From 15th May until 15th August 2017.

References

Aistrup GL, Kelly JE, Kapur S, Kowalczyk M, Sysman-Wolpin I, Kadish AH, Wasserstrom JA. 2006. Pacing-induced heterogeneities in intracellular Ca2+ signaling, cardiac alternans, and ventricular arrhythmias in intact rat heart. Circ Res 99(7):e65-73.

Álvarez D, Alonso-Atienza F, Rojo-Álvarez JL, García-Alberola A, Moscoso M. 2012. Shape reconstruction of cardiac ischemia from non-contact intracardiac recordings: A model study. Math Comput Model 55(5-6):1770-81.

Amidror I. 2002. Scattered data interpolation methods for electronic imaging systems: A survey. Journal of Electronic Imaging 11(ARTICLE):157-76.

Antzelevitch C. 2005. Heart rhythm society; european heart rhythm association. brugada syndrome: Report of the second consensus conference: Endorsed by the heart rhythm society and the european heart rhythm association. Circulation 111(5):659-70.

Antzelevitch,Charles, Yan,Gan-Xin, Ackerman M,J., Borggrefe,Martin, Corrado,Domenico, Guo,Jihong, Gussak,Ihor, Hasdemir,Can, Horie,Minoru, Huikuri,Heikki, et al. 2017. J-wave syndromes expert consensus conference report: Emerging concepts and gaps in knowledge. Europace 19(4):665-94.

Ashman R and Byer E. 1943. The normal human ventricular gradient: I. factors which affect its direction and its relation to the mean QRS axis. Am Heart J 25(1):16-35.

Aslanidi OV, Colman MA, Stott J, Dobrzynski H, Boyett MR, Holden AV, Zhang H. 2011. 3D virtual human atria: A computational platform for studying clinical atrial fibrillation. Prog Biophys Mol Biol 107(1):156-68.

Atienza F., Jalife J., Almendral J., Moreno J., Talkachou A., Vaidyanathan R., Arenal A., Villacastin JP, Sanchez A. and Torrecilla EG. 2005. Adenosine accelerates drivers and increases frequency gradients differently in paroxysmal versus persistent human

atrial fibrillation. CirculationLIPPINCOTT WILLIAMS & WILKINS 530 WALNUT ST, PHILADELPHIA, PA 19106-3261 USA. U763 p.

Atienza F, Almendral J, Jalife J, Zlochiver S, Ploutz-Snyder R, Torrecilla EG, Arenal A, Kalifa J, Fernández-Avilés F, Berenfeld O. 2009. Real-time dominant frequency mapping and ablation of dominant frequency sites in atrial fibrillation with left-to-right frequency gradients predicts long-term maintenance of sinus rhythm. Heart Rhythm 6(1):33-40.

Atienza F, Almendral J, Moreno J, Vaidyanathan R, Talkachou A, Kalifa J, Arenal A, Villacastin JP, Torrecilla EG, Sanchez A, et al. 2006. Activation of inward rectifier potassium channels accelerates atrial fibrillation in humans: Evidence for a reentrant mechanism. Circulation 114(23):2434-42.

Banville I and Gray RA. 2002. Effect of action potential duration and conduction velocity restitution and their spatial dispersion on alternans and the stability of arrhythmias. J Cardiovasc Electrophysiol 13(11):1141-9.

Baranchuk A, Nguyen T, Ryu MH, Femenía F, Zareba W, Wilde AA, Shimizu W, Brugada P, Pérez-Riera AR. 2012. Brugada phenocopy: New terminology and proposed classification. Annals of Noninvasive Electrocardiology 17(4):299-314.

Barber CB, Dobkin DP, Dobkin DP, Huhdanpaa H. 1996. The quickhull algorithm for convex hulls. ACM Transactions on Mathematical Software (TOMS) 22(4):469-83.

Bayly PV, KenKnight BH, Rogers JM, Hillsley RE, Ideker RE, Smith WM. 1998. Estimation of conduction velocity vector fields from epicardial mapping data. IEEE Transactions on Biomedical Engineering 45(5):563-71.

Bers DM. 2002. Cardiac excitation–contraction coupling. Nature 415(6868):198.

Bezzina CR, Barc J, Mizusawa Y, Remme CA, Gourraud J, Simonet F, Verkerk AO, Schwartz PJ, Crotti L, Dagradi F. 2013. Common variants at SCN5A-SCN10A and HEY2 are associated with brugada syndrome, a rare disease with high risk of sudden cardiac death. Nat Genet 45(9):1044.

Blanc O, Virag N, Vesin J, Kappenberger L. 2001. A computer model of human atria with reasonable computation load and realistic anatomical properties. IEEE Transactions on Biomedical Engineering 48(11):1229-37.

Bommes David and Kobbelt Leif. 2007. Accurate computation of geodesic distance fields for polygonal curves on triangle meshes. Vmv. 151 p.

Brooks DH and MacLeod RS. 1997. Electrical imaging of the heart. IEEE Signal Process Mag 14(1):24-42.

Brugada P and Brugada J. 1992. Right bundle branch block, persistent ST segment elevation and sudden cardiac death: A distinct clinical and electrocardiographic syndrome: A multicenter report. J Am Coll Cardiol 20(6):1391-6.

Brundel BJ, Van Gelder IC, Henning RH, Tieleman RG, Tuinenburg AE, Wietses M, Grandjean JG, Van Gilst WH, Crijns HJ. 2001. Ion channel remodeling is related to intraoperative atrial effective refractory periods in patients with paroxysmal and persistent atrial fibrillation. Circulation 103(5):684-90.

Bruns H, Eckardt L, Vahlhaus C, Schulze-Bahr E, Haverkamp W, Borggrefe M, Breithardt G, Wichter T. 2002. Body surface potential mapping in patients with brugada syndrome: Right precordial ST segment variations and reverse changes in left precordial leads. Cardiovasc Res 54(1):58-66.

Burdumy M, Luik A, Neher P, Hanna R, Krueger MW, Schilling C, Barschdorf H, Lorenz C, Seemann G, Schmitt C. 2012. Comparing measured and simulated wave directions in the left atrium–a workflow for model personalization and validation. Biomedizinische Technik/Biomedical Engineering 57(2):79-87.

Burstein B and Nattel S. 2008. Atrial fibrosis: Mechanisms and clinical relevance in atrial fibrillation. J Am Coll Cardiol 51(8):802-9.

Calkins H, Reynolds MR, Spector P, Sondhi M, Xu Y, Martin A, Williams CJ, Sledge I. 2009. Treatment of atrial fibrillation with antiarrhythmic drugs or radiofrequency ablation: Two systematic literature reviews and meta-analyses. Circulation: Arrhythmia and Electrophysiology 2(4):349-61.

Calkins H, Hindricks G, Cappato R, Kim Y, Saad EB, Aguinaga L, Akar JG, Badhwar V, Brugada J, Camm J. 2017. 2017 HRS/EHRA/ECAS/APHRS/SOLAECE expert consensus statement on catheter and surgical ablation of atrial fibrillation. Ep Europace 20(1):e1-e160.

Cantwell CD, Roney CH, Ng FS, Siggers JH, Sherwin SJ, Peters NS. 2015. Techniques for automated local activation time annotation and conduction velocity estimation in cardiac mapping. Comput Biol Med 65:229-42.

Cao JM, Qu Z, Kim YH, Wu TJ, Garfinkel A, Weiss JN, Karagueuzian HS, Chen PS. 1999. Spatiotemporal heterogeneity in the induction of ventricular fibrillation by rapid pacing: Importance of cardiac restitution properties. Circ Res 84(11):1318-31.

Cardone-Noott L, Bueno-Orovio A, Mincholé A, Zemzemi N, Rodriguez B. 2016. Human ventricular activation sequence and the simulation of the electrocardiographic QRS complex and its variability in healthy and intraventricular block conditions. EP Europace 18(suppl_4):iv4-iv15.

Choi B and Salama G. 2000. Simultaneous maps of optical action potentials and calcium transients in guinea-pig hearts: Mechanisms underlying concordant alternans. J Physiol (Lond) 529(1):171-88.

Choi PT, Lam KC, Lui LM. 2015. FLASH: Fast landmark aligned spherical harmonic parameterization for genus-0 closed brain surfaces. SIAM Journal on Imaging Sciences 8(1):67-94.

Chorro FJ, Canoves J, Guerrero J, Mainar L, Sanchis J, Such L, Lopez-Merino V. 2000. Alteration of ventricular fibrillation by flecainide, verapamil, and sotalol: An experimental study. Circulation 101(13):1606-15.

Chudin E, Goldhaber J, Garfinkel A, Weiss J, Kogan B. 1999. Intracellular ca 2 dynamics and the stability of ventricular tachycardia. Biophys J 77(6):2930-41.

Clayton R and Panfilov A. 2008. A guide to modelling cardiac electrical activity in anatomically detailed ventricles. Prog Biophys Mol Biol 96(1-3):19-43.

Colman MA, Aslanidi OV, Kharche S, Boyett MR, Garratt C, Hancox JC, Zhang H. 2013. Pro-arrhythmogenic effects of atrial fibrillation-induced electrical remodelling: Insights from the three-dimensional virtual human atria. J Physiol (Lond) 591(17):4249-72.

Coronel R, Casini S, Koopmann TT, Wilms-Schopman FJ, Verkerk AO, de Groot JR, Bhuiyan Z, Bezzina CR, Veldkamp MW, Linnenbank AC, et al. 2005. Right ventricular fibrosis and conduction delay in a patient with clinical signs of brugada syndrome: A combined electrophysiological, genetic, histopathologic, and computational study. Circulation 112(18):2769-77.

Corradi D, Callegari S, Maestri R, Ferrara D, Mangieri D, Alinovi R, Mozzoni P, Pinelli S, Goldoni M, Privitera YA. 2012. Differential structural remodeling of the left-atrial posterior wall in patients affected by mitral regurgitation with or without persistent atrial fibrillation: A morphological and molecular study. J Cardiovasc Electrophysiol 23(3):271-9.

Corrado D, Zorzi A, Cerrone M, Rigato I, Mongillo M, Bauce B, Delmar M. 2016. Relationship between arrhythmogenic right ventricular cardiomyopathy and brugada syndrome: New insights from molecular biology and clinical implications. Circulation: Arrhythmia and Electrophysiology 9(4):e003631.

Courtemanche M, Ramirez RJ, Nattel S. 1998. Ionic mechanisms underlying human atrial action potential properties: Insights from a mathematical model. American Journal of Physiology-Heart and Circulatory Physiology 275(1):H301-21.

Cuculich PS, Zhang J, Wang Y, Desouza KA, Vijayakumar R, Woodard PK, Rudy Y. 2011. The electrophysiological cardiac ventricular substrate in patients after myocardial infarction: Noninvasive characterization with electrocardiographic imaging. J Am Coll Cardiol 58(18):1893-902.

Dallet C, Roney C, Martin R, Kitamura T, Puyo S, Duchâteau J, Dumas-Pomier C, Ravon G, Bear L, Derval N. 2018. Cardiac propagation pattern mapping with vector field for helping tachyarrhythmias diagnosis with clinical tridimensional electro-

anatomical mapping tools. IEEE Transactions on Biomedical Engineering 66(2):373-82.

Dam PMV and Oosterom AV. 2003. Atrial excitation assuming uniform propagation. J Cardiovasc Electrophysiol 14:S166-71.

Dang L, Virag N, Ihara Z, Jacquemet V, Vesin J, Schlaepfer J, Ruchat P, Kappenberger L. 2005. Evaluation of ablation patterns using a biophysical model of atrial fibrillation. Ann Biomed Eng 33(4):465-74.

de Diego C, Pai RK, Dave AS, Lynch A, Thu M, Chen F, Xie LH, Weiss JN, Valderrabano M. 2008. Spatially discordant alternans in cardiomyocyte monolayers. Am J Physiol Heart Circ Physiol 294(3):H1417-25.

Di Diego JM, Cordeiro JM, Goodrow RJ, Fish JM, Zygmunt AC, Perez GJ, Scornik FS, Antzelevitch C. 2002. Ionic and cellular basis for the predominance of the brugada syndrome phenotype in males. Circulation 106(15):2004-11.

Dössel O, Krueger MW, Weber FM, Wilhelms M, Seemann G. 2012. Computational modeling of the human atrial anatomy and electrophysiology. Med Biol Eng Comput 50(8):773-99.

Dubuc M, Nadeau R, Tremblay G, Kus T, Molin F, Savard P. 1993. Pace mapping using body surface potential maps to guide catheter ablation of accessory pathways in patients with wolff-parkinson-white syndrome. Circulation 87(1):135-43.

Dutta S, Mincholé A, Quinn TA, Rodriguez B. 2017. Electrophysiological properties of computational human ventricular cell action potential models under acute ischemic conditions. Prog Biophys Mol Biol 129:40-52.

Eckardt L, BRUNS H, Paul M, Kirchhof P, SCHULZE-BAHR E, Wichter T, BREITHARDT G, Borggrefe M, Haverkamp W. 2002. Body surface area of ST elevation and the presence of late potentials correlate to the inducibility of ventricular tachyarrhythmias in brugada syndrome. J Cardiovasc Electrophysiol 13(8):742-9.

Einthoven W. 1906. Le tl cardiogramme. Arch Internat Physiol 4:132.

Figuera C, Suárez-Gutiérrez V, Hernández-Romero I, Rodrigo M, Liberos A, Atienza F, Guillem MS, Barquero-Pérez Ó, Climent AM, Alonso-Atienza F. 2016. Regularization techniques for ECG imaging during atrial fibrillation: A computational study. Frontiers in Physiology 7:466.

Finlay DD, Nugent CD, McCullagh PJ, Black ND. 2005. Mining for diagnostic information in body surface potential maps: A comparison of feature selection techniques. Biomedical Engineering Online 4(1):51.

Frustaci A, Priori SG, Pieroni M, Chimenti C, Napolitano C, Rivolta I, Sanna T, Bellocci F, Russo MA. 2005. Cardiac histological substrate in patients with clinical phenotype of brugada syndrome. Circulation 112(24):3680-7.

Fuster V, Rydén LE, Cannom DS, Crijns HJ, Curtis AB, Ellenbogen KA, Halperin JL, Le Heuzey J, Kay GN, Lowe JE. 2006. ACC/AHA/ESC 2006 guidelines for the management of patients with atrial fibrillation: A report of the american college of cardiology/american heart association task force on practice guidelines and the european society of cardiology committee for practice guidelines (writing committee to revise the 2001 guidelines for the management of patients with atrial fibrillation) developed in collaboration with the european heart rhythm association and the heart rhythm society. J Am Coll Cardiol 48(4):e149-246.

García-Molla VM, Liberos A, Vidal A, Guillem M, Millet J, Gonzalez A, Martínez-Zaldívar F, Climent AM. 2014. Adaptive step ODE algorithms for the 3D simulation of electric heart activity with graphics processing units. Comput Biol Med 44:15-26.

Garfinkel A, Kim YH, Voroshilovsky O, Qu Z, Kil JR, Lee MH, Karagueuzian HS, Weiss JN, Chen PS. 2000. Preventing ventricular fibrillation by flattening cardiac restitution. Proc Natl Acad Sci U S A 97(11):6061-6.

Giudicessi JR, Ye D, Tester DJ, Crotti L, Mugione A, Nesterenko VV, Albertson RM, Antzelevitch C, Schwartz PJ, Ackerman MJ. 2011. Transient outward current (I to) gain-of-function mutations in the KCND3-encoded Kv4. 3 potassium channel and brugada syndrome. Heart Rhythm 8(7):1024-32.

Gizzi A, Cherry E, Gilmour Jr RF, Luther S, Filippi S, Fenton FH. 2013. Effects of pacing site and stimulation history on alternans dynamics and the development of complex spatiotemporal patterns in cardiac tissue. Frontiers in Physiology 4:71.

Grandi E, Pandit SV, Voigt N, Workman AJ, Dobrev D, Jalife J, Bers DM. 2011. Human atrial action potential and Ca2 model: Sinus rhythm and chronic atrial fibrillation. Circ Res 109(9):1055-66.

Gu Xianfeng, Gortler Steven J. and Hoppe Hugues. 2002. Geometry images. ACM transactions on graphics (TOG)ACM. 355 p.

Guillem MS, Climent AM, Millet J, Berne P, Ramos R, Brugada J, Brugada R. 2016a. Spatiotemporal characteristics of QRS complexes enable the diagnosis of brugada syndrome regardless of the appearance of a type 1 ECG. J Cardiovasc Electrophysiol 27:563-70.

Guillem Maria S., Climent Andreu M., Millet José, Berne Paola, Ramos Rafael, Brugada Josep and Brugada Ramon. 2010. Conduction abnormalities in the right ventricular outflow tract in brugada syndrome detected body surface potential mapping. 2010 annual international conference of the IEEE engineering in medicine and biologyIEEE. 2537 p.

Guillem MS, Climent AM, Millet J, Arenal Á, Fernández-Avilés F, Jalife J, Atienza F, Berenfeld O. 2013. Noninvasive localization of maximal frequency sites of atrial fibrillation by body surface potential mapping. Circulation: Arrhythmia and Electrophysiology 6(2):294-301.

Guillem MS, Climent AM, Castells F, Husser D, Millet J, Arya A, Piorkowski C, Bollmann A. 2009a. Noninvasive mapping of human atrial fibrillation. J Cardiovasc Electrophysiol 20(5):507-13.

Guillem MS, Climent AM, Rodrigo M, Fernández-Avilés F, Atienza F, Berenfeld O. 2016b. Presence and stability of rotors in atrial fibrillation: Evidence and therapeutic implications. Cardiovasc Res 109(4):480-92.

Guillem M, Quesada A, Donis V, Climent A, Mihi N, Millet J, Castells F. 2009b. Surface wavefront propagation maps: Non-invasive characterization of atrial flutter circuit. Int J Bioelectromagn 11:22-6.

Gulrajani RM. 1998. The forward and inverse problems of electrocardiography. IEEE Engineering in Medicine and Biology Magazine 17(5):84-101.

Haïssaguerre M, Shah DC, Jaïs P, Hocini M, Yamane T, Deisenhofer I, Chauvin M, Garrigue S, Clémenty J. 2000. Electrophysiological breakthroughs from the left atrium to the pulmonary veins. Circulation 102(20):2463-5.

Haissaguerre M, Shah DC, Jais P, Clementy J. 1997. Role of catheter ablation for atrial fibrillation. Curr Opin Cardiol 12(1):18-23.

Harada M, Tsuji Y, Ishiguro YS, Takanari H, Okuno Y, Inden Y, Honjo H, Lee JK, Murohara T, Sakuma I, et al. 2011. Rate-dependent shortening of action potential duration increases ventricular vulnerability in failing rabbit heart. Am J Physiol Heart Circ Physiol 300(2):H565-73.

Hayashi H, Shiferaw Y, Sato D, Nihei M, Lin S, Chen P, Garfinkel A, Weiss JN, Qu Z. 2007. Dynamic origin of spatially discordant alternans in cardiac tissue. Biophys J 92(2):448-60.

Hayashi M, Shimizu W, Albert CM. 2015. The spectrum of epidemiology underlying sudden cardiac death. Circ Res 116(12):1887-906.

Hirayama Y, Saitoh H, Atarashi H, Hayakawa H. 1993. Electrical and mechanical alternans in canine myocardium in vivo. dependence on intracellular calcium cycling. Circulation 88(6):2894-902.

Hodgkin AL and Huxley AF. 1952. A quantitative description of membrane current and its application to conduction and excitation in nerve. J Physiol (Lond) 117(4):500-44.

Hoekema R, Uijen G, Van Oosterom A. 1999. On selecting a body surface mapping procedure. J Electrocardiol 32(2):93-101.

Honarbakhsh S, Schilling RJ, Orini M, Providencia R, Keating E, Finlay M, Sporton S, Chow A, Earley MJ, Lambiase PD. 2019. Structural remodeling and conduction velocity dynamics in the human left atrium: Relationship with reentrant mechanisms sustaining atrial fibrillation. Heart Rhythm 16(1):18-25.

Hoogendijk MG, Opthof T, Postema PG, Wilde AA, de Bakker JM, Coronel R. 2010a. The brugada ECG pattern: A marker of channelopathy, structural heart disease, or neither? toward a unifying mechanism of the brugada syndrome. Circulation: Arrhythmia and Electrophysiology 3(3):283-90.

Hoogendijk MG, Potse M, Linnenbank AC, Verkerk AO, den Ruijter HM, van Amersfoorth SC, Klaver EC, Beekman L, Bezzina CR, Postema PG. 2010b. Mechanism of right precordial ST-segment elevation in structural heart disease: Excitation failure by current-to-load mismatch. Heart Rhythm 7(2):238-48.

Horácek BM and Clements JC. 1997a. The inverse problem of electrocardiography: A solution in terms of single-and double-layer sources on the epicardial surface. Math Biosci 144(2):119-54.

Horácek BM and Clements JC. 1997b. The inverse problem of electrocardiography: A solution in terms of single-and double-layer sources on the epicardial surface. Math Biosci 144(2):119-54.

Hwang GS, Hayashi H, Tang L, Ogawa M, Hernandez H, Tan AY, Li H, Karagueuzian HS, Weiss JN, Lin SF, et al. 2006. Intracellular calcium and vulnerability to fibrillation and defibrillation in langendorff-perfused rabbit ventricles. Circulation 114(24):2595-603.

Ikeda T, Yoshino H, Sugi K, Tanno K, Shimizu H, Watanabe J, Kasamaki Y, Yoshida A, Kato T. 2006. Predictive value of microvolt T-wave alternans for sudden cardiac death in patients with preserved cardiac function after acute myocardial infarction: Results of a collaborative cohort study. J Am Coll Cardiol 48(11):2268-74.

Issa ZF, Miller JM, Zipes DP. 2009. Clinical arrhythmology and electrophysiology: A companion to braunwald's heart disease. Elsevier Health Sciences.

Iyer V, Mazhari R, Winslow RL. 2004. A computational model of the human left-ventricular epicardial myocyte. Biophys J 87(3):1507-25.

Jacquemet V, Virag N, Ihara Z, Dang L, Blanc O, Zozor S, VESIN J, Kappenberger L, Henriquez C. 2003. Study of unipolar electrogram morphology in a computer model of atrial fibrillation. J Cardiovasc Electrophysiol 14:S172-9.

Jalife J, Delmar M, Anumonwo J, Berenfeld O, Kalifa J. 2011. Basic cardiac electrophysiology for the clinician. John Wiley & Sons.

Jia P, Ramanathan C, Ghanem RN, Ryu K, Varma N, Rudy Y. 2006. Electrocardiographic imaging of cardiac resynchronization therapy in heart failure: Observation of variable electrophysiologic responses. Heart Rhythm 3(3):296-310.

Jin Q, Dosdall DJ, Li L, Rogers JM, Ideker RE, Huang J. 2014. Verapamil reduces incidence of reentry during ventricular fibrillation in pigs. Am J Physiol Heart Circ Physiol 307(9):H1361-9.

John Camm A, Lip GY, De Caterina R, Savelieva I, Atar D, Hohnloser SH, Hindricks G, Kirchhof P. 2013. '2012 focused update of the ESC guidelines for the management of atrial fibrillation'[eur heart J (2012); 33 (21): 2719–2747]. Eur Heart J 34(10):790-.

Karma A. 1994. Electrical alternans and spiral wave breakup in cardiac tissue. Chaos: An Interdisciplinary Journal of Nonlinear Science 4(3):461-72.

Karma A and Gilmour Jr RF. 2007. Nonlinear dynamics of heart rhythm disorders. Phys Today 60(3):51-7.

Kay MW and Gray RA. 2005. Measuring curvature and velocity vector fields for waves of cardiac excitation in 2-D media. IEEE Transactions on Biomedical Engineering 52(1):50-63.

Kessler EL, Boulaksil M, van Rijen HV, Vos MA, van Veen TA. 2015. Passive ventricular remodeling in cardiac disease: Focus on heterogeneity. Remodeling of Cardiac Passive Electrical Properties and Susceptibility to Ventricular and Atrial Arrhythmias :54.

Kharche S, Garratt CJ, Boyett MR, Inada S, Holden AV, Hancox JC, Zhang H. 2008. Atrial proarrhythmia due to increased inward rectifier current (IK1) arising from KCNJ2 mutation–a simulation study. Prog Biophys Mol Biol 98(2-3):186-97.

Kléber AG and Rudy Y. 2004. Basic mechanisms of cardiac impulse propagation and associated arrhythmias. Physiol Rev 84(2):431-88.

Koivumäki JT, Korhonen T, Tavi P. 2011. Impact of sarcoplasmic reticulum calcium release on calcium dynamics and action potential morphology in human atrial myocytes: A computational study. PLoS Computational Biology 7(1):e1001067.

Koivumäki JT, Seemann G, Maleckar MM, Tavi P. 2014. In silico screening of the key cellular remodeling targets in chronic atrial fibrillation. PLoS Computational Biology 10(5):e1003620.

Krogh-Madsen T and Christini DJ. 2012. Nonlinear dynamics in cardiology. Annu Rev Biomed Eng 14:179-203.

Krueger MW, Dorn A, Keller DU, Holmqvist F, Carlson J, Platonov PG, Rhode KS, Razavi R, Seemann G, Dössel O. 2013. In-silico modeling of atrial repolarization in normal and atrial fibrillation remodeled state. Med Biol Eng Comput 51(10):1105-19.

Krueger Martin W., Schmidt Viktor, Tobón Catalina, Weber Frank M., Lorenz Cristian, Keller David UJ, Barschdorf Hans, Burdumy Michael, Neher Peter and Plank Gernot. 2011. Modeling atrial fiber orientation in patient-specific geometries: A semi-automatic rule-based approach. International conference on functional imaging and modeling of the heartSpringer. 223 p.

Krummen DE, Ho G, Villongco CT, Hayase J, Schricker AA. 2016. Ventricular fibrillation: Triggers, mechanisms and therapies. Future Cardiology 12(3):373-90.

Laughner JI, Ng FS, Sulkin MS, Arthur RM, Efimov IR. 2012. Processing and analysis of cardiac optical mapping data obtained with potentiometric dyes. Am J Physiol Heart Circ Physiol 303(7):H753-65.

Lee P, Yan P, Ewart P, Kohl P, Loew LM, Bollensdorff C. 2012. Simultaneous measurement and modulation of multiple physiological parameters in the isolated heart using optical techniques. Pflügers Archiv-European Journal of Physiology 464(4):403-14.

Liberos A, Bueno-Orovio A, Rodrigo M, Ravens U, Hernandez-Romero I, Fernandez-Aviles F, Guillem MS, Rodriguez B, Climent AM. 2016. Balance between sodium and calcium currents underlying chronic atrial fibrillation termination: An in silico intersubject variability study. Heart Rhythm 13(12):2358-65.

Littmann L, Monroe MH, Taylor L, Brearley WD. 2007. The hyperkalemic brugada sign. J Electrocardiol 40(1):53-9.

Luo CH and Rudy Y. 1991. A model of the ventricular cardiac action potential. depolarization, repolarization, and their interaction. Circ Res 68(6):1501-26.

MacLeod RS, Gardner M, Miller RM, HORÁČUEK BM. 1995. Application of an electrocardiographic inverse solution to localize ischemia during coronary angioplasty. J Cardiovasc Electrophysiol 6(1):2-18.

MacLeod RS, Johnson CR and Ershler PR. 1991. Construction of an inhomegeneous model of the human torso for use in computational electrocardiography. Proceedings of the annual international conference of the IEEE engineering in medicine and biology society volume 13: 1991IEEE. 688 p.

Makinose M and Hasselbach W. 1971. ATP synthesis by the reverse of the sarcoplasmic calcium pump. FEBS Lett 12(5):271-2.

Maleckar MM, Greenstein JL, Giles WR, Trayanova NA. 2009. K current changes account for the rate dependence of the action potential in the human atrial myocyte. American Journal of Physiology-Heart and Circulatory Physiology 297(4):H1398-410.

Maleckar MM, Greenstein JL, Trayanova NA, Giles WR. 2008. Mathematical simulations of ligand-gated and cell-type specific effects on the action potential of human atrium. Prog Biophys Mol Biol 98(2-3):161-70.

Malmivuo J and Plonsey R. 1996. Bioelectromagnetism. Medical and Biological Engineering and Computing 34:9-12.

Malmivuo P, Malmivuo J, Plonsey R. 1995. Bioelectromagnetism: Principles and applications of bioelectric and biomagnetic fields. Oxford University Press, USA.

Mansour M, Mandapati R, Berenfeld O, Chen J, Samie FH, Jalife J. 2001. Left-to-right gradient of atrial frequencies during acute atrial fibrillation in the isolated sheep heart. Circulation 103(21):2631-6.

Marrouche NF, Wilber D, Hindricks G, Jais P, Akoum N, Marchlinski F, Kholmovski E, Burgon N, Hu N, Mont L. 2014. Association of atrial tissue fibrosis identified by delayed enhancement MRI and atrial fibrillation catheter ablation: The DECAAF study. Jama 311(5):498-506.

McAllister RE, Noble D, Tsien R. 1975. Reconstruction of the electrical activity of cardiac purkinje fibres. J Physiol (Lond) 251(1):1-59.

McDowell KS, Vadakkumpadan F, Blake R, Blauer J, Plank G, MacLeod RS, Trayanova NA. 2012. Methodology for patient-specific modeling of atrial fibrosis as a substrate for atrial fibrillation. J Electrocardiol 45(6):640-5.

Mironov S, Jalife J, Tolkacheva EG. 2008. Role of conduction velocity restitution and short-term memory in the development of action potential duration alternans in isolated rabbit hearts. Circulation 118(1):17-25.

Moe GK. 1962. On the multiple wavelet hypothesis of atrial fibrillation. Arch Int Pharmacodyn Ther 140:183.

Morotti S, Grandi E, Summa A, Ginsburg KS, Bers DM. 2012. Theoretical study of l-type Ca2 current inactivation kinetics during action potential repolarization and early afterdepolarizations. J Physiol (Lond) 590(18):4465-81.

Nachimuthu S, Assar MD, Schussler JM. 2012. Drug-induced QT interval prolongation: Mechanisms and clinical management. Therapeutic Advances in Drug Safety 3(5):241-53.

Nademanee K, Hocini M, Haïssaguerre M. 2017. Epicardial substrate ablation for brugada syndrome. Heart Rhythm 14(3):457-61.

Nademanee K, McKenzie J, Kosar E, Schwab M, Sunsaneewitayakul B, Vasavakul T, Khunnawat C, Ngarmukos T. 2004. A new approach for catheter ablation of atrial fibrillation: Mapping of the electrophysiologic substrate. J Am Coll Cardiol 43(11):2044-53.

Nattel S. 2002. New ideas about atrial fibrillation 50 years on. Nature 415(6868):219.

Nattel S. 1998. Experimental evidence for proarrhythmic mechanisms of antiarrhythmic drugs. Cardiovasc Res 37(3):567-77.

Nattel S and Singh BN. 1999. Evolution, mechanisms, and classification of antiarrhythmic drugs: Focus on class III actions. Am J Cardiol 84(9):11-9.

Nieuwlaat R, Capucci A, Camm AJ, Olsson SB, Andresen D, Davies DW, Cobbe S, Breithardt G, Le Heuzey J, Prins MH. 2005. Atrial fibrillation management: A prospective survey in ESC member countries: The euro heart survey on atrial fibrillation. Eur Heart J 26(22):2422-34.

Noble D. 1962. A modification of the Hodgkin—Huxley equations applicable to purkinje fibre action and pacemaker potentials. J Physiol (Lond) 160(2):317-52.

Nolasco J and Dahlen RW. 1968. A graphic method for the study of alternation in cardiac action potentials. J Appl Physiol 25(2):191-6.

Noujaim SF, Auerbach DS, Jalife J. 2007. Ventricular fibrillation. Circulation Journal 71(SupplementA):A1-A11.

Nygren A, Fiset C, Firek L, Clark J, Lindblad D, Clark R, Giles W. 1998. Mathematical model of an adult human atrial cell: The role of K currents in repolarization. Circ Res 82(1):63-81.

O'Hara T, Virág L, Varró A, Rudy Y. 2011. Simulation of the undiseased human cardiac ventricular action potential: Model formulation and experimental validation. PLoS Comput Biol 7(5):e1002061.

Opthof T, Remme CA, Jorge E, Noriega F, Wiegerinck RF, Tasiam A, Beekman L, Alvarez-Garcia J, Munoz-Guijosa C, Coronel R. 2017. Cardiac activation–repolarization patterns and ion channel expression mapping in intact isolated normal human hearts. Heart Rhythm 14(2):265-72.

Oral H, Knight BP, Tada H, Özaydın M, Chugh A, Hassan S, Scharf C, Lai SW, Greenstein R, Pelosi Jr F. 2002. Pulmonary vein isolation for paroxysmal and persistent atrial fibrillation. Circulation 105(9):1077-81.

Oral H, Chugh A, Good E, Wimmer A, Dey S, Gadeela N, Sankaran S, Crawford T, Sarrazin JF, Kuhne M, et al. 2007. Radiofrequency catheter ablation of chronic atrial fibrillation guided by complex electrograms. Circulation 115(20):2606-12.

Oster HS and Rudy Y. 1997. Regional regularization of the electrocardiographic inverse problem: A model study using spherical geometry. IEEE Transactions on Biomedical Engineering 44(2):188-99.

Oster HS, Taccardi B, Lux RL, Ershler PR, Rudy Y. 1997. Noninvasive electrocardiographic imaging: Reconstruction of epicardial potentials, electrograms, and isochrones and localization of single and multiple electrocardiac events. Circulation 96(3):1012-24.

Pastore JM, Girouard SD, Laurita KR, Akar FG, Rosenbaum DS. 1999. Mechanism linking T-wave alternans to the genesis of cardiac fibrillation. Circulation 99(10):1385-94.

Pedrón-Torrecilla J, Rodrigo M, Climent AM, Liberos A, Pérez-David E, Bermejo J, Arenal A, Millet J, Fernández-Avilés F, Berenfeld O. 2016. Noninvasive estimation of epicardial dominant high-frequency regions during atrial fibrillation. J Cardiovasc Electrophysiol 27(4):435-42.

Pelleg A, Mitamura H, Price R, Kaplinsky E, Menduke H, Dreifus LS, Michelson EL. 1989. Extracellular potassium ion dynamics and ventricular arrhythmias in the canine heart. J Am Coll Cardiol 13(4):941-50.

Praun Emil and Hoppe Hugues. 2003. Spherical parametrization and remeshing. ACM transactions on graphics (TOG)ACM. 340 p.

Priori SG, Wilde AA, Horie M, Cho Y, Behr ER, Berul C, Blom N, Brugada J, Chiang C, Huikuri H. 2013. HRS/EHRA/APHRS expert consensus statement on the diagnosis and management of patients with inherited primary arrhythmia syndromes. Heart Rhythm 10:1932-63.

Probst V, Veltmann C, Eckardt L, Meregalli PG, Gaita F, Tan HL, Babuty D, Sacher F, Giustetto C, Schulze-Bahr E, et al. 2010. Long-term prognosis of patients diagnosed with brugada syndrome: Results from the FINGER brugada syndrome registry. Circulation 121(5):635-43.

Pruvot EJ, Katra RP, Rosenbaum DS, Laurita KR. 2004. Role of calcium cycling versus restitution in the mechanism of repolarization alternans. Circ Res 94(8):1083-90.

Pueyo E, Smetana P, Caminal P, De Luna AB, Malik M, Laguna P. 2004. Characterization of QT interval adaptation to RR interval changes and its use as a risk-stratifier of arrhythmic mortality in amiodarone-treated survivors of acute myocardial infarction. IEEE Transactions on Biomedical Engineering 51(9):1511-20.

Qu Z, Garfinkel A, Chen PS, Weiss JN. 2000. Mechanisms of discordant alternans and induction of reentry in simulated cardiac tissue. Circulation 102(14):1664-70.

Quintanilla JG, Moreno J, Archondo T, Alfonso-Almazán JM, Lillo-Castellano JM, Usandizaga E, García-Torrent MJ, Rodríguez-Bobada C, González P, Borrego L. 2017. QRS duration reflects underlying changes in conduction velocity during increased intraventricular pressure and heart failure. Prog Biophys Mol Biol .

Reumann M, Bohnert J, Seemann G, Osswald B, Dossel O. 2008. Preventive ablation strategies in a biophysical model of atrial fibrillation based on realistic anatomical data. IEEE Transactions on Biomedical Engineering 55(2):399-406.

Riccio ML, Koller ML, Gilmour RF,Jr. 1999. Electrical restitution and spatiotemporal organization during ventricular fibrillation. Circ Res 84(8):955-63.

Rodrigo M, Pedrón-Torecilla J, Hernández I, Liberos A, Climent AM, Guillem MS. 2015. Data analysis in cardiac arrhythmias. In: Data mining in clinical medicine. Springer. 217 p.

Rodrigo M, Climent AM, Liberos A, Hernández-Romero I, Arenal Á, Bermejo J, Fernández-Avilés F, Atienza F, Guillem MS. 2017. Solving inaccuracies in anatomical models for electrocardiographic inverse problem resolution by maximizing reconstruction quality. IEEE Trans Med Imaging 37(3):733-40.

Rodrigo M, Guillem MS, Climent AM, Pedrón-Torrecilla J, Liberos A, Millet J, Fernández-Avilés F, Atienza F, Berenfeld O. 2014. Body surface localization of left and right atrial high-frequency rotors in atrial fibrillation patients: A clinical-computational study. Heart Rhythm 11(9):1584-91.

Roney CH, Whitaker J, Sim I, O'Neill L, Mukherjee RK, Razeghi O, Vigmond EJ, Wright M, O'Neill MD, Williams SE. 2019. A technique for measuring anisotropy in atrial conduction to estimate conduction velocity and atrial fibre direction. Comput Biol Med 104:278-90.

Samie FH, Mandapati R, Gray RA, Watanabe Y, Zuur C, Beaumont J, Jalife J. 2000. A mechanism of transition from ventricular fibrillation to tachycardia : Effect of calcium channel blockade on the dynamics of rotating waves. Circ Res 86(6):684-91.

Sanders P, Berenfeld O, Hocini M, Jaïs P, Vaidyanathan R, Hsu L, Garrigue S, Takahashi Y, Rotter M, Sacher F. 2005. Spectral analysis identifies sites of high-frequency activity maintaining atrial fibrillation in humans. Circulation 112(6):789-97.

Sato D, Bers DM, Shiferaw Y. 2013. Formation of spatially discordant alternans due to fluctuations and diffusion of calcium. PloS One 8(12):e85365.

Schotten U, Ausma J, Stellbrink C, Sabatschus I, Vogel M, Frechen D, Schoendube F, Hanrath P, Allessie MA. 2001. Cellular mechanisms of depressed atrial contractility in patients with chronic atrial fibrillation. Circulation 103(5):691-8.

Schotten U, Greiser M, Benke D, Buerkel K, Ehrenteidt B, Stellbrink C, Vazquez-Jimenez JF, Schoendube F, Hanrath P, Allessie M. 2002. Atrial fibrillation-induced

atrial contractile dysfunction: A tachycardiomyopathy of a different sort. Cardiovasc Res 53(1):192-201.

Silva JN, Ghosh S, Bowman TM, Rhee EK, Woodard PK, Rudy Y. 2009. Cardiac resynchronization therapy in pediatric congenital heart disease: Insights from noninvasive electrocardiographic imaging. Heart Rhythm 6(8):1178-85.

SippensGroenewegen A, Peeters HA, Jessurun ER, Linnenbank AC, Robles de Medina, Etienne O, Lesh MD, van Hemel NM. 1998. Body surface mapping during pacing at multiple sites in the human atrium: P-wave morphology of ectopic right atrial activation. Circulation 97(4):369-80.

Skasa M, Jüngling E, Picht E, Schöndube F, Lückhoff A. 2001. L-type calcium currents in atrial myocytes from patients with persistent and non-persistent atrial fibrillation. Basic Res Cardiol 96(2):151-9.

Swissa M, Qu Z, Ohara T, Lee MH, Lin SF, Garfinkel A, Karagueuzian HS, Weiss JN, Chen PS. 2002. Action potential duration restitution and ventricular fibrillation due to rapid focal excitation. Am J Physiol Heart Circ Physiol 282(5):H1915-23.

Taccardi B. 1963. Distribution of heart potentials on the thoracic surface of normal human subjects. Circ Res 12(4):341-52.

Taccardi B, Punske BB, Lux RL, MacLEOD RS, Ershler PR, Dustman TJ, Vyhmeister Y. 1998. Useful lessons from body surface mapping. J Cardiovasc Electrophysiol 9(7):773-86.

Ten Tusscher K, Noble D, Noble P, Panfilov AV. 2004. A model for human ventricular tissue. American Journal of Physiology-Heart and Circulatory Physiology 286(4):H1573-89.

Tikhonov Andrei Nikolaevich. 1963. On the solution of ill-posed problems and the method of regularization. Doklady akademii naukRussian Academy of Sciences. 501 p.

Tobón C, Ruiz-Villa CA, Heidenreich E, Romero L, Hornero F, Saiz J. 2013. A three-dimensional human atrial model with fiber orientation. electrograms and arrhythmic activation patterns relationship. PloS One 8(2):e50883.

Torres V, Tepper D, Flowers D, Wynn J, Lam S, Keefe D, Miura DS, Somberg JC. 1986. QT prolongation and the antiarrhythmic efficacy of amiodarone. J Am Coll Cardiol 7(1):142-7.

Trayanova N. 2006. Defibrillation of the heart: Insights into mechanisms from modelling studies. Exp Physiol 91(2):323-37.

Trujillo-Pino A, Krissian K, Alemán-Flores M, Santana-Cedrés D. 2013. Accurate subpixel edge location based on partial area effect. Image Vision Comput 31(1):72-90.

van Oosterom A and Oostendorp TF. 2004. ECGSIM: An interactive tool for studying the genesis of QRST waveforms. Heart 90(2):165-8.

Virag N, Jacquemet V, Henriquez C, Zozor S, Blanc O, Vesin J, Pruvot E, Kappenberger L. 2002. Study of atrial arrhythmias in a computer model based on magnetic resonance images of human atria. Chaos: An Interdisciplinary Journal of Nonlinear Science 12(3):754-63.

Visweswaran R, McINTYRE SD, Ramkrishnan K, Zhao X, Tolkacheva EG. 2013. Spatiotemporal evolution and prediction of [Ca2] i and APD alternans in isolated rabbit hearts. J Cardiovasc Electrophysiol 24(11):1287-95.

Wagner S, Maier LS, Bers DM. 2015. Role of sodium and calcium dysregulation in tachyarrhythmias in sudden cardiac death. Circ Res 116(12):1956-70.

Wang D, Kirby RM, MacLeod RS, Johnson CR. 2013. Inverse electrocardiographic source localization of ischemia: An optimization framework and finite element solution. Journal of Computational Physics 250:403-24.

Wang K, Lee P, Mirams GR, Sarathchandra P, Borg TK, Gavaghan DJ, Kohl P, Bollensdorff C. 2015. Cardiac tissue slices: Preparation, handling, and successful optical mapping. Am J Physiol Heart Circ Physiol 308(9):H1112-25.

Wang L, Myles RC, De Jesus NM, Ohlendorf AK, Bers DM, Ripplinger CM. 2014. Optical mapping of sarcoplasmic reticulum Ca2+ in the intact heart: Ryanodine receptor refractoriness during alternans and fibrillation. Circ Res 114(9):1410-21.

Wang Y, Cuculich PS, Zhang J, Desouza KA, Vijayakumar R, Chen J, Faddis MN, Lindsay BD, Smith TW, Rudy Y. 2011. Noninvasive electroanatomic mapping of human ventricular arrhythmias with electrocardiographic imaging. Sci Transl Med 3(98):98ra84.

Weiss JN, Qu Z, Chen P, Lin S, Karagueuzian HS, Hayashi H, Garfinkel A, Karma A. 2005. The dynamics of cardiac fibrillation. Circulation 112(8):1232-40.

Weiss JN, Qu Z, Shivkumar K. 2017. Electrophysiology of hypokalemia and hyperkalemia. Circ Arrhythm Electrophysiol 10(3):e004667.

Weiss JN, Garfinkel A, Karagueuzian HS, Qu Z, Chen PS. 1999. Chaos and the transition to ventricular fibrillation: A new approach to antiarrhythmic drug evaluation. Circulation 99(21):2819-26.

Wiegerinck RF, Verkerk AO, Belterman CN, van Veen TA, Baartscheer A, Opthof T, Wilders R, de Bakker JM, Coronel R. 2006. Larger cell size in rabbits with heart failure increases myocardial conduction velocity and QRS duration. Circulation 113(6):806-13.

Wilde AA, Postema PG, Di Diego JM, Viskin S, Morita H, Fish JM, Antzelevitch C. 2010. The pathophysiological mechanism underlying brugada syndrome: Depolarization versus repolarization. J Mol Cell Cardiol 49(4):543-53.

Williams EV. 1984. A classification of antiarrhythmic actions reassessed after a decade of new drugs. The Journal of Clinical Pharmacology 24(4):129-47.

Willoughby RA. 1979. Solutions of ill-posed problems (an tikhonov and vy arsenin). SIAM Rev 21(2):266.

Wilson FN, Macleod AG, Barker PS, Johnston FD. 1934. The determination and the significance of the areas of the ventricular deflections of the electrocardiogram. Am Heart J 10(1):46-61.

Workman AJ, Kane KA, Rankin AC. 2001. The contribution of ionic currents to changes in refractoriness of human atrial myocytes associated with chronic atrial fibrillation. Cardiovasc Res 52(2):226-35.

Zhang J, Sacher F, Hoffmayer K, O'Hara T, Strom M, Cuculich P, Silva J, Cooper D, Faddis M, Hocini M, et al. 2015. Cardiac electrophysiological substrate underlying the ECG phenotype and electrogram abnormalities in brugada syndrome patients. Circulation 131(22):1950-9.

Zhou X, Bueno-Orovio A, Orini M, Hanson B, Hayward M, Taggart P, Lambiase PD, Burrage K, Rodriguez B. 2016. In vivo and in silico investigation into mechanisms of frequency dependence of repolarization alternans in human ventricular cardiomyocytes. Circ Res 118(2):266-78.

Zlochiver S, Yamazaki M, Kalifa J, Berenfeld O. 2008. Rotor meandering contributes to irregularity in electrograms during atrial fibrillation. Heart Rhythm 5(6):846-54.